NANOMECHANICAL AND MICROWAVE RESONANCE SENSING FOR CHARACTERIZATION OF INDIVIDUAL VIRIONS AND NANOPARTICLES IN ATMOSPHERIC CONDITIONS

A DISSERTATION SUBMITTED TO

THE GRADUATE SCHOOL OF ENGINEERING AND SCIENCE

OF BILKENT UNIVERSITY

IN PARTIAL FULFILLMENT OF THE REQUIREMENTS FOR

THE DEGREE OF

DOCTOR OF PHILOSOPHY

IN

MECHANICAL ENGINEERING

By

Mohammed Alkhaled

September 2023

Nanomechanical and Microwave Resonance Sensing for Characterization of Individual Virions and Nanoparticles in Atmospheric Conditions

By Mohammed Alkhaled

September 2023

We certify that we have read this dissertation and that in our opinion it is fully adequate, in scope and in quality, as a dissertation for the degree of Doctor of Philosophy.

Mehmet Selim Hanay(Advisor)

Burhanettin Erdem Alaca

Emine Yegân Erdem

Alper Demir

Onur Özcan

Approved for the Graduate School of Engineering and Science:

Orhan Arıkan
Director of the Graduate School

ABSTRACT

NANOMECHANICAL AND MICROWAVE RESONANCE SENSING FOR CHARACTERIZATION OF INDIVIDUAL VIRIONS AND NANOPARTICLES IN ATMOSPHERIC CONDITIONS

Mohammed Alkhaled
Ph.D. in Mechanical Engineering
Advisor: Mehmet Selim Hanay
September 2023

This dissertation focuses on Nanoelectromechanical-based Mass Spectrometry (NEMS-MS), an innovative technique for characterizing nanoparticles and biomolecules weighing above the working limit of commercial mass spectrometry tools. It suggests performing NEMS-MS under atmospheric conditions and enhancing its capabilities with a built-in focusing lens. Amid the COVID-19 pandemic, the study addresses urgent virus detection needs, proposing a label-free method using NEMS-MS for individual virus detection and characterization. Notably, the study achieves mass spectrometry measurement of the SARS-CoV-2 virus using a NEMS-MS system operating entirely under atmospheric pressure. As the first to pioneer NEMS-MS in air, the study examines challenges tied to this, particularly how NEMS response in dissipative environments, known as Mode Shape Attenuation. Mathematical models and experiments dissect factors contributing to this attenuation, resulting in improved mass spectra and contributing toward the utilization of NEMS-MS for real-world application. Taking innovation a step further, the study introduces a microwave-based sensor for inferring electrical properties of nanoparticles. This sensor works in the electromagnetic domain, determining properties like dielectric constant and expanding the sensing possibilities. Overall, this dissertation propels NEMS-based sensing and characterization by combining mass spectrometry, microwave sensing, and atmospheric pressure operation. Addressing challenges and introducing innovative solutions, it advances NEMS-MS technology and offers a cost-effective tool for characterizing nanoparticles and biomolecules across various applications.

Keywords: Nanoelectromechanical systems, NEMS mass spectrometry, Atmospheric pressure mass spectrometry, label-free virus detection, SARS-CoV-2 mass measurement, Nanoparticle microwave sensing.

ÖZET

ATMOSFERİK KOŞULLARDA TEKLİ VİRÜSLERİN VE NANOPARÇACIKLARIN KARAKTERİZASYONU İÇİN NANOMEKANİK VE MİKRODALGA REZONANS ALGILAMA

Mohammed Alkhaled
Makine Mühendisliği, Doktora
Tez Danışmanı: Mehmet Selim Hanay
Eylul 2023

Bu doktora tezi, geleneksel kütle spektrometresi teknikleri için ağır olan nanoparçacıkları ve biyomolekülleri tartmak için devrim niteliğinde bir teknik olan Nanoelektromekanik tabanlı Kütle Spektrometresi (NEMS-MS) etrafında dönüyor. Çalışma, NEMS-MS'yi atmosferik koşullar altında yürütmeyi ve entegre bir odaklama merceği ile NEMS yongasının yeteneklerini geliştirmeyi önermektedir. COVID-19 salgını zemininde, tez, hızlı virüs tespiti için acil ihtiyacı ele almaktadır. NEMS-MS kullanarak tek tek virüsleri tespit etmek ve karakterize etmek için etiketsiz bir yaklaşım kullanılmıştır. Etkileyici bir şekilde, çalışma, tamamen atmosferik basınç altında çalışan ilk NEMS-MS sistemi tarafından elde edilen SARS-CoV-2 virüsünün kütle spektrometri ölçümünü sunmaktadır. Bu çalışma, atmosferik ortamlarda NEMS-MS'ye öncülük ettiğinden, tez, NEMS-MS'nin atmosferik koşullar altında çalıştırılmasındaki bazı zorlukları, özellikle de esas olarak havanın viskoz sönümünün neden olduğu enerji tüketen mod şekillerini araştırmaktadır. Mod Şekli Zayıflamasına yol açan faktörlerin karmaşık etkileşimi, matematiksel modeller ve deneyler kullanılarak incelenmiştir, gerçek dünyaya uygulamasına yönelik öncü bir sistematik çalışma ortaya konulmuştur. Bu analiz, yalnızca gelişmiş kütle spektrumlarına ortaya çıkarmakla kalmayıp, aynı zamanda teknolojiyi gerçek dünya senaryolarında daha uygulanabilir hale getirmeye yönelik önemli bir ilerleme ortaya koymaktadır. İnovasyonu bir adım öteye taşıyan çalışma, nanopartiküllerin elektriksel özelliklerini tanımlamak için tasarlanmış mikrodalga tabanlı bir sensörü de tanıtmaktadır. Atmosferik koşullar altında elektromanyetik alanda çalışan bu sensör, dielektrik sabit gibi özellikleri belirleyerek NEMS tabanlı algılama

araçlarının potansiyelini genişletmektedir. Genel olarak, bu tez, kütle spektrometresi, mikrodalga algılama ve atmosferde çalışma imkânını birleştirerek NEMS tabanlı algılama ve karakterizasyonu yeni zirvelere taşımıştır. Zorlukları doğrudan ele alan ve yaratıcı çözümler sunan bu çalışma, yalnızca NEMS teknolojisini ilerletmekle kalmamış, aynı zamanda çeşitli uygulamalarda nanoparçacıkları ve biyomolekülleri karakterize etmek için uygun maliyetli, çok yönlü bir araç sunmaktadır.

Anahtar sözcükler: Nanoelektromekanik sistemler, NEMS kutle spektrometrisi, Atmosferik basınç kkutle spektrometrisi, etiketsiz virkus tespiti, SARS-CoV-2 kkutle olçkumku, Nanoparçacık mikrodalga algılama.

Acknowledgement

I commence by expressing my profound gratitude to the Almighty Allah, the most Gracious and Merciful, for His blessings that have culminated in the successful completion of this dissertation. I wish to extend my acknowledgments to several individuals who have been instrumental in this journey.

I wish to convey my utmost appreciation to my esteemed Ph.D. advisor, Prof. Mehmet Selim Hanay, for his boundless support throughout my journey of Ph.D. study and research. His patience, motivation, enthusiasm, and vast knowledge have been instrumental in shaping my academic growth. His guidance has been an unwavering light, guiding me through the intricacies of research and the meticulous process of writing this dissertation. I am immensely grateful for the privilege of having such an exceptional advisor and mentor for my Ph.D. journey. On a personal note, I also extend my gratitude for his understanding and support during the challenging moments that marked my Ph.D. pursuit.

I am equally indebted to my thesis monitoring committee members: Prof. Burhanettin Erdem Alaca and Prof. Emine Yegân Erdem, as well as the members of my dissertation defense jury: Prof. Alper Demir and Prof. Onur Özcan. Your gracious acceptance of being a part of my dissertation defense jury and your insightful feedback after reading my dissertation have been invaluable.

My deepest gratitude is reserved for my father, Abdulrahman, and my mother, Somayah. Your prayers and support have enhanced every facet of my Ph.D. journey and I am thankful for your encouragement in pursuing my Ph.D. studies. I aspire to make you proud, Dad. May Allah forgive you and elevate your standing among those who tread the righteous path. To my beloved mother, may Allah bless you with enduring health and a life filled with goodness.

In this space, I also wish to acknowledge and express my heartfelt thanks to my beloved wife and my partner in all aspects of life, Fatima. Your enduring love and steadfast support have been a constant source of strength, especially during the demanding years of my Ph.D. journey. I am profoundly grateful for your presence by my side, and I eagerly anticipate the opportunity to reciprocate your sacrifices. Your care and nurturing of me and our little ones have been a beacon of comfort. My heart overflows with gratitude for my young children, Yusuf and

Abdulrahman, who have infused my recent years with unbridled joy. I beseech Allah to illuminate your paths with guidance and to grant you with a heart that loves to obey Him. May Allah lead you to the highest echelons of achievement in both this world and the hereafter.

My acknowledgments extend to my esteemed colleagues and research group members: Dr. Hashim Alhmoud, Sayedus Salehin, Enise Kartal, Uzay Tefek, and Ceren Alataş. I am equally grateful to former group members, Tufan Ramazan Erdogan and Batuhan Emre Kaynak. The collaborative journey with each of you has been enriching, and I extend my best wishes for your future endeavors.

I extend my thanks to Ms. Elâ Baycan, Ms. Guliz Erdal, and Mr. Şakir Duman. Special mentions go to Dr. Cenk Yanık from Sabancı University for EBL fabrication of NEMS devices, and to Dr. Ahmet Murat Yağcı from METU MEMS for his assistance in wirebonding NEMS devices. My gratitude is extended to Abdullah Kafadenk for his guidance and assistance in the cleanroom. I extend my appreciation to Prof. Aykut Özkul of Ankara University for generously providing the virus sample crucial to the measurements and findings reported in this dissertation.

This work stands as a testament to the generous support provided by the European Research Council (ERC), under grant no. 758769, Additionally, I am deeply indebted to the Scientific and Technological Research Council of Turkey (TÜBİTAK) for their funding under agreement no. EEEAG-119E503 which has made this work possible.

Finally, I extend a heartfelt thank you to all my family and friends who have contributed to making my Ph.D. journey a joyful one.

Contents

1 Introduction & Background **1**

1.1 Mass Spectrometry 2

1.2 Nanoelectromechanical Systems-based Mass Spectrometry (NEMS-MS) 5

1.3 Soft Ionization Techniques 8

1.3.1 Matrix-Assisted Laser Desorption/Ionization 8

1.3.2 Electrospray Ionization 9

1.4 Alternative Mass Sensing Approaches 11

1.4.1 Gas-Phase Electrophoretic Molecular Mobility Analyzers (GEMMA) 11

1.4.2 Mass Photometry 12

1.4.3 Charge Detection Mass Spectrometry 12

1.5 Motivation 14

1.6 Dissertation Structure 16

2 Atmospheric NEMS-MS for Virus Detection and Mass Measurement **18**

2.1 NEMS as Virus Mass Sensors 20

2.1.1 Working Principle 20

2.1.2 Estimation of Mass and Landing Position 22

2.1.3 Device Fabrication 25

2.2 Electrospray Ionization 31

2.2.1 Electrospray Ionization Working Principle 31

2.2.2 Electrostatic Focusing 33

2.2.3 ESI Setup and Parameters 36

2.3 Virus Isolation and Sample Preparation 38
2.3.1 Isolating SARS-CoV-2 from Cell Culture 38
2.3.2 Isolating BoHV-1 from Cell Culture 38
2.3.3 Virus Precipitation & Purification 39
2.4 Experimentation 41
2.4.1 Actuation and Read-out Scheme 41
2.4.2 Optimization of ESI System and Electrostatic Focusing . . 42
2.5 Two Modes Measurements & Data Analysis 44
2.5.1 Event Finding Algorithm 45
2.5.2 NEMS-MS Resolution 48
2.5.3 Mass Calculation 49
2.6 Results 51
2.6.1 Purified SARS-CoV-2 Mass Measurements 51
2.6.2 SARS-CoV-2 Mass Measurements (Purified *vs.* Lysate) . . 54
2.6.3 SARS-CoV-2 *vs.* BoHV-1 Mass Spectrum 57

3 Dissipative Mode Shapes in Atmospheric NEMS-MS 59
3.1 Introduction 60
3.2 Mode Shape Attenuation and Atmospheric NEMS-MS 63
3.3 Mathematical Modelling Based on Wave Propagation 65
3.4 Experimental Results *vs.* Proposed Model 69
3.5 Dissipation and Mass Uncertainty 73
3.6 Mode Shape Attenuation Effect: Experimental Results 79
3.7 Potential Strategies to Address Mode Shape Attenuation 82
3.7.1 Three Mode Experiments 82
3.7.2 Statistical Approach 87

4 Microwave-Based Characterization of Nanoparticle Electric Properties 89
4.1 Microwave sensor working principle 90
4.2 Microwave Sensor Design 93
4.3 Proof of Concept Demonstration 95
4.4 Nanoscale Sensing Region Fabrication 97
4.5 Proof of Concept Experiment 99

4.6 Results 101
4.7 Discussion and Future Work 105

5 Conclusion **107**
5.1 Summary 107
5.2 Outlook and Future Work 108

A Fabrication Recipes and Masks **121**

List of Figures

1.1 Main components of Mass Spectrometry setup. 2
1.2 Working principle of Matrix-assisted laser desorption/ionization (MALDI). 8
1.3 Working principle of Electrospray Ionization (ESI), adapted from [1]. 10
1.4 Technological gap filled by NEMS-MS. 14

2.1 Mass-spring-damper system. 21
2.2 First and second fundamental out-of-plane mode shapes of doubly-clamped beams. 23
2.3 Mode shapes and resulting frequency shifts in the first and second modes. Different mass values are presented by different crescent-like contours and different landing positions are presented as lines with different slopes. 25
2.4 Fabrication steps for self-focusing NEMS device. 28
2.5 Colorized SEM image of the fabricated self-focusing NEMS device. 29
2.6 Electrospray Ionization and electrostatic focusing of nanoparticles. 32
2.7 Architecture of the particles and molecules transmission system in the previous state-of-the-art. Adapted from [2, Sergio Dominguez-Medina et al., Neutral mass spectrometry of virus capsids above 100 megadaltons with nanomechanical resonators. Science 362, 918-922(2018). DOI:10.1126/science.aat6457]. Reprinted with permission from AAAS. 34
2.8 Illustration of ESI system with the dimensions and process parameters. 37

2.9 Virus sample PEG precipitation and purification. 40
2.10 NEMS drive and read circuitry using Lock-in amplifier. 42
2.11 Demonstration of electrostatic focusing of 200 nm fluorescent PS nanoparticles. 43
2.12 Frequency shifts on fundamental modes of NEMS caused by a particle landing event. 45
2.13 3D plot of sweeping the minimum prominence and minimum slope threshold. 46
2.14 Frequency PLL data of the first and second modes along with its calculated slope. 47
2.15 Zoom-in to frequency PLL data of the first and second modes. Zoom-in illustrates an instance of local minima within the noise and a detection of an event in a single mode. 47
2.16 Allan deviation calculation for NEMS device calculated when shutter was closed. PLL time constant = 140 ms. 49
2.17 Mass and inferred diameter histograms of SARS-CoV-2 virus. . . 52
2.18 Mass spectrum of SARS-CoV-2 virus obtained from both PEG-precipitated and lysate samples. 55
2.19 Inferred diameter histograms of SARS-CoV-2 and BoHV-1 viruses. 58

3.1 NEMS displacement measurements in air and vacuum. For NEMS operating in air, the quality factors for the first, second, and third mode shapes are 32, 54, and 73, respectively. Conversely, in a vacuum, the quality factors shift to 23600, 22800, and 20300 for the first, second, and third mode shapes, respectively. Figures adapted from [3, C. Ti et al.; Dynamics of NEMS resonators across dissipation limits. Appl. Phys. Lett. 11 July 2022; 121 (2): 023506. https://doi.org/10.1063/5.0100318] with permission from AIP Publishing, License Number: 5610710652347. 62
3.2 The effect of the mode shape attenuation on Two-mode theory. . 63
3.3 Mathematical model of mode shape attenuation based on wave propagation. 67

3.4 COMSOL simulated mode shapes of the device utilized in (Ti et al., 2022). Panels (a-c) display the first three mode shapes in isometric view and panels (d-f) depict the out-of-plane view of the corresponding modes. 69
3.5 Comparison between the mathematical model and experimental results adapted from [3] concerning vacuum condition in the first three modes. 70
3.6 Comparison between the mathematical model and experimental results adapted from [3] concerning air condition in the first three modes. 70
3.7 Comparison between the mathematical model and experimental results adapted from [3] concerning air condition in the first three modes with boundary condition modified. 71
3.8 Function $g(x)$ for a NEMS operating at vacuum condition ($Q_1 = 23600$ and $Q_2 = 22800$). 75
3.9 Function $g(x)$ for a NEMS operating at atmospheric condition ($Q_1 = 32$ and $Q_2 = 54$). 75
3.10 The emergence of two distinct solutions for the landing position due to dissipation. The two curves would overlap if there were no dissipation. 76
3.11 The uncertainty in mass measurement arising from the ambiguity in the landing side. In vacuum conditions, the quality factors were $Q_1 = 23600$ and $Q_2 = 22800$ for the first and second modes, respectively, while in an air environment, they were $Q_1 = 32$ and $Q_2 = 54$. 77
3.12 Experimental demonstration of mode shape attenuation effect. Workflow is depicted in panel (a). Panels (b) and (c) display bright field and fluorescent microscope images, respectively, captured after a single landing event. Scale bar: 5 µm. 79
3.13 Illustration of experimental findings demonstrating the occurrence of mode shape attenuation. 80

3.14 Relationship between the change in the third mode frequency (δf_3) and the ratio of changes in the first and second modes ($\delta f_1/\delta f_2$), which correspond to the landing position. Error bars in the plot represent the range of δf_3 values derived from the inherent size distribution of the 200 nm PSNP used in this analysis. Quality factors of NEMS operated in air were employed, specifically $Q_1 = 32$, $Q_2 = 54$, and $Q_3 = 73$. 83
3.15 Monte Carlo simulation for 200 nm PSNP. Quality factors of NEMS operated in air were employed, specifically $Q_1 = 32$, $Q_2 = 54$, and $Q_3 = 73$. 85
3.16 Monte Carlo simulation for 50 nm GNP. Quality factors of NEMS operated in air were employed, specifically $Q_1 = 32$, $Q_2 = 54$, and $Q_3 = 73$. 86
3.17 Histograms depicting mass measurements of 40 nm GNP particles, as reported by [4], and after applying the statistical approach outlined along with respective non-parametric probability density functions (PDF). The vertical line represents the nominal mass value for a 40 nm GNP particle. 88

4.1 Microwave Sensor at the Nano Scale for Nanoparticle Electrical Characterization. 91
4.2 Microwave resonator proposed. (a) Split-ring resonator (SRR) with a nano-scale sensing region in the inner ring or (b) Coplanar waveguide (CPW) fabricated off the chip containing the sensing gap and interconnected by wirebonds. Panel (c) illustrates the nano-scale sensing gap that is situated between two electrodes (signal and ground). 93
4.3 Nano-scale sensing region with self-focusing ion lens. 96
4.4 Microwave nano-scale sensing region fabrication. 98
4.5 Microwave sensing experiment with 100nm fluorescent polystyrene nanoparticles. 100
4.6 PLL Data and results from the 100 nm polystyrene nanoparticles spray and control solution spray. 102

4.7 ΔY histogram for control and 100 nm PSNP experiments with intrinsic phase of 1.07π and 1.4π, respectively. 103

A.1 1^{st} EBL mask used for patterning the electrodes (Full size). Distance between each two subsequent dots is 1 μm 122
A.2 Close-up view to the 1^{st} EBL mask used for patterning the electrodes. Distance between each two subsequent dots is 200 nm . . 123
A.3 Zoom-in to a single electrode in the 1^{st} EBL mask. Distance between each two subsequent dots is 20 nm 123
A.4 2^{nd} EBL mask used for patterning the beam and clamping region (Full size). Distance between each two subsequent dots is 2 μm . 124
A.5 Close-up view to the 2^{nd} EBL mask used for patterning the beam and clamping region. Distance between each two subsequent dots is 200 nm 125
A.6 Layout of the 3 leg CPW resonator. Distance between each two subsequent dots is 500 nm 126
A.7 Layout of the PCB utilized in the proof-of-concept microwave experiment illustrating the microwave CPW resonator, the fused silica chip with the nanoscale sensing region along with the SMA connectors and wirebonds. Distance between each two subsequent dots is 1 µm 127

List of Tables

1.1 Major experiments and milestones in the NEMS-MS field. 6

2.1 Inductively Coupled Plasma (ICP) etching recipe and parameters for Silicon and Silicon Nitride layers. 30
2.2 Electrospray Ionization system parameters. 43
2.3 Measured SARS-CoV-2 diameters obtained through various techniques as reported in the literature. 53
2.4 Statistical measures of SARS-CoV-2 Experiments (PEG-precipitated *vs.* Lysate). 56

3.1 Air and vacuum fitting parameters for the first 3 out-of-plane modes. 72

Chapter 1

Introduction & Background

Nanoelectromechanical Systems (NEMS) are intricate devices that integrate mechanical structures and electronic components with features at the submicron scale. NEMS have a wide range of applications, including sensors, actuators, and computing. The focus of this dissertation is on utilizing NEMS as mass sensors for nanoparticles, viruses and other biomolecules. This technique, known as Nanoelectromechanical-based Mass Spectrometry (NEMS-MS), offers a promising approach for weighing particles that are too large to be measured using conventional Mass Spectrometry (MS) techniques. Additionally, this dissertation proposes an advanced approach that enables the sensing process to be carried out entirely under atmospheric conditions. This means conducting experiments at atmospheric pressure and room temperature, which has not been previously explored in the context of NEMS-MS. The dissertation addresses the challenges associated with performing experiments in an atmospheric environment, such as dissipation due to viscous damping. Moreover, this dissertation introduces a novel microwave sensor designed to extract further insights into the nanoparticles' characteristics. The sensor operating within the electromagnetic domain is seamlessly integrated with the Electrospray Ionization (ESI) system for nanoparticle transportation. Operating effectively within atmospheric conditions, this sensor is poised to deliver vital nanoparticle traits such dielectric constant.

1.1 Mass Spectrometry

Mass Spectrometry (MS) is an analytical technique that allows researchers to determine the molecular structure of a substance by measuring the mass-to-charge ratio (m/z) of its ions. The basic principle of mass spectrometry is shown below in Figure 1.1 and it starts with ionizing the sample and then separating and sorting the resulting ions based on their mass-to-charge ratio at the mass analyzer. The intensity is then determined by measuring the abundance of each ion by a detector.

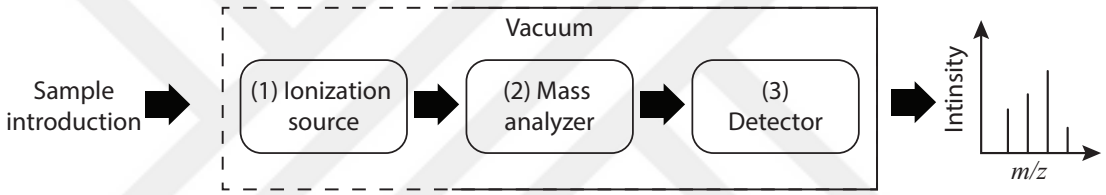

Figure 1.1: Main components of Mass Spectrometry setup.

There are several methods of generating the ions (*i.e.*, ionization), including electron impact ionization, electrospray ionization (ESI), and matrix-assisted laser desorption/ionization (MALDI). A review of ionization techniques will be discussed thoroughly in a separate section due to its relevance to this dissertation (section 1.3). Ion sorting occurs in the mass analyzer where they get accelerated and then separated according to their m/z. The most common type of mass analyzers include quadrupole mass analyzer, which uses a set of four electrically charged rods to filter ions based on their m/z. Other types of mass analyzers include time-of-flight (TOF) mass spectrometry, ion trap mass spectrometry, and Fourier transform ion cyclotron resonance (FTICR) mass spectrometry. After the ions are separated, the detector converts the ion signal into an electrical signal. The resulting mass spectrum shows the intensity of each ion as a function of its mass-to-charge ratio. From this information, researchers can determine the molecular weight and chemical composition of the sample. The reader is referred to the following book [5] for a comprehensive review of different mass spectrometry techniques (including a detailed review of ionization techniques, mass analyzers and detectors) currently available as well as a detailed discussion of mass spectrometry workflow from sample preparation to data analysis.

The origins of mass spectrometry can be traced back to the work of J.J. Thomson in the late 19th century, who discovered the electron and developed the first mass spectrometer [6]. In this experiment, Thomson's work paved the way for the development of modern mass spectrometry, which began in the 1920s with the work of Arthur Dempster and Francis Aston. Dempster invented the first electron impact source whereas Aston, on the other hand, developed the mass spectrograph, which could separate ions based on their mass-to-charge ratio and measure their abundance [7]. The field had developed further with the development of Time-of-flight (TOF) mass spectrometry by Stephens in 1964 [8]. Later, new ionization techniques were developed such as Chemical Ionization by Frank Field in 1966 and field desorption ionization by Beckey three years later. During these years, the technique was primarily used for the analysis of small organic molecules. The field of mass spectrometry expanded further in the 1970s and 1980s to include the analysis of larger biological molecules, such as proteins and nucleic acids. This was made possible with the development of soft ionization techniques, such as electrospray ionization [9] and matrix-assisted laser desorption/ionization [10], which allowed for the ionization of large molecules to gaseous phase without fragmenting them. A comprehensive overview of the historical development of the field of mass spectrometry can be found in [7] and [11].

Today, mass spectrometry is used in a wide range of fields, including chemistry, biology, medicine, and environmental science. Its applications continue to expand as new technologies and methods are developed, making it an essential tool for scientific research and discovery. One of the most important applications of mass spectrometry is in proteomics (*i.e.*, the study of proteins). Proteins are complex biomolecules that play a crucial role in many biological processes, including metabolism, signaling, and gene expression. Mass spectrometry allows researchers to identify and quantify proteins in a sample and study their interactions with other molecules. This information can help researchers understand the function of proteins in cells and tissues, and develop new drugs to treat diseases.

However, most of the mass spectrometry techniques that are commercially available cannot measure larger biomolecules such as supramolecular assemblies,

exosomes, viruses and lipid vesicles which have masses exceeding 10 MDa [4]. This mass range also include synthetic metallic, ceramic and polymeric nanoparticles as well as quantum dots (QDs). This is mainly due to the fact that when large ions or particles are ionized, they become multiply-charged leading to difficulty in relating the resulting m/z spectra to mass [12]. When the ionized particles are multiply charged, it becomes crucial to identify their charge from the m/z spectrum [13], as this information is required to calculate their mass accurately.

Aside from its significant limitation in measuring large particles, mass spectrometry (MS) is an expensive and intricate analytical technique that demands trained technicians for its operation. The ultra high vacuum (UHV) subsystem, which is essential for ionization and separation of charged particles, is among the components that increase the cost of the system. Consequently, there is a present demand for a cost-effective technique that can measure the mass of intact particles at mass range $>$ 10 MDa.

1.2 Nanoelectromechanical Systems-based Mass Spectrometry (NEMS-MS)

Nanoelectromechanical Systems (NEMS) have emerged as a promising technique for mass spectrometry, utilizing NEMS structures as mass sensors. These structures are miniaturized devices with at least one dimension in the submicron range (*i.e.*, $< 1 \times 10^{-6}$ m), several times smaller than the diameter of a human hair.

In NEMS-based mass spectrometry, the sample is ionized, and the molecules or particles are deposited onto a NEMS resonator. The resonator vibrates at specific frequency(ies), and the device response is electronically sensed by nano-sized electrodes. The adsorption of particles on the sensor alters the resonance frequency, primarily decreasing it, due to the increased mass. By analyzing the changes in the resonator frequency, the mass of the deposited ions can be accurately determined.

Various mechanical structures, including cantilevers [14, 15], membranes [16], and doubly-clamped beams [2, 4] are employed for mass sensing . One notable application of NEMS-MS lies in the realm of proteomics, which involves the study of proteins. Proteomic analysis heavily relies on mass spectrometry to characterize proteins within cells. However, the complex and dynamic nature of biomarkers poses a significant challenge in proteomics, necessitating the development of improved characterization tools. NEMS devices are inherently suitable for mass spectrometry due to their tiny masses, enabling high-resolution measurements of added mass. Moreover, NEMS-MS can cover mass ranges typically unattainable by conventional Mass Spectrometry. This extended mass range includes synthetic nanoparticles, protein aggregates, intact viruses, and other biomolecules with weights ranging from MDa to GDa, which surpass the capabilities of conventional MS.

Recent advances in NEMS-MS which will be presented in this dissertation offers a cost-effective alternative to bulky and expensive systems like mass analyzers and detectors. Additionally, it is worth noting that NEMS-MS can determine

Table 1.1: Major experiments and milestones in the NEMS-MS field.

Year	Reference	Main advancement / Experiment
2002	Roukes et al. [19]	Invention of the NEMS-based Mass Spectrometry method
2004	Ekinci et al. [20]	NEMS-MS of Au molecules with attogram (10^{-18}g) sensitivity
2006	Yang et al. [21]	NEMS-MS of N_2 gas molecules with zeptogram (10^{-21}g) sensitivity
2009	Naik et al. [22]	Mass probability analysis of the BSA protein using single-mode NEMS-MS
2012	Hanay et al. [23]	Mass measurement of intact biomolecule (IgM antibody) using dual-mode NEMS-MS
2012	Chaste et al. [24]	First 1D (CNT) NEMS-MS experiment
2014	Chan et al. [25]	Weighing ultra large biomolecular complexes ($10^{-11} - 10^{-6}$g)
2015	Sage et al. [26]	First hybrid MS device comprising TOF and NEMS MS showing that the later is charge-state independent
2016	Malvar et al. [27]	NEMS MS for whole bacteria (10^{-13}g)
2018	Dominguez-Medina et al. [2]	NEMS MS for intact virus capsids (10^{-16}g)
2021	Hanay et al. [28]	Invention of self-focusing NEMS-MS for high throughput measurements
2022	Hanay et al. [4]	NEMS-MS experiment to measure SARS-CoV-2 virus conducted for the first time in atmospheric conditions

the mass of particles regardless of their charge state, eliminating the reliance on charge-state of the particle or molecule [17].

The earliest form of a NEMS device can be traced back to 1960 when a metal-oxide-semiconductor field-effect transistor (MOSFET) was developed, utilizing a 100 nm thick oxide layer [18]. The field of NEMS-MS, however, is more recent and has progressed significantly with the advent of nanofabrication techniques, such as e-beam lithography, capable of patterning at submicron scales.

The concept of NEMS-MS was first invented by Prof. Michael Roukes and Dr. Kamil Ekinci in the early 2000s [19]. The Caltech team conducted pioneering experiments in which they measured gold atoms aggregates with attogram

resolution (*i.e.*, 1×10^{-18}g) in 2004 [20], and later nitrogen gas molecules with zeptogram resolution (*i.e.*, 1×10^{-21}g) in 2006. The first-ever NEMS-MS experiment on a single biomolecule level was conducted in 2009 by Naik et al. [22]. In these trials, the NEMS device resonated in a single mode, facilitating analysis of mass probabilities of BSA protein rather than direct mass measurement, as the frequency shifts were influenced by the molecule's landing position of the NEMS device. Three years later, Hanay et al. introduced a dual-mode NEMS-MS system with the ability to disentangle the relationship between the molecule's landing position and its mass, thereby successfully measuring the mass of human IgM antibodies [23]. This achievement marked the first instance of measuring the mass of large intact biomolecules using NEMS-MS. Over the past decade, NEMS-MS has further developed, with researchers devising methods to ionize, deposit, and measure intact bacteria and viruses. Table 1.1 provides a chronological overview of the historical progression and breakthroughs in NEMS-MS, with a specific emphasis on experiments related to bio-sensing through "all-electronic" NEMS-based mass spectrometry.

1.3 Soft Ionization Techniques

Ionization techniques are pivotal in mass spectrometry as they facilitate the transformation of analyte molecules into mobile ions for subsequent analysis and measurement. These techniques can be broadly categorized into two main groups: hard ionization and soft ionization. Hard ionization techniques, such as electron ionization (EI), lead to extensive fragmentation and yield highly energetic ions. In contrast, soft ionization techniques generate intact molecular ions with minimal fragmentation, making them well-suited for analyzing larger molecules, such as protein aggregates, viruses and other complex biomolecules, which are the focus of this dissertation.

1.3.1 Matrix-Assisted Laser Desorption/Ionization

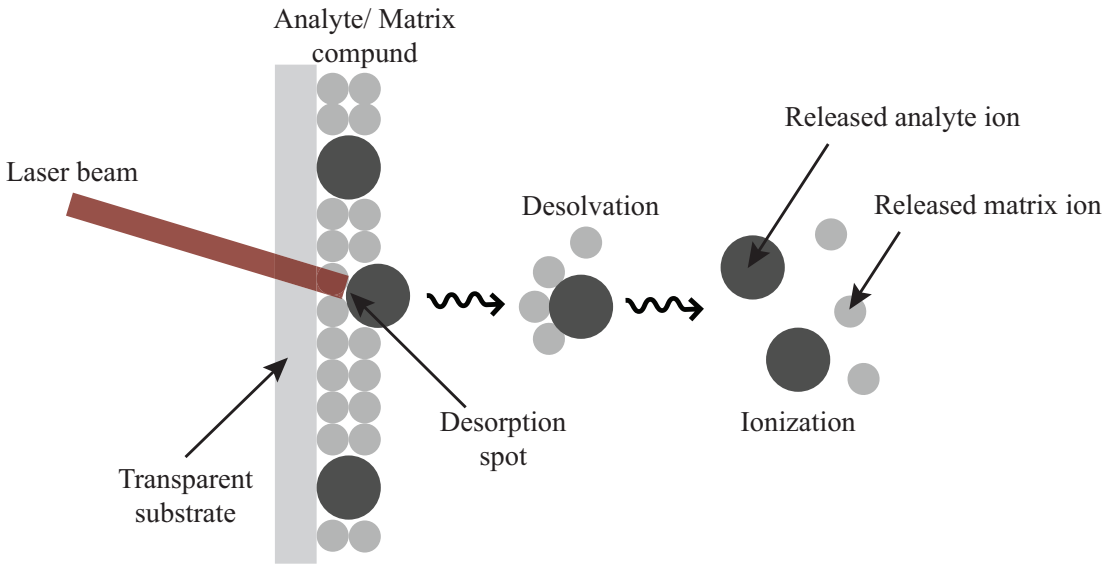

Figure 1.2: Working principle of Matrix-assisted laser desorption/ionization (MALDI).

Matrix-Assisted Laser Desorption/Ionization (MALDI) is a powerful analytical technique that leverages laser radiation to facilitate the desorption of analytes from a sample consisting of both analyte molecules and a matrix compound. As depicted in Figure 1.2, when the sample is exposed to laser irradiation, the matrix

compound absorbs the energy from the laser, which in turn aids in the desorption of analyte molecules. This process leads to the ionization of the analytes and the formation of intact molecular ions, enabling their analysis in their native state with minimal fragmentation. The advantages of MALDI are particularly valuable in the field of nanoelectromechanical systems mass spectrometry (NEMS-MS) applications, where it has found wide application for the ionization of nanoparticles. One notable example is the ionization and detection of gold nanoparticles (GNP) using non-linear nanoelectromechanical systems (NEMS) mass sensors [29]. By employing MALDI in this context, researchers have been able to effectively ionize and detect 20 nm GNP, enabling the construction of mass spectra from over 500 individual landing events with high sensitivity.

Despite its numerous advantages, Matrix-Assisted Laser Desorption/Ionization (MALDI) also has a few inherent disadvantages. Firstly, it exhibits a limited mass range, making it less suitable for the analysis of smaller molecules or compounds with high volatility. Additionally, the presence of the matrix compound in MALDI can cause interference, generating background signals or overlapping peaks that hinder the accurate identification of analyte ions. Furthermore, the high laser energy used in MALDI can lead to sample degradation or fragmentation, affecting the analysis of delicate and sensitive analytes. Finally, the complexity and cost of MALDI instrumentation, including lasers and high-vacuum systems, may limit its accessibility to certain researchers or laboratories.

1.3.2 Electrospray Ionization

Electrospray Ionization (ESI) is a soft ionization technique widely employed for ionizing nanoparticles and biomolecules directly from their native solutions with minimal fragmentation. In ESI, the sample is pumped through a nozzle or tip that is maintained at a high voltage, typically in the kilovolt (kV) range. As illustrated in Figure 1.3 (adapted from [1]), this process initiates the formation of a liquid meniscus, also known as the Taylor cone. The Taylor cone emits charged microdroplets containing the particles or molecules of interest.

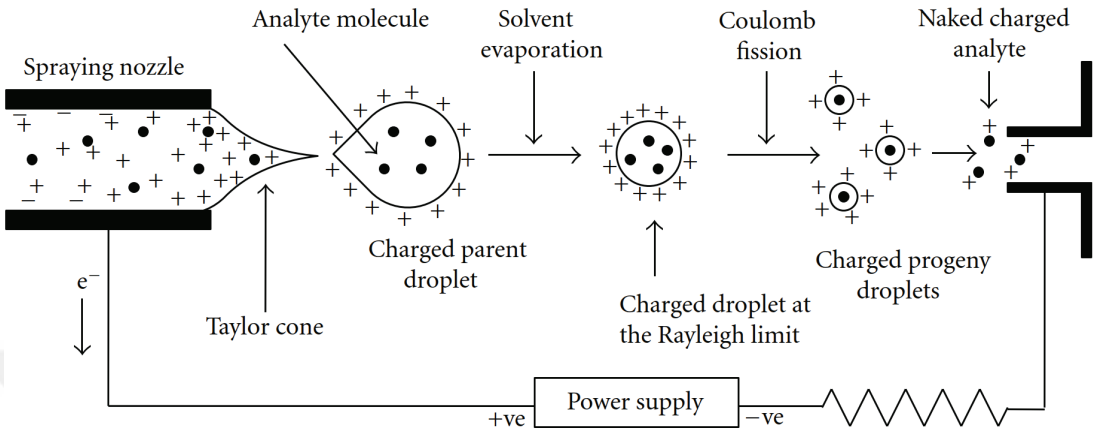

Figure 1.3: Working principle of Electrospray Ionization (ESI), adapted from [1].

As these droplets move away from the tip, they undergo evaporation, resulting in a reduction in size while retaining their initial charge. Upon reaching a critical point called the Rayleigh limit, the droplets can no longer sustain the preserved charge, leading to Coulomb fission. This phenomenon causes the droplets to explode, generating smaller droplets. The charge is distributed among these newly formed droplets, and the process continues at smaller scales until single nanoparticles, viruses, or biomolecules become ionized.

Electrospray Ionization offers a significant benefit over MALDI by directly ionizing molecules and analytes from the native solution. As a result, there is no requirement for intermediate procedures like depositing onto a substrate before ionization. Additionally, this technique operates seamlessly under atmospheric conditions, providing a straightforward and convenient setup.

1.4 Alternative Mass Sensing Approaches

In an effort to overcome the limited mass range of conventional Mass Spectrometry (MS) techniques, various alternative approaches are currently being developed. In addition to Nanoelectromechanical Systems Mass Spectrometry (NEMS-MS), several other research avenues have emerged. This section aims to provide an overview of these research lines that enable the analysis of analytes exceeding the size range accommodated by conventional MS techniques. The review encompasses Gas-Phase Electrophoretic Molecular Mobility Analyzers (GEMMA), Mass Photometry (MP) and Charge Detection Mass Spectrometry (CDMS).These innovative methods offer alternative solutions for measuring large analytes that fall outside the range of traditional MS techniques.

1.4.1 Gas-Phase Electrophoretic Molecular Mobility Analyzers (GEMMA)

The combination of Gas-phase electrophoretic molecular mobility analyzers (GEMMA) with Electrospray Ionization (ESI) has proven to be highly effective in the detection of biological species within the mass range of single viruses [30]. GEMMA operates by separating charged particles in the gas-phase based on their electrophoretic mobility diameter (EMD). Through the assumption of a spherical geometry and the use of an internal standard, the molecular weight (Mw) of the analyte species can be accurately determined. Notably, GEMMA offers the advantage of ambient pressure separation and exhibits less dependence on sample purity and homogeneity compared to similar techniques such as native electrospray ionization time-of-flight mass spectrometry (native ESI ToF MS).

However, GEMMA and NEMS-MS differ fundamentally in their approach to mass measurements. GEMMA relies on electrophoretic principles and requires the charge state of the analyte for determining its molecular weight (Mw). In contrast, NEMS-MS directly measures the mass of analytes through the mass change of a resonant structure upon adsorption. Additionally, the EMD of species

depends on its morphology. Morphological variations, such as the shrinkage of empty capsids, can lead to discrepancies in the measured Mw for species with different electrophoretic mobility diameters (EMD) as demonstrated in [31].

1.4.2 Mass Photometry

Mass Photometry (MP) is another emerging technique for determining the molecular mass of proteins, nanodiscs, and other nanoscale objects [32]. It operates based on interferometric scattering microscopy, in which the optical scattering signal of an analyte molecule is enhanced near an interface. The interface enhances the measurement because of it allows the the optical scattering signal from the analyte to interfere with the optical reflection signal from the same interface. The collected optical signal from the is correlated with the molecular mass, offering a valuable means of probing molecular mass with high time-resolution while the molecules are suspended in their native liquid solution. Nevertheless, MP technique has been used for species with a mass below 10 MDa [33]

1.4.3 Charge Detection Mass Spectrometry

A more relevant technique, Charge Detection Mass Spectrometry (CDMS), represents an innovative approach to mass analysis, focusing on directly detecting the charges carried by ions instead of relying solely on measuring their mass-to-charge ratio m/z as in traditional mass spectrometry. The technique can utilize different charge detection methods such as single-pass, linear array, or ion trap, which enable the resolution of the charge state of ions in combination with the m/z measurement from traditional detectors. By incorporating this information, CDMS allows for the determination of the mass of individual ions with multiple charges.

Among the various charge detection techniques, Ion traps have demonstrated superior accuracy in charge measurement compared to Single-pass and Linear

array methods [34]. In Ion trap CDMS, the analyte ions are trapped and confined within a high-vacuum environment using specialized devices such as ion traps. Within the trap, the ions undergo oscillatory or rotational motion induced by an electric field. As the ions interact with an electrode or a charged surface acting as a detector, the resulting changes in the electrical potential of the detector are directly proportional to the charges carried by the ions.

As demonstrated in various studies [35, 36, 37, 38], this approach enables the detection and measurement of biomolecules weighing up to several hundred MDa. Unlike CDMS and other mass spectrometry techniques that rely on m/z detectors, NEMS technology offers the unique ability to directly measure mass without dependence on the charge state of ions. This characteristic makes NEMS-MS immune to discrepancies in the spectrum arising from identical species with different charge states. Additionally, this mass range ($>$ 10 MDa) has been identified as optimal for Nanoelectromechanical systems by the practitioners in the field of mass spectrometry [17].

1.5 Motivation

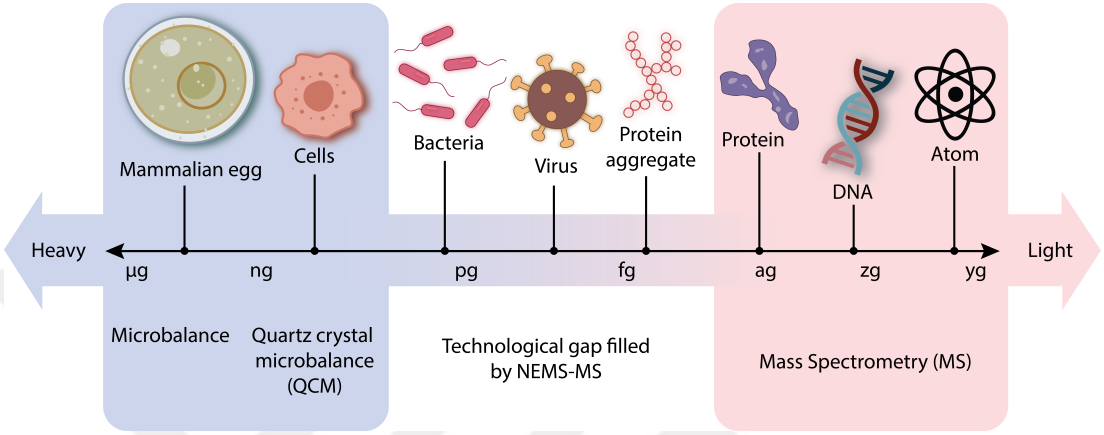

Figure 1.4: Technological gap filled by NEMS-MS.

The development of nanoelectromechanical systems (NEMS) based mass spectrometry (MS) is motivated by the desire to overcome the limitations of conventional mass spectrometry techniques. This innovative approach aims to provide a fast and precise method for characterizing the mass of nanoparticles and biomolecules. NEMS-MS offers distinct advantages and capabilities that make it appealing in various research fields.

One crucial advantage of NEMS-MS is its ability to measure a broad range of masses, extending into the MDa and GDa range, which is typically inaccessible to conventional mass spectrometry techniques. Unlike most other mass spectrometry methods, NEMS-MS can directly measure the mass of individual analyte molecules or particles without relying on their charge states or mass-to-charge ratios (m/z).

NEMS-MS also excels in sensitivity and resolution for mass analysis. The nanoscale resonant structures used in NEMS devices possess exceptional mechanical properties, enabling precise measurements of mass changes induced by the adsorption of analyte molecules.

Furthermore, NEMS-MS holds promise for miniaturization and integration with other analytical systems. The small size and scalability of NEMS devices

make them compatible with microfluidic systems, lab-on-a-chip platforms, and other miniaturized analytical tools. This integration facilitates efficient sample handling, improved sensitivity, and multiplexed analysis, opening up possibilities for high-throughput and point-of-care applications.

Another advantage of NEMS-MS is its capability to analyze a wide range of analytes, including nanoparticles, biomolecules, polymers, and complex mixtures. This versatility makes it applicable in various fields such as proteomics, pharmaceuticals, materials science, and environmental monitoring. By providing accurate and detailed information about analytes' mass and properties, NEMS-MS contributes to a better understanding of their behavior, interactions, and functions.

Overall, the motivation behind NEMS-MS is driven by the need for improved analytical techniques capable of analyzing nanoscale objects with high sensitivity, accuracy, and direct mass measurement. Its unique capabilities, including direct mass detection, high resolution, miniaturization potential, and versatility, make NEMS-MS an exciting and promising tool to bridge the current gap in commercially available products. It also holds great potential for advancing research in numerous scientific disciplines (Figure 1.4).

1.6 Dissertation Structure

This dissertation comprises five chapters that focus on conducting NEMS-based mass sensing of viruses and nanoparticles under atmospheric conditions. The technique, known as Nanoelectromechanical-based Mass Spectrometry (NEMS-MS), offers a promising approach to weigh particles that are too large for conventional Mass Spectrometry (MS) techniques.

In the opening chapter (Introduction and Background), a comprehensive review of Mass Spectrometry and NEMS-MS is provided. Different ionization techniques, with a particular emphasis on Electrospray Ionization (ESI), are discussed alongside the reasons for selecting ESI for the ionization and transportation of particles and biomolecules. Additionally, this chapter includes a review of emerging tools for large molecules mass sensing that are currently under research.

The second chapter titled (Virus Detection and Sensing Using Atmospheric NEMS-MS) presents the experimental results for virus detection using the proposed system. The working principle of NEMS as mass sensors is explained, and the governing equations are derived and discussed. Detailed information about NEMS device fabrication is provided. The in-house built ionization system and the innovative electrostatic focusing lens are described. This chapter also presents thorough explanations of the experiments conducted for isolating, purifying, and measuring the mass of Severe Acute Respiratory Syndrome Coronavirus 2 (SARS-CoV-2) and Bovine Herpesvirus 1 (BoHV-1). The results are discussed in relation to available measurement techniques and existing literature data.

The third chapter (Dissipation in Atmospheric NEMS-MS) delves into the challenges associated with performing experiments in an atmospheric environment, specifically addressing dissipation caused by viscous damping. This dissertation introduces an innovative method for conducting the sensing process entirely under atmospheric conditions, which has not been explored in the context of NEMS-MS. A review of relevant literature demonstrating this effect is presented, along with a mathematical model to simulate mode shapes and experimental results

showcasing the effect.

The fourth chapter is titled (Microwave-Based Characterization of Nanoparticle Electric Properties) and it introduces another class of sensors operating at electromagnetic domain. The proposed microwave sensor device aims at gather supplementary information of the nanoparticles sprayed. The operational mechanics of the microwave sensor is explained, accompanied by experimental outcomes that validate its feasibility. This suggested device opens up new possibilities for comprehensive characterization and analysis of nanoparticles and biomolecules.

Lastly, in the concluding Chapter 5 (Conclusion), a comprehensive overview of the entire dissertation is presented, encapsulating its key findings and insights. Moreover, this chapter plays a crucial role in showing the different directions that future research could take. We use the findings from our studies to suggest possible areas where other researchers could explore further.

Chapter 2

Atmospheric NEMS-MS for Virus Detection and Mass Measurement

The recent COVID-19 pandemic has highlighted the critical importance of developing a rapid viral detection technique. Current techniques, such as polymerase chain reaction (PCR) and antigen test kits, mainly rely on biochemical detection methods. However, these methods have limitations, particularly in terms of their ability to provide timely results, especially during the initial response phase where quick identification is crucial. This chapter focuses on the detection and mass sensing of viruses using Nanoelectromechanical-based Mass Spectrometry (NEMS-MS).

NEMS-MS offers a promising approach to overcome the limitations of current viral detection techniques. By utilizing NEMS as mass sensors, it enables rapid and precise detection of viruses. This technology provides a potential solution for timely identification and characterization of viral particles, allowing for faster response in controlling and managing viral outbreaks.

Despite its advantages, the current NEMS-MS technology faces certain challenges. One of these challenges is limited throughput, which refers to the number of samples that can be analyzed within a given time frame. Improving the throughput of NEMS-MS systems is crucial for efficient and large-scale viral detection.

Additionally, existing NEMS-MS systems are often bulky and require a vacuum environment for operation. The need for a vacuum adds complexity and limits the portability and practicality of these systems in various settings. Overcoming these challenges is essential to enhance the capabilities and applicability of NEMS-MS technology in viral detection and mass sensing.

2.1 NEMS as Virus Mass Sensors

Nanoelectromechanical Systems (NEMS) have emerged as a promising technique for mass spectrometry, utilizing NEMS structures as mass sensors. These structures are miniaturized devices with at least one dimension in the sub-micron range (*i.e.* $< 1 \times 10^{-6}$m). In NEMS-based mass spectrometry, the sample is ionized, and the molecules or particles are deposited onto a NEMS resonator. The resonator vibrates at specific frequency(ies), and the device response is electronically sensed by nano-sized electrodes. The adsorption of particles on the sensor alters the resonance frequency, primarily decreasing it, due to the increased mass. By analyzing the changes in the resonator frequency, the mass of the deposited ions can be accurately determined.

2.1.1 Working Principle

To comprehend the functioning of NEMS resonators as mass sensors, we must understand how the addition of mass influences the response of the resonating NEMS device. Essentially, the relationship between the measured quantity (*i.e.*, NEMS resonance frequency) and the desired information (*i.e.*, the mass of the particles landing on the beam) need to be established. For simplify, let's assume (as a zeroth-order approximation) that the doubly clamped beam structure is a harmonic oscillator that is modeled as a mass-spring-damper system (Figure 2.1) which follows the following equation of motion:

$$m\ddot{x} + c\dot{x} + kx = F$$

where m is the mass of the resonator, c is the damping coefficient and k correspond to the spring constant. $x, \dot{x}$ and $\ddot{x}$ correspond to the position, velocity and the acceleration of the mass respectively. For this structure the undamped resonance frequency (f_n) is:

$$f_n = \frac{1}{2\pi}\sqrt{\frac{k}{m}}$$

As shown above, for a given resonator, the resonance frequency is inversely proportional to the $\sqrt{m}$. In other words, when a particle lands on the resonator,

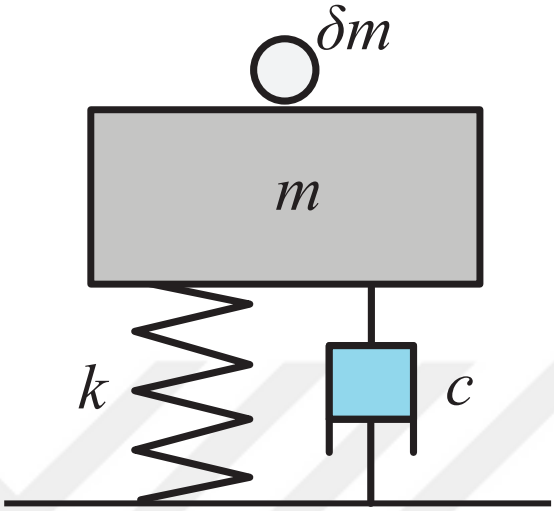

Figure 2.1: Mass-spring-damper system.

increasing its total mass, the resonance frequency decreases.

However, doubly-clamped beams (as the name implies) are fixed from both ends, and the assumption of a mass-spring-damper system is not entirely accurate. Due to the fixed boundary conditions, the resonating beam exhibits varying amplitudes at different points (x) along its length. The deflection amplitude function at each resonance frequency is called the mode shape and can be estimated using Euler-Bernoulli beam theory. If only the first mode is utilized, particles of a specific mass landing at different positions along the beam will cause different frequency shifts, making it impossible to resolve the mass of the particle accurately.

For instance, a particle landing at the center of the beam generates the maximum frequency shift in the first mode, while a particle landing at a normalized distance of $x = 0.3$ produces a lower frequency shift compared to the same particle landing at $x = 0.4$. This implies that the change in the first mode frequency is position-dependent due to the varying mode shape along x and the first mode alone is not sufficient to resolve for the mass of the landing particles. To resolve this dilemma, the first and second fundamental modes (as shown in Figure 2.2) are employed to determine both the mass and landing position of the adsorbed particles.

2.1.2 Estimation of Mass and Landing Position

The estimation of both mass and landing position of analytes desorbed on doubly-clamped NEMS beam was first introduced and employed by Hanay et al. [23] using the first and second fundamental out-of-plane modes. This method was applied to determine the mass and landing position of IgM antibody isoforms and gold nanoparticles. By utilizing this approach, the influence of the landing position can be accounted for, allowing for the construction of position-independent mass spectra of particles. This results in improved mass spectra compared to those obtained using a single mode measurement.

In this model, the adsorption of analytes on the surface of a doubly-clamped structure is treated as point particles, resulting in localized changes in the mass distribution of the beam at the landing position. The mass of the point particle (Δm) that lands on a specific location $x = a$ on the NEMS resonator with a total mass (M) causes a decrease in the resonator's frequency across all modes (Δf_n), as expressed in the following equation [23]:

$$\Delta f_n = -\frac{f_n}{\alpha_n M} \Delta m \phi_n(a)^2 \tag{2.1}$$

Where f_n is the n$^{\text{th}}$ resonance frequency of the NEMS resonator and $\phi_n(a)$ denoting the n$^{\text{th}}$ resonance mode shape (*i.e.*, the normalized displacement profile) at the normalized landing position ($x = a$). The mode shape functions in the first and second modes are shown in figure 2.2.

The term α_n is computed as follows:

$$\alpha_n = 2 \int_{a=0}^{a=1} \phi_n(a)^2 da \tag{2.2}$$

This factor is important for the estimation of the effective mass in each mode ($M_{eff}^{(n)}$) which scales the inertia term in the equation of motion. The calculation of $M_{eff}^{(n)}$ is conducted as follows:

$$M_{eff}^{(n)} = (\alpha_n/2)\, M \tag{2.3}$$

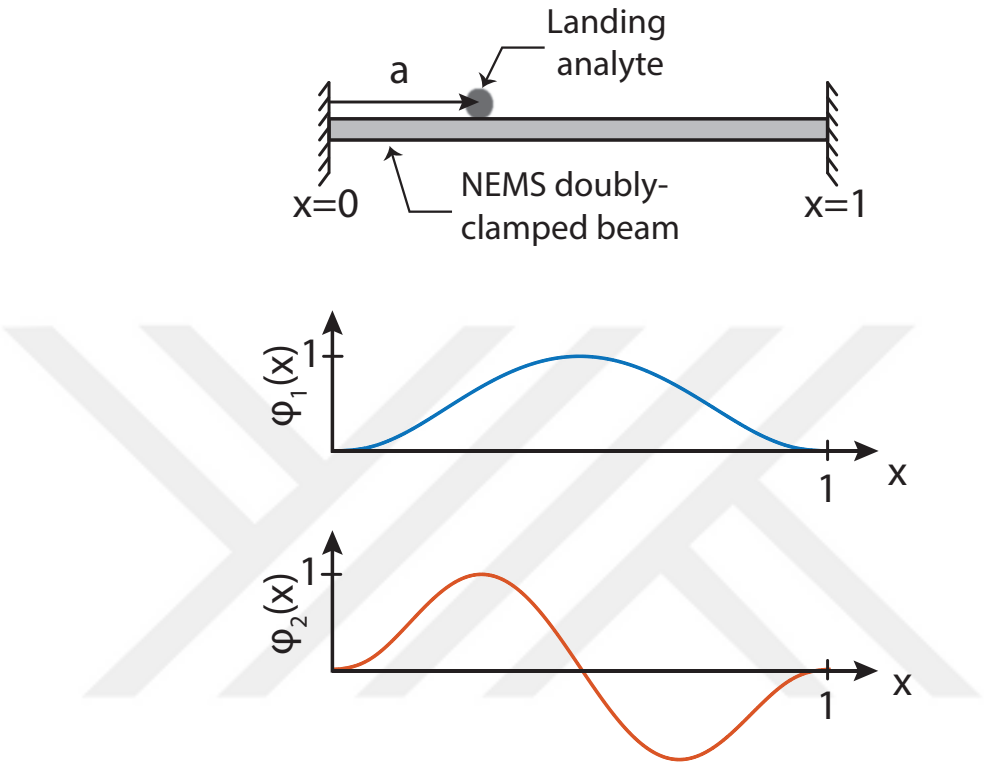

Figure 2.2: First and second fundamental out-of-plane mode shapes of doubly-clamped beams.

The effective mass scales the inertia term in the equation of motion. Next we define the normalized mass change (δm) and normalized frequency shift in the n^{th} mode as follows:

$$\delta m \equiv \Delta m / M \tag{2.4}$$

$$\delta f \equiv \Delta f / f_0 \tag{2.5}$$

Now one can re-write equation (2.1) in the first and second modes as follows:

$$\delta m \phi_1(a)^2 = -\alpha_1 \delta f_1 \tag{2.6}$$

$$\delta m \phi_2(a)^2 = -\alpha_2 \delta f_2 \tag{2.7}$$

Now this is a set of two equations with two unknowns with the unknowns being the mass of the analyte (quantified by its normalized mass change δm) and its landing position (a).

By considering the symmetry of the mode shapes about the center of the beam (Figure 2.2), the landing position of the analyte can be estimated by measuring the ratio of the frequency shifts as follows:

$$a = G^{-1}\left(\frac{\alpha_1 \delta f_1}{\alpha_2 \delta f_2}\right) \tag{2.8}$$

Where the function $G(x)$ is defined as follows:

$$G(x) \equiv \phi_1(x)^2 / \phi_2(x)^2 \tag{2.9}$$

Additionally, the analyte mass can be estimated By isolating the variable (δm) in either equation (2.6) or ((2.7)) as follows:

$$\delta m = \frac{-\alpha_1 \delta f_1}{\phi_1(a)^2} = \frac{-\alpha_1 \delta f_1}{\left(\phi_1\left(G^{-1}\left[\delta f_1, \delta f_2\right]\right)\right)^2} \tag{2.10}$$

Note that the use of inherit symmetry in the mode shapes facilitates finding the mass and the landing position of the analytes. However, the landing position found can either be (a) or it can have the value of its complimentary (*i.e.*, $1-a$). In other words, the landing position value can be either measured from the right or left electrode and it is not possible to deduce the side of landing with the two-mode method. However, since the objective here is to measure the mass of landing analytes and construct a position-independent mass spectra, this method was found sufficient.

For a comprehensive derivation of the mathematical model, please refer to the Supplementary Information provided in reference [23]. Additionally, the

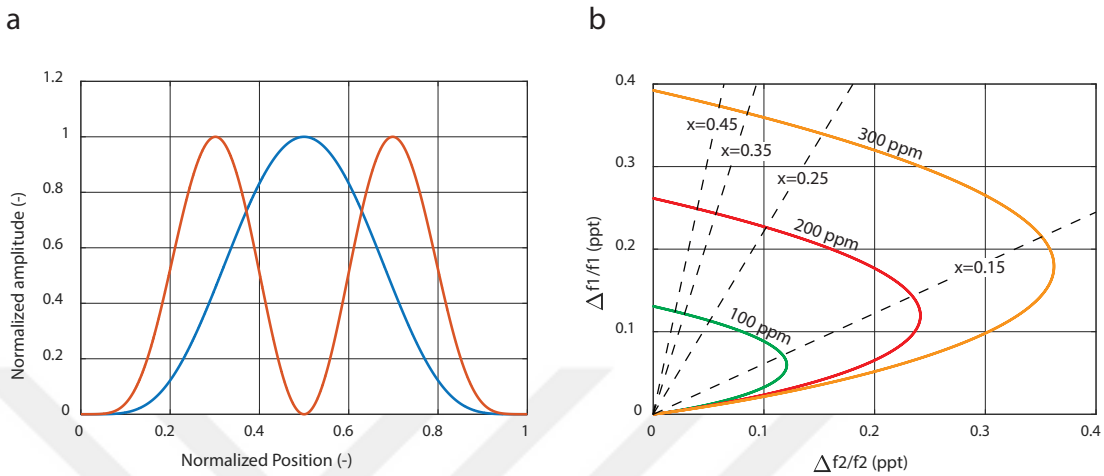

Figure 2.3: Mode shapes and resulting frequency shifts in the first and second modes. Different mass values are presented by different crescent-like contours and different landing positions are presented as lines with different slopes.

aforementioned reference have a dedicated section for modelling the frequency noise in the first and second modes and how they correlate. Joint-probability density function formalization is used to find the estimated error in the mass and position calculations.

Figure 2.3b presents the different mass solutions on the δf_1 *vs.* δf_2 plane. Three mass solutions namely 100, 200 and 300 ppm (*i.e.*, mass analyte over beam total mass equal to 0.01, 0.02 and 0.03 respectively) are plotted for all landing positions (*i.e.*, from $x = 0$ to $x = 0.5$). The dotted lines illustrate the solution of a specific landing position.

2.1.3 Device Fabrication

The fabrication process of the NEMS sensor involves three major steps. Firstly, the doubly clamped beam along with the actuation and read-out electrodes are patterned through two steps e-beam lithography (EBL) (Figure 2.4a-f). Secondly, the NEMS structure is suspended through dry etching (Figure 2.4g-j) and Lastly, the electrostatic polymeric focusing lens is created and aligned with the NEMS device (Figure 2.4k-l).

The NEMS sensor was fabricated from a commercially available (Univeristy-Wafer, Inc.) 100 nm-thick stoichiometric low stress silicon nitride (SiN) film that was grown using low pressure chemical vapor deposition (LPCVD) technique on top of a 500 µm silicon substrate (Figure 2.4a). The wafer is cut into 28×28 mm sized chips which each will include an array of 49 NEMS devices each is 4×4 mm when diced. The array size is limited by the maximum size allowed in the EBL chamber.

The process begins with the metallization of the actuation and read-out electrodes, along with the contact pads. This involves spin coating of poly(methyl methacrylate) (PMMA) as depicted in Figure 2.4b and using EBL with the first mask (Figure A.1) to pattern the electrodes and pads (Figure 2.4c). After developing the PMMA, a 5 nm chrome adhesion layer followed by a 70 nm gold layer were deposited through thermal evaporation. Subsequently, a lift-off technique is employed in an acetone bath to retain the metal within the patterned area (*i.e.*, the electrodes and pads) as illustrated in Figure 2.4d.

Next, a second EBL process is performed to define the NEMS structure, which includes the doubly-clamped beam and the clamping region. This step involves spin coating of PMMA (Figure 2.4e) and patterning the nitride mask shown in figure (Figure A.5) using EBL. The schematic of the structure is shown in Figure 2.4f after the development. Next, the chips are properly packaged and sent to another cleanroom facility to proceed with the fabrication.

The chips are then placed in thermal evaporation to deposit a 40 nm Copper (Cu) layer (with a maximum deposition rate of 1 Å/s). Lift-off is performed after the Cu deposition (Figure 2.4g) and the resulting layer serves as a hard mask for suspending the beam in the subsequent stages. Before suspending the NEMS structure, the wafer is diced into individual 4×4 mm chips. The dicing is done at this stage as the dicer might damage the delicate NEMS structures after suspension.

Next, an anisotropic dry etch was carried out for silicon nitride layer to define the structure (Figure 2.4h), followed by an isotropic dry etch for the silicon to suspend the structure (Figure 2.4i). The dry etching is performed using an Inductively Coupled Plasma (ICP) with the recipes and etching parameters shown in Table 2.1.3. Finally, the copper hard mask was removed using a wet etchant (Al-80) which include a mixture of nitric acid, phosphoric acid and acetic acids (Figure 2.4j).

In order to increase the efficiency of NEMS devices, another process based on photolithography was developed to construct the polymeric lensing structure. For ease of fabrication, we employed a commercial photoresist (Microchemicals GmbH, AZ 4533) to form the polymeric lens. The high viscosity photoresist was spin coated @3000 rpm for 1 minute to form a 3.5 µm layer over the NEMS structure (Figure 2.4k). A mask aligner (EVG620) was then utilized with a Photolithography mask to align the mask and expose the beam area with UV light. The mask comprises a rectangular section measuring 20µm × 15 µm and alignment marks to facilitate aligning the rectangular section with the NEMS structure. Subsequently, the exposed photoresist was developed, resulting in the creation of an electrostatic polymeric lensing structure with a window aligned over the sensor (Figure 2.4i). Additionally, during the same process step contact pads for wirebonding were opened approximately 400 µm away from the NEMS sensor.

At this stage, we have fabricated a fully working device that can be wirebonded and used for mass sensing experiments. A colorized SEM image of the resulting NEMS device is shown in figure 2.5. The suspended SiN beam along with the set

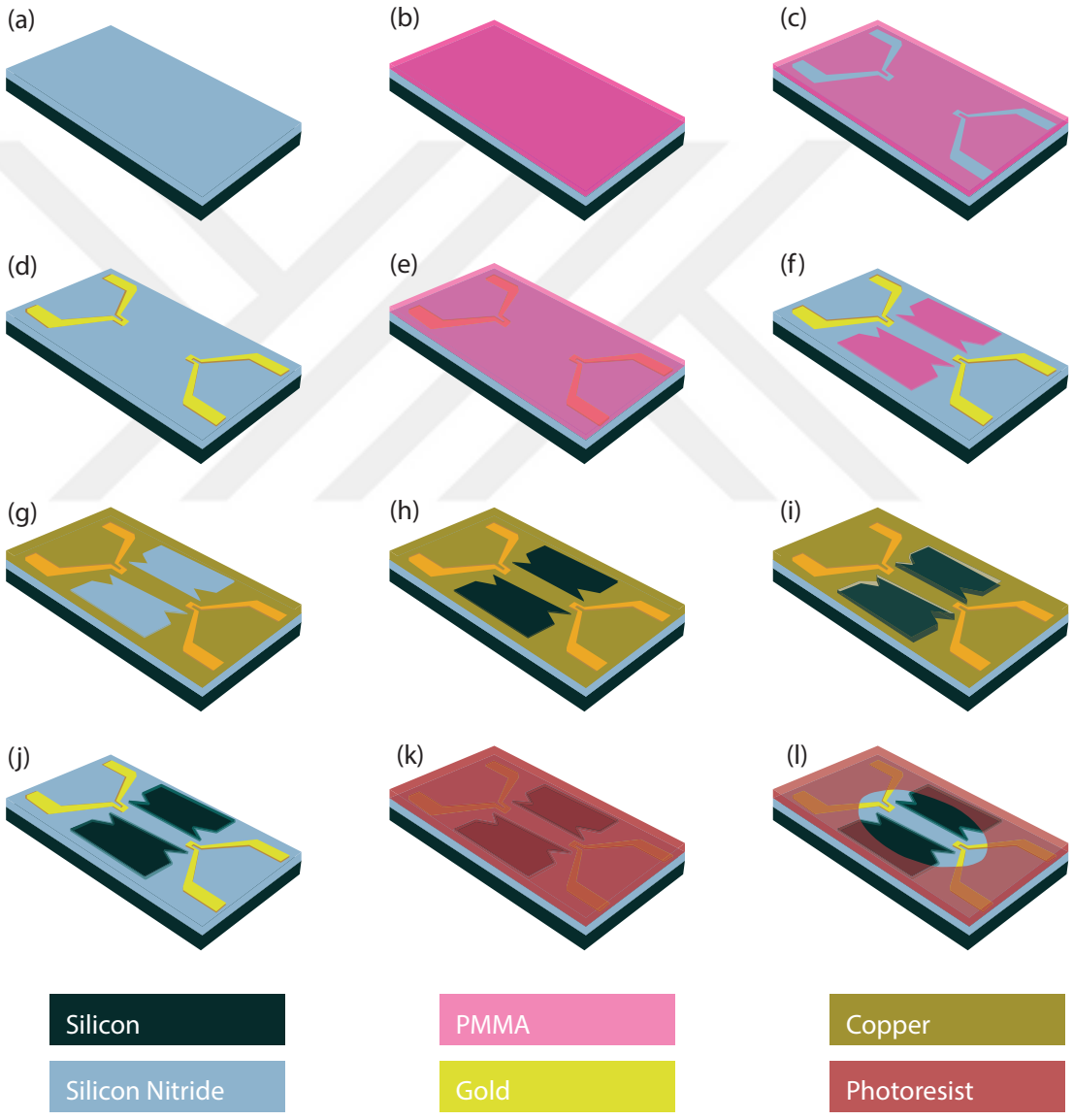

Figure 2.4: Fabrication steps for self-focusing NEMS device.

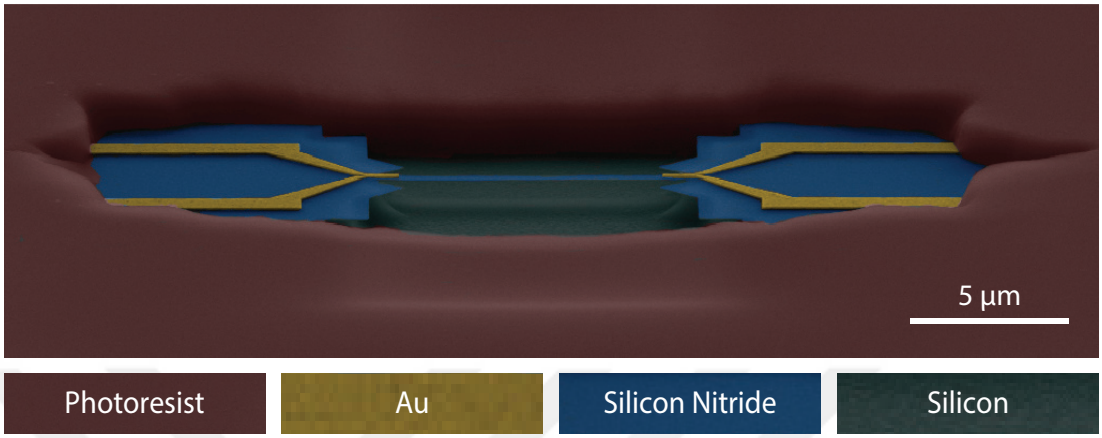

Figure 2.5: Colorized SEM image of the fabricated self-focusing NEMS device.

of Au electrodes constitute the NEMS device and the photoresist layer with the opening in the center constitutes the ion lens for focusing the incoming particles.

Table 2.1: Inductively Coupled Plasma (ICP) etching recipe and parameters for Silicon and Silicon Nitride layers.

Parameter	**Anisotropic Si_3N_4**	**Isotropic Si**
Etchant gas	CF_4	SF_6
Etchant flow rate (sscm)	20	15
Passivation gas	CHF_3	
Passivation flow rate (sscm)	3	2
Coil power (Watt)	400	150
Platen power (Watt)	100	30
Pressure (mtorr)	5	10
Temperature (°C)	25	
Duration (s)	60	240

2.2 Electrospray Ionization

2.2.1 Electrospray Ionization Working Principle

The nanoparticles and viruses measured in this study were produced and sprayed toward the NEMS sensor using an in-house Electrospray Ionization (ESI) setup. ESI is a soft-ionization technique that generates charged individual particles in the gaseous phase without causing fragmentation, in contrast to hard-ionization methods.

In ESI, the sample is pumped through a nozzle or tip that is held at high-voltage typically in the kV range. As illustrated in figure 2.6, the process creates a liquid meniscus (also known as the Taylor cone) which emits charged micro-droplets containing the particles or molecules of interest. As these droplets travel towards the NEMS chip, which is maintained at ground voltage, they undergo evaporation, reducing their size while retaining their initial charge. When the droplets reach a critical point known as the Rayleigh limit, the droplet can no longer hold the preserved charge, leading to Coulomb fission. This results in the explosion of the droplet, generating smaller nanodroplets. The charge is distributed among these newly formed droplets, and this process continues at smaller scales until single nanoparticles, viruses, or biomolecules are ionized.

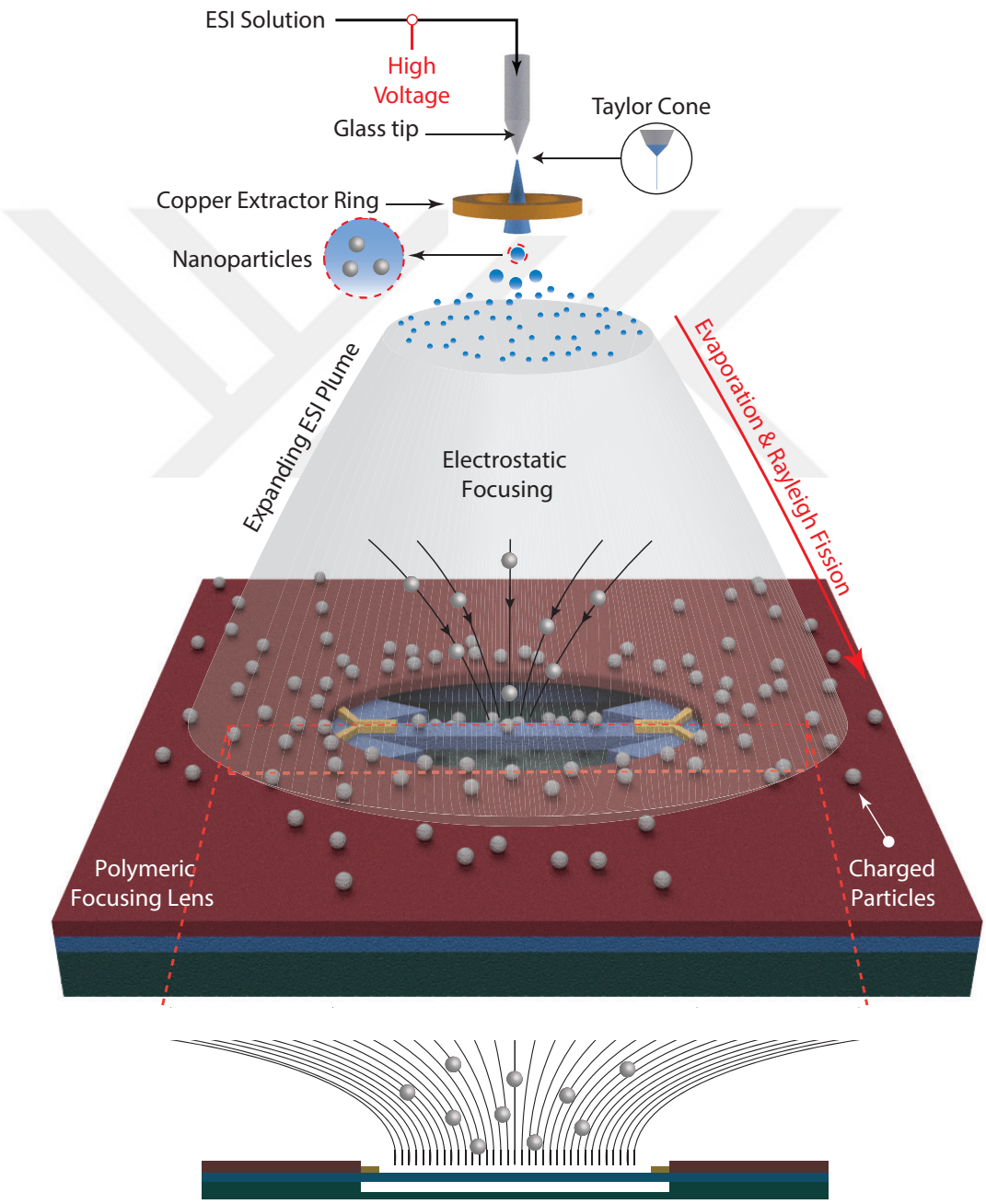

Figure 2.6: Electrospray Ionization and electrostatic focusing of nanoparticles.

2.2.2 Electrostatic Focusing

In the majority of the NEMS-MS experiments conducted thus far, the charged droplets generated from ESI are subsequently transported via a pressure gradient to a vacuum setup, where focusing toward the NEMS device and detection occur. An illustrative instance of such a setup is depicted in Figure 2.7, which has been adapted from [2, Sergio Dominguez-Medina et al., Neutral mass spectrometry of virus capsids above 100 megadaltons with nanomechanical resonators. Science 362, 918-922(2018). DOI:10.1126/science.aat6457] and reprinted with permission from AAAS.

The vacuum setup serves two primary purposes. Firstly, it increases the quality factor of NEMS, thereby improving the resolution of the technique. Secondly, and more importantly, it plays a crucial role in facilitating the focusing of nanoparticles towards the NEMS surface, as conventional ion optics functions effectively only under vacuum conditions [39, 40].

However, in this study, an innovative technique was developed to enhance the efficiency of NEMS-MS without the need for bulky differential vacuum systems or complex ion lenses. The technique utilizes the incoming charged ions to effectively charge a polymeric lens integrated on top of the NEMS device. As the on-chip insulating layer accumulates the charge, it creates a bias voltage that focuses the incoming flux towards the NEMS sensor (Figure 2.6).

This advancement has enabled us to operate under atmospheric conditions (*i.e.*, room temperature and atmospheric pressure) and achieve efficiency values that surpass the previous state-of-the-art by two orders of magnitude [2, 15].

The concept of electrostatic focusing of charged nanoparticles drew inspiration from previous studies [41, 42]. In these studies, a charged aerosol containing nanoparticles was generated and directed towards an insulating layer featuring nanoscale [41] or microscale [42] openings. These openings were fabricated directly on a chip through lithography techniques. As a result of the accumulation

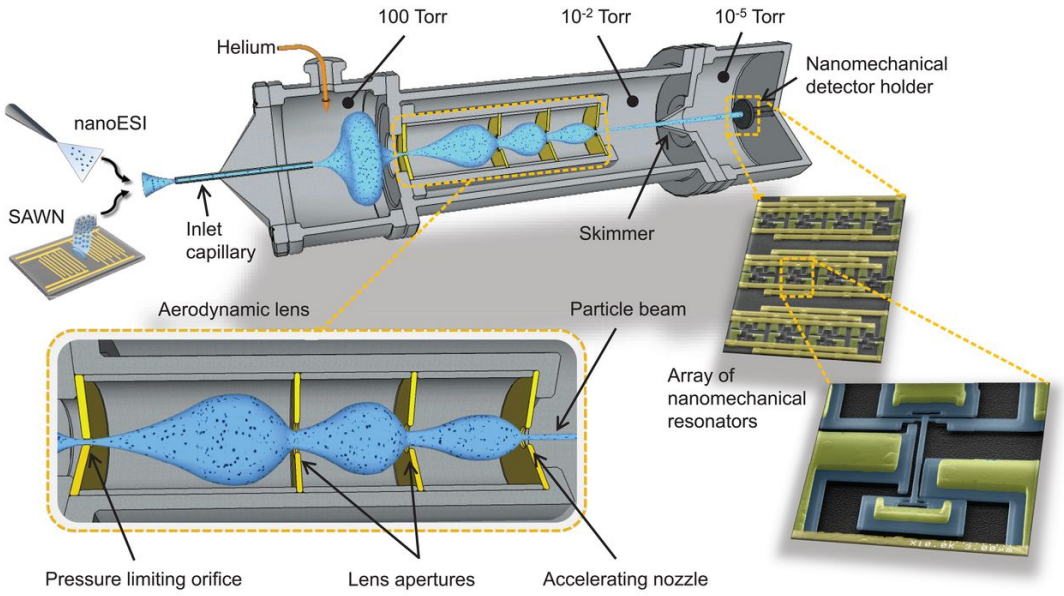

Figure 2.7: Architecture of the particles and molecules transmission system in the previous state-of-the-art. Adapted from [2, Sergio Dominguez-Medina et al., Neutral mass spectrometry of virus capsids above 100 megadaltons with nanomechanical resonators. Science 362, 918-922(2018). DOI:10.1126/science.aat6457]. Reprinted with permission from AAAS.

of electrostatic charge on the insulating layer, the nanoparticles were concentrated within the open features. While the technique of electrostatic focusing of nanoparticles had been previously accomplished, the results presented in this dissertation marks the first application of electrostatic focusing within the context of NEMS-MS [4].

2.2.3 ESI Setup and Parameters

The developed ESI system, depicted in Figure 2.8, begins with a glass Hamilton syringe (Hamilton 1750 Series) containing the ESI solution. The solution is pumped at a rate of 500 nL/min using a syringe pump (New Era Pump Systems, NE-1000) through a 360 µm capillary (LabSmith, CAP360–150S). To ensure stability, the capillary is inserted into a dry-box, isolating the rest of the ESI setup from environmental changes, such as humidity caused by the laboratory's air conditioning.

The capillary is connected to a high-voltage MicroTee connector (New Objective, MICT-PV), maintained at a voltage of 5.5 kV. The high voltage required to ionize the solution was provided by a high-voltage convertor (American Power Design, Inc. P2-600/C/Y) with input voltage of 10.8V supplied by a DC power supply (Agilent E3640A). On the other end of the Tee connector, a fused silica pulled capillary (New Objective, PicoTip Emitter SilicaTip) is connected, with one end pulled to a diameter of 10-30 µm.

Downstream from the spraying tip, an extractor lens is positioned to facilitate extracting charged droplets from the Taylor cone. This extractor lens is placed approximately 3-5 mm away from the spraying tip and consists of a copper plate with a 15 mm opening, held at a voltage of 1.3 kV. The extraction voltage was supplied by a DC high-voltage convertor (American Power Design, Inc. P2-600/C/Y) connected to DC power supply (Marxlow RXN-1502D) set at 3V. At a distance spanning from 75 mm to 150 mm from the extractor lens, the NEMS chip with the embedded polymeric lens is situated, where incoming particles are detected and measured. At the outset, the ESI parameters were established in alignment with those outlined in [43] and were subsequently fine-tuned for optimization.

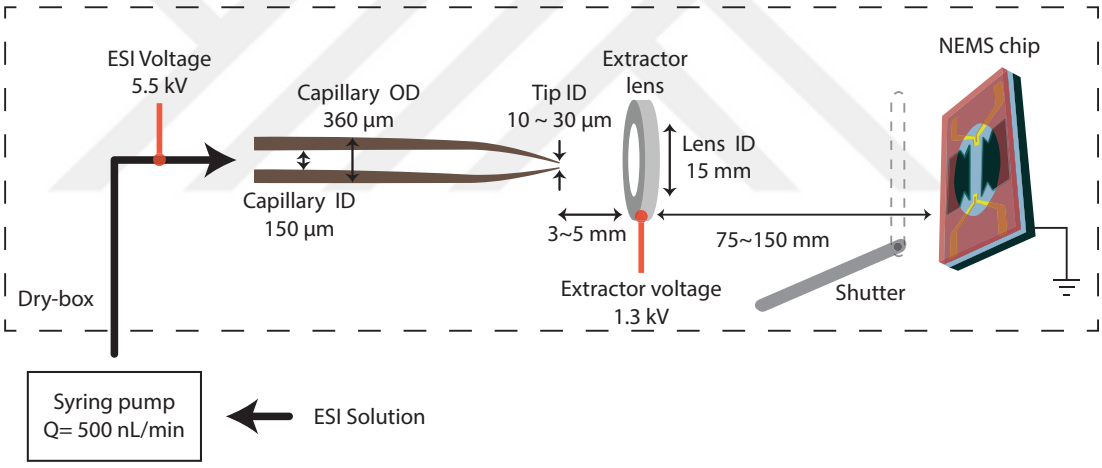

Figure 2.8: Illustration of ESI system with the dimensions and process parameters.

2.3 Virus Isolation and Sample Preparation

2.3.1 Isolating SARS-CoV-2 from Cell Culture

Prof. Aykut Ozkul of Ankara University provided a lysate of Vero E6 cells infected with acute respiratory syndrome coronavirus 2 (SARS-CoV-2). This particular virus strain was isolated from individuals who tested positive for COVID-19 using real-time reverse transcription polymerase chain reaction (RT-PCR). The samples for virus isolation were collected at the Infectious Disease Clinics, Ankara City Hospital with the official permission No. 20-654, 21.05.2020 obtained from the Ministry of Health, Ankara City Hospital, Ethical Committee for Human Experiments. Nasopharyngeal swabs were collected from these individuals and immediately placed in Dulbecco's Modified Eagle's Medium (DMEM, Thermo Fisher) supplemented with 10% Fetal Bovine Serum (FBS) and penicillin-streptomycin (Lonza, Switzerland). The collected swabs were then used to infect Vero E6 cells (ATCC, CRL-1586), which were incubated at 37°C in DMEM and monitored for cytopathic effects. To purify the virus isolates, plaque assays were performed three times consecutively.

The stock virus solution was produced by infecting Vero E6 cells in T75 cell culture flasks with the virus isolated from the three consecutive plaque assays. Once cytopathy reached 80% of the cellular monolayer, the cells were frozen and thawed twice to ensure lysis. The resulting cell lysate had an infectivity titer of 2×10^6 PFU/mL and was clarified by centrifugation at 1030 relative centrifugal force (RCF) for 15 minutes at 4° C (Allegra X-30, Beckman Coulter, USA). The supernatant was collected and thermally inactivated for safety purposes at 60°C for 90 minutes, then stored at −80° C.

2.3.2 Isolating BoHV-1 from Cell Culture

The Bovine Herpesvirus Type 1 Cooper strain (BoHV-1 Cooper, ATCC VR864) was obtained from the same source outlined above and cultivated in Madine

Darby Bovine Kidney (MDBK, ATCC CCL-22) cells in a similar fashion to how SARS-CoV-2 viruses were cultivated as detailed earlier.The stock virus solution was obtained from MDBK cells infected with virus isolates after three consecutive plaque assays. Cells showing 80% cytopathy were subjected to 2 freeze-thaw cycles to lyse the cells, and then clarified using centrifugation. Infectivity titer showed a concentration of 1×10^7 PFU/mL. The virus was thermally inactivated at 60° C for a period of 90 min and preserved at −80° C for further processing.

2.3.3 Virus Precipitation & Purification

Both SARS-CoV-2 and BoHV-1 were subjected to identical procedures to separate and purify the viral sample prior to ESI spray. To harvest the virus sample, a freeze-thaw cycle was applied twice to lyse the cell culture. Subsequently, the cell lysate underwent centrifugation to eliminate cellular debris, followed by a brief thermal inactivation step for safety reasons. To selectively separate the virus from the cellular debris present in the lysate, a Polyethylene glycol (PEG) virus purification kit (Abcam, UK) was utilized. Initially, a 500 µL aliquot of the cell lysate was diluted with 1 mL of HPLC water (Sigma-Aldrich, USA). Subsequently, 250 µL of the PEG-6000 solution from the precipitation kit was added to the diluted lysate, and the mixture was left to agglomerate overnight at 4 °C for 16 hours. The PEG-lysate solution was then centrifuged at 3200 RCF for 30 minutes at 4 °C (himac CT 15RE, Hitachi, Japan). The supernatant was carefully removed by aspiration, while retaining the visible white pellet. The pellet was re-suspended in 100 µL of the re-suspension solution provided with the precipitation kit, using careful pipetting to ensure proper mixing.

To eliminate the PEG molecules from the purified virus mixture, a salting-out process was employed. A total of 33 µL of 50 mM Tris-HCl buffer containing 4 M of KCl (pH 7.3)was added to 100 µL of the PEG-virus mixture. The solution was then incubated on ice for 30 minutes and subsequently centrifuged at 12,000 RCF for 10 minutes. The supernatant, which contained the virus, was carefully collected without disturbing the pellet. The supernatant was further diluted with

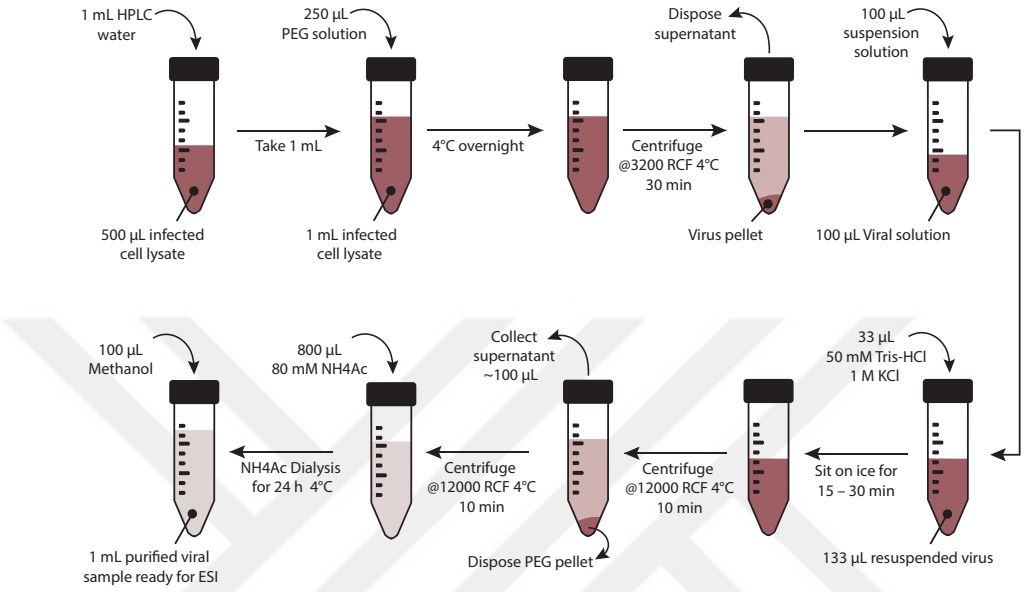

Figure 2.9: Virus sample PEG precipitation and purification.

867 µL of 80 mM ammonium acetate buffer with pH of 7.1 from (Merck Millipore, USA).

To remove nonvolatile salts from the purified virus solution, dialysis was performed using a Pur-A-Lyzer Maxi dialysis kit with a molecular weight cutoff of 12 kDa (12kDa MWCO, Sigma, USA). An 80 mM ammonium acetate buffer (pH 7.1) was prepared in advance and kept at 4 °C. The PEG-purified virus solution (1 mL) was placed inside the dialysis tube and suspended in 1 L of ammonium acetate at 4° C for 24 hours. After completion of dialysis, the sample was retrieved from the dialysis tube and used as is. The nonpurified cell lysate was dialyzed in a similar manner. A 12 kDa dialysis tube was filled with 1 mL of cell lysate, which was then suspended in 1 L of ammonium acetate for 24 hours at 4° C. The dialyzed cell lysate was collected and used without further modification. To facilitate efficient electrospraying, HPLC grade, triple filtered using 220 nm syringe filter 10% v/v% methanol was added to each virus-containing solution in ammonium acetate buffer prior to the experiment. The PEG precipitation and purification is shown in figure 2.9.

2.4 Experimentation

2.4.1 Actuation and Read-out Scheme

In order to track the change in resonance frequency in the first and second fundamental modes, a phase-locked loop (PLL) circuitry is used in conjunction with the doubly-clamped beam (Figure 2.10). The beam has a pair of gold electrodes deposited, one on each side, where one is used for actuation and the other is utilized for transduction of the beam's movement. The structure is brought to resonance thermo-elastically, meaning that alternating thermal stress is applied to one of the sides. Due to the mismatch in thermal expansion coefficients between the deposited gold electrodes and the underneath Silicon Nitride beam, applying alternating current to the nano-scaled electrodes causes heating of the electrode, inducing thermal stress that drives the NEMS device at a specific frequency. As the transduction electrode, located on the opposite side of the drive electrode, moves, its resistance undergoes modulation. This modulation can be utilized to read the resonance frequency of the beam, and this detection mechanism is known as piezo-resistive detection [44]. For a comprehensive review of different mechanical motion transduction mechanisms in NEMS, the reader is referred to [45].

The combination of thermo-elastic actuation and piezo-resistive transduction offers several advantages, such as maintaining an entirely electronic measurement scheme instead of relying on bulky optical detection. Both the phase-locked loop (PLL) frequency tracking and open-loop frequency measurements were conducted using a Lock-in-Amplifier (Zurich Instruments, HF2LI). The circuitry includes a bias tee (Mini-Circuits, ZFBT-4R2GW) and a low-noise amplifier (Mini-Circuits, ZFL-1000LN). The lock-in amplifier can superimpose two independent signals and measure the NEMS response through phase-locked detection via the same port. The PLL option available in the HF2LI was employed to set the controller parameters and perform the PLL frequency tracking.

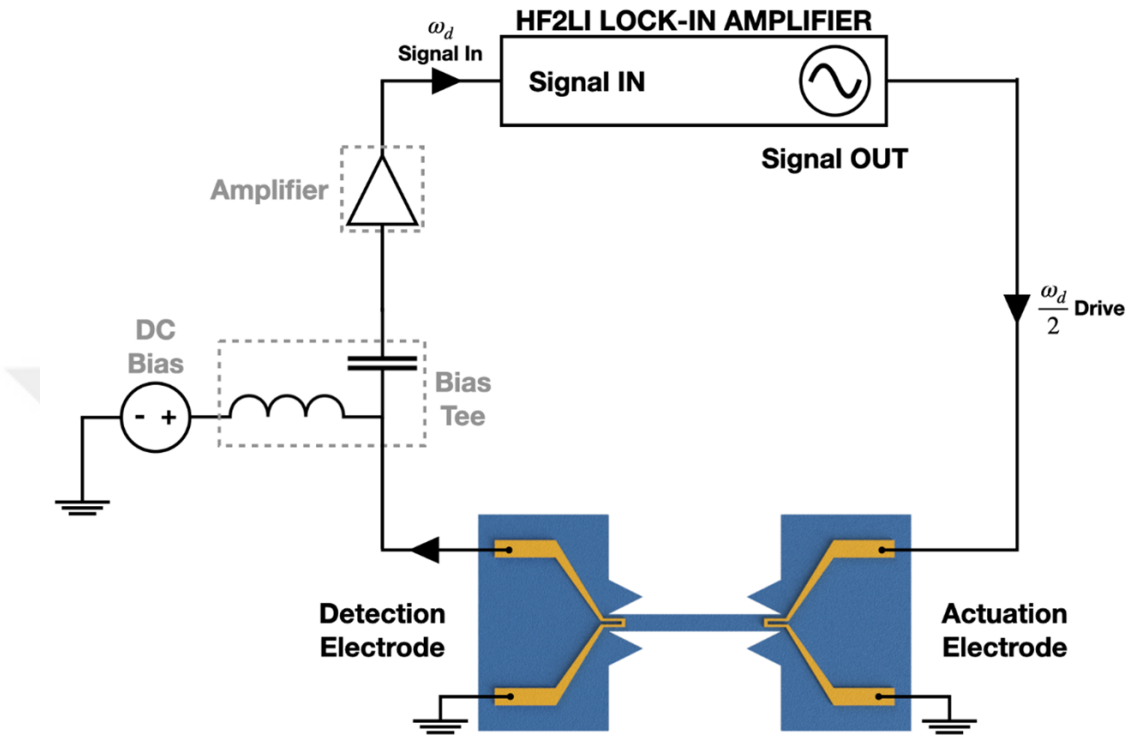

Figure 2.10: NEMS drive and read circuitry using Lock-in amplifier.

2.4.2 Optimization of ESI System and Electrostatic Focusing

Before conducting experiments involving viruses, the electrospray ionization (ESI) system underwent testing using fluorescent polystyrene nanoparticles (f-PSNP). The purpose of this testing was to ensure that the ESI setup was functioning as intended and that electrostatic focusing was indeed taking place. For this particular experiment, 200 nm polystyrene nanoparticles (G200, Thermo Fisher) were utilized. The spraying process was directed onto a blank silicon chip with on-chip polymeric lens but with no NEMS device (see Figure 2.11a).

After optimizing the parameters and running the ESI for 10 minutes, remarkable focusing of the nanoparticles was observed within the aperture, as depicted in the fluorescent microscopy image (Figure 2.11b). The contrast in particle quantities entering the opening versus those outside, can be clearly seen. The optimized parameters are presented in Figure 2.8 and summarized in Table 2.2.

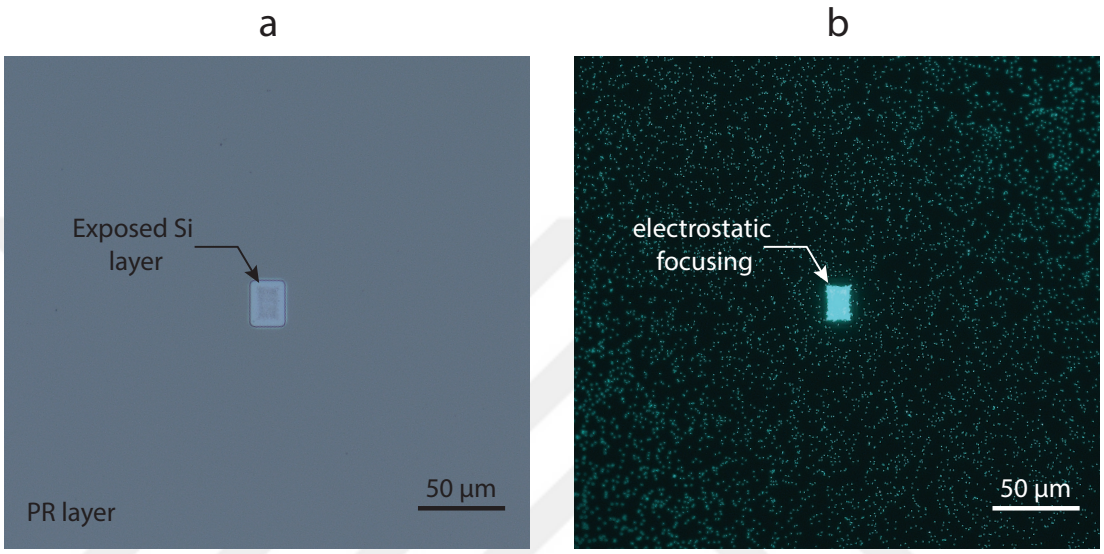

Figure 2.11: Demonstration of electrostatic focusing of 200 nm fluorescent PS nanoparticles.

Table 2.2: Electrospray Ionization system parameters.

Parameter	Value
ESI voltage	5.5 kV
Extractor lens voltage	1.3 kV
Tip inner diameter	10-30 µm
Extractor inner diameter	15 mm
Tip to extractor spacing	3-5 mm
Extractor to NEMS spacing	75-150 mm
Flow rate	500 nL/min

2.5 Two Modes Measurements & Data Analysis

After configuring the PLL parameters and resonating the NEMS device simultaneously in the first and second out-of-plane modes, and optimizing the ESI parameters while ensuring electrostatic focusing, the shutter separating the NEMS device and ESI system is opened. This allows the ionized particles to reach the NEMS device. Once the shutter is removed, the change in the first and second mode frequencies due to a particle landing event can be seen in real-time in the user interface of the lock-in amplifier (Zurich Instruments, LabOne) as illustrated in Figure 2.12.

Once a sufficient number of particles is collected or if the PLL control is lost, the shutter is closed, and the lock-in amplifier channels are turned off to stop the actuation of the NEMS beam. The PLL data, including time, frequency, phase, and amplitude for both the first and second modes, are imported into the MATLAB workspace. A custom program is then used to identify the landing events of analytes and calculate the corresponding frequency shifts for each event.

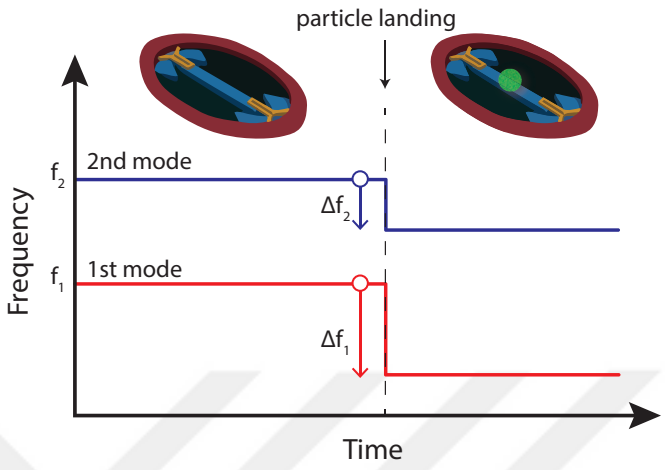

Figure 2.12: Frequency shifts on fundamental modes of NEMS caused by a particle landing event.

2.5.1 Event Finding Algorithm

The initial step involves plotting the raw data and determining the start time (t_1) and end time (t_{end}) of the experiment. These times correspond to when the shutter was opened and closed, respectively as shown in the PLL data plotted in Figure 2.14. Since the landing of analyte creates a sudden change in the frequency measurement, analyzing the frequency data slope helps locating the landing events and they appear as distinct local minima in the slope data.

However, in some cases, there may be smaller local minima that are very close to the noise floor (Figure 2.15). To ensure an automated event finding process and to ensure the code detects specific parameters related to landing events, a sweeping step is introduced. The minimum threshold for the slope and the minimum prominence value are varied between two extreme scenarios, counting the number of possible events for each parameter combination. In one scenario, the parameters are set to high values that result in no event detection, while in the other scenario, all local minima (including noise) are counted as events.

Since the number of landing analytes is limited compared to the total local minima in the PLL data that correspond to noise, a distinctive feature is identified in the sweeping plot, and the parameter combination is selected just before the

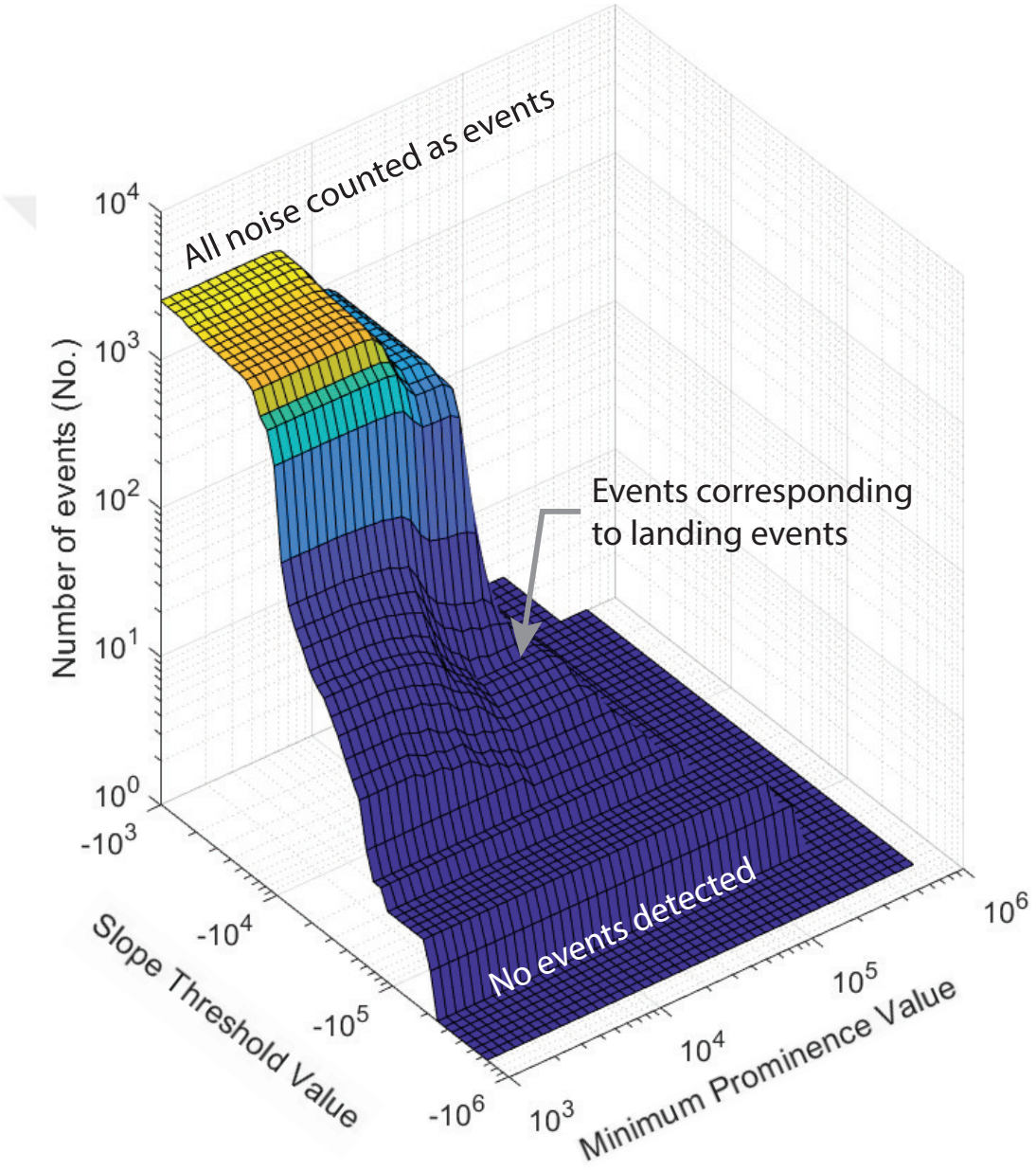

Figure 2.13: 3D plot of sweeping the minimum prominence and minimum slope threshold.

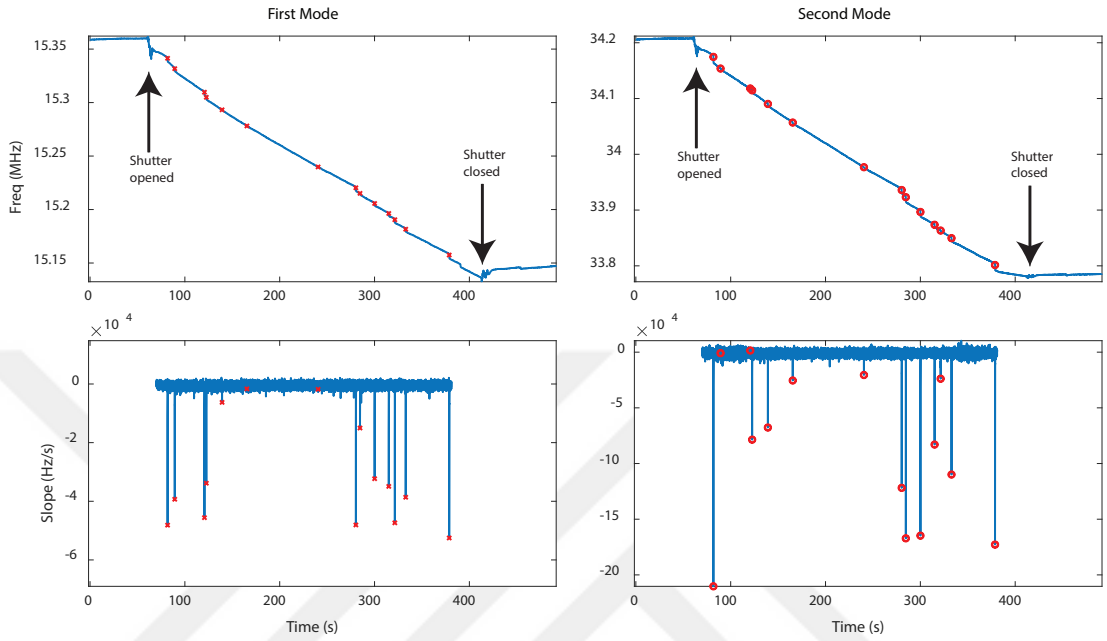

Figure 2.14: Frequency PLL data of the first and second modes along with its calculated slope.

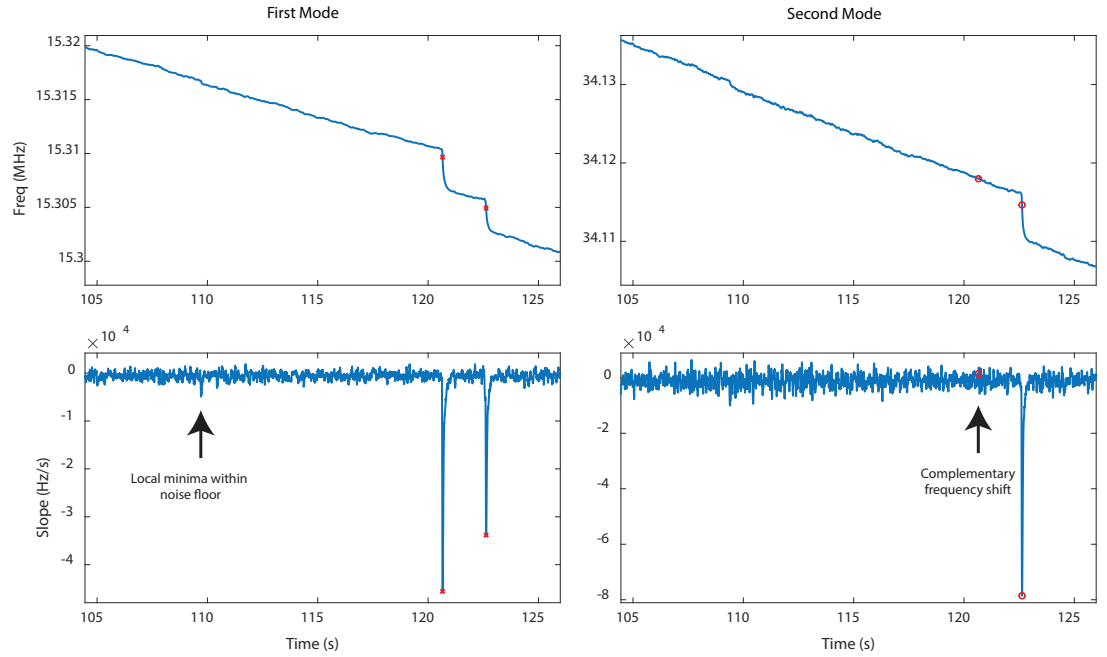

Figure 2.15: Zoom-in to frequency PLL data of the first and second modes. Zoom-in illustrates an instance of local minima within the noise and a detection of an event in a single mode.

number of possible events increases significantly (indicating the inclusion of noise as events). After this step, the events are plotted on the PLL data and iterated if necessary. If an event is detected in one mode only, the complementary frequency shift in the other mode is automatically estimated from the PLL data.

For each event, the frequency shifts (Δf_1 and Δf_2) in the first and second modes, as well as the initial frequencies (f_1 and f_2) of the first and second modes just before the frequency shift, are calculated. These values are then used to determine the mass and position of each landing event. Events with frequency shifts below the noise threshold or outliers above a certain threshold are excluded from further analysis.

Note that figures 2.14 and 2.15 correspond to previous experiments conducted with 40 nm Gold nanoparticles (GNP) as calibration particles.

2.5.2 NEMS-MS Resolution

The next step involves calculating the Allan deviation to determine the resolution of the NEMS-MS technique and the minimum detectable mass. The Allan deviation is a measure of frequency stability at different time scales. In the case of the device used in the experiments shown in figures 2.14 and 2.15, the Allan deviation is calculated from the time when the shutter is closed. The calculated Allan deviation at the PLL time constant (140 ms) is 2.15 ppm for the first mode and 1.24 ppm for the second mode, as shown in figure 2.16.

The mass resolution, or minimum detectable mass (Δm_{min}), can be determined using the following equation:

$$\Delta m_{\text{min}} = \sqrt{2} \times M_{\text{NEMS}} \times \sigma_{\text{Allan}} \tag{2.11}$$

Here, M_{NEMS} represents the mass of the NEMS beam, and σ_{Allan} is the best Allan deviation calculated at the PLL time scale. For the device used in the

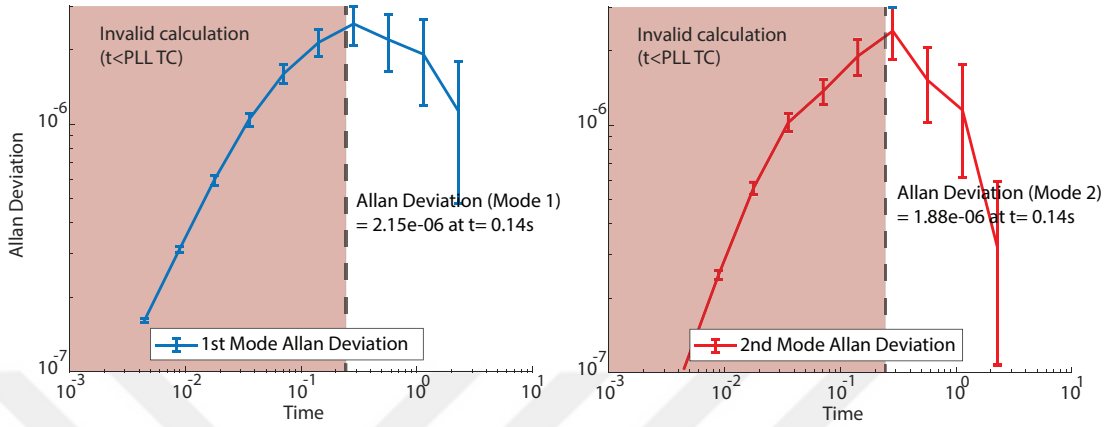

Figure 2.16: Allan deviation calculation for NEMS device calculated when shutter was closed. PLL time constant = 140 ms.

experiments shown in figures 2.14, 2.15, and 2.16, where $M_{\text{NEMS}} = 2937$ fg and $\sigma_{\text{Allan}} = 1.24 \times 10^{-6}$, the mass resolution is $\Delta m_{\text{min}} = 2.2$ MDa. This resolution is excellent for weighing particles larger than the 100 MDa range.

2.5.3 Mass Calculation

In order to calculate the mass and position of the detected events, it is necessary to have prior knowledge of the mode shape, which represents the normalized displacement profile at resonance. Since this work relies on an all-electronic actuation and read-out scheme, optical measurement setups to directly measure the displacement are not utilized. Therefore, the mode shapes of the NEMS device at resonance were simulated using COMSOL Multiphysics software.

The exact dimensions of the vibrating NEMS device, obtained through SEM imaging, were incorporated to accurately model the 3D geometries. Through the structural mechanics module in COMSOL, the resonance frequencies were determined. By adjusting the residual stress in the silicon nitride (SiN) layer, the simulated resonance frequencies and the experimentally obtained resonance frequencies were matched with high accuracy. Next, a cut-line passing through the center of the beam was utilized to estimate the corresponding mode shapes at both resonance frequencies.

Once the normalized displacement profiles for the first and second modes are plotted, following the derivation outlined earlier in section 2.1.2, the mass and landing position for each of the detected events was determined.

2.6 Results

2.6.1 Purified SARS-CoV-2 Mass Measurements

After successfully optimizing the ESI setup and ensuring effective electrostatic focusing of particles, biological samples were investigated. A PEG-precipitated sample of acute respiratory syndrome coronavirus 2 (SARS-CoV-2) was sprayed and detected by an active NEMS-MS device. The SARS-CoV-2 sample precipitation and purification procedure was discussed earlier in (Figure 2.9).

In this experiment of SARS-CoV-2, a total of 153 landing events were observed within a 14-minute period, primarily corresponding to individual SARS-CoV-2 virion events. The resulting mass spectrum, depicted in Figure 2.17a, was used to fit a non-parametric probability density function (PDF) with a maximum density function value of 454 MDa. To facilitate interpretation and comparison with indirect measurements available in the literature, we converted the mass values to effective diameter values. We assumed a spherical shape for the SARS-CoV-2 virions and used a typical mass density value of 1.4 g/cm^3 based on calculations by [46].

Figure 2.17b displays the inferred diameter histogram based on the measurements in Figure 2.17a. The mass measurement peak value of 454 MDa corresponded to a diameter of 99.7 nm, while the mean diameter of all 153 events was 101.8 nm, with a standard deviation of 13.1 nm. Additionally, Dynamic Light Scattering (DLS) was conducted on the same sample to determine the hydrodynamic diameter of the isolated virus (Figure 2.17b). The DLS characterization revealed a prominent peak at 86 nm, indicating that the majority of the particles in the sample were likely virions. No other significant peaks were observed, confirming the successful of the isolation and precipitation of the sample.

Although this study represented the first-ever direct "mass" measurement of the SARS-CoV-2 virions, previous research has reported "size" measurements of the virions using various microscopy techniques. Previous studies have utilized

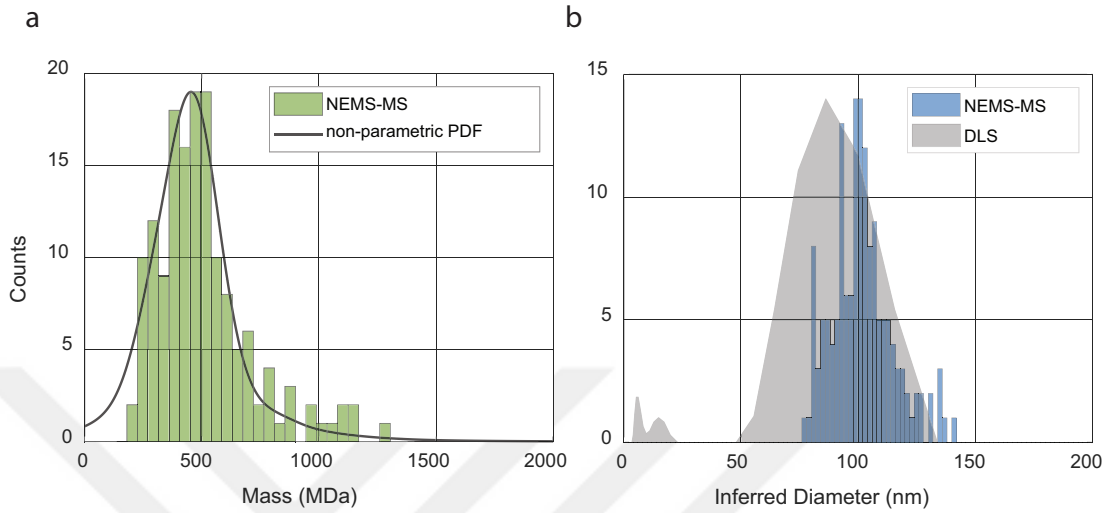

Figure 2.17: Mass and inferred diameter histograms of SARS-CoV-2 virus.

various microscopy techniques, including Scanning Electron Microscopy (SEM) [47, 48], Tunneling Electron Microscopy (TEM) [49, 50, 51], Atomic Force Microscopy (AFM) [52, 53], and Cryo-Electron Microscopy and Tomography (Cryo-EM, Cryo-ET) [54, 55, 56, 57], to estimate the diameter of SARS-CoV-2 virions. These investigations have shown that the average diameter of virion particles typically falls within the range of 80 to 100 nm. However, some studies have reported extreme values as low as 60 nm and as high as 140 nm. Most of these studies reported the core size of the virus excluding the peplomers (*i.e.*, spike proteins projecting from the viral envelope).

NEMS mass measurement however encompassed the entire structure, including the mass of surface proteins. Hence, it was expected that the size determined by NEMS-MS would be slightly larger. Table 2.3 provides a quantitative comparison between the diameter measurements of SARS-CoV-2 obtained through imaging techniques described in the literature and the inferred diameter derived from NEMS-MS. The close similarity in values demonstrates that the NEMS-MS system, operating under room temperature and atmospheric pressure conditions, is an excellent tool for virus detection and characterization.

Table 2.3: Measured SARS-CoV-2 diameters obtained through various techniques as reported in the literature.

Ref.	Method	Virion diameter (nm)	Notes
[49]	TEM	60-140	(+9-12) nm spikes
[54]	Cryo-ET	89.8	SD = 13.7 nm
[47]	SEM	65-80	-
[50]	TEM	97	Core diameter without spikes
[55]	Cryo-EM	91	Core diameter without spikes
[48]	SEM	80-120	(+9-13) nm spikes
[51]	TEM	90.33 and 71.02	Core diameter assembled from HEK-293T cells and Vero E6 cells respectively
[52]	AFM	83	Height of the center of the virus, SD = 7 nm
[56]	Cryo-EM	85.9	Medium axis of the lipid bilayer, SD = 9.4 nm
[57]	Cryo-ET	90	Core diameter estimated from slices of tomography
[53]	AFM	89	Height of the center of the virus, SD = 19 nm
This work [4]	NEMS MS	101.8	Inferred diameter from the total mass (including surface proteins), SD = 13.1 nm

2.6.2 SARS-CoV-2 Mass Measurements (Purified *vs.* Lysate)

To evaluate the performance of the NEMS-MS technique on a complex biological solution like the clarified cell lysate, we conducted further NEMS-MS experiments after removing the PEG precipitation from the purification protocol. The cell lysate was subjected to dialysis to eliminate nonvolatile salts, ensuring compatibility with Electrospray Ionization. DLS analysis of the lysate sample revealed a peak around 115 nm, accompanied by a much larger peak spanning between 200 and 1200 nm. This larger peak was likely caused by interference from cellular debris present in the sample. Spraying such a solution, which contained relatively massive particulates ($>$ 100 GDa), could potentially damage the suspended NEMS beam. In several experimental runs with the lysate sample, the NEMS device stopped responding due to damage caused by the landing of these comparatively large particles.

To address this issue, the cell lysate was centrifuged for a longer duration and at a higher speed than previously described. This adjustment aimed to remove the majority of the larger cell debris. In a subsequent trial, we registered a total of 101 events after approximately 18 minutes of spraying without any NEMS damage. Most of these events fell within the mass range determined from the isolated SARS-CoV-2 sample, as depicted in Figure 2.18. However, in comparison to the isolated virus sample, additional particulates, particularly at higher mass values, were detected, likely originating from cellular debris. Nonetheless, above this background, a distinct population emerged at the expected location for SARS-CoV-2, with the major peak almost overlapping with the spectrum peak of the isolated virus (469 *vs.* 454 MDa, respectively). Table 2.6.2 presents the key results for mass measurements of SARS-CoV-2 from both the PEG-precipitated sample and the purified lysate. Note that in the lysate sample, the events with masses larger than 1 GDa were considered as cellular debris and were not considered in the calculations.

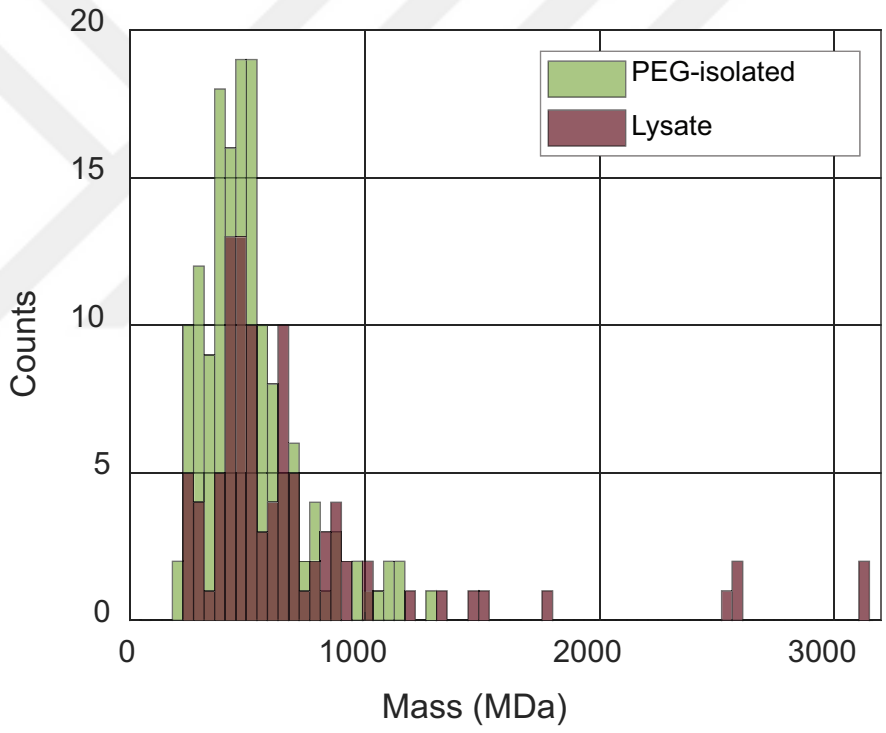

Figure 2.18: Mass spectrum of SARS-CoV-2 virus obtained from both PEG-precipitated and lysate samples.

Table 2.4: Statistical measures of SARS-CoV-2 Experiments (PEG-precipitated *vs.* Lysate).

Measure	PEG-precipitated SARS-CoV-2 sample	SARS-CoV-2 lysate sample
Most probable mass from non-parametric PDF (MDa)	469	454
Mean mass (MDa)	507	539
Median mass (MDa)	466	499
Standard deviation (MDa)	208	172
NEMS Mass resolution (MDa)	45	19

2.6.3 SARS-CoV-2 *vs.* BoHV-1 Mass Spectrum

In addition to SARS-CoV-2 virus, NEMS-MS experiment with an inactivated bovine herpesvirus type 1 (BoHV-1) sample was conducted. In this experiment, the sample preparation protocol was identical to the PEG-precipitated SARS-CoV-2 sample as depicted in 2.9. This experiment served as both a control experiment and a demonstration of the system's ability to detect virions from a different mammalian virus family. BoHV-1 exhibits a more intricate structure compared to SARS-CoV-2 and possesses a larger mean diameter. Furthermore, electron microscopy has shown that the virion of BoHV-1 can incorporate multiple nucleocapsids, resulting in a broader size distribution [58]. Additionally, different studies have shown different diameter of the enveloped virions ranging from 95 nm in [58] up to 166 nm in [59].

The NEMS-MS experiment using the BoHV-1 virus sample produced 83 landing events in total. Among these, 31 events exhibited mass values exceeding 4.2 GDa. The outcomes of the experiment were consistent with the expected size distribution of BoHV-1, as depicted in Figure 2.19. Notably, distinct peaks observed in the SARS-CoV-2 analysis, corresponding to the anticipated mass and size values, were absent in the BoHV-1 analysis. This finding highlights the specificity of NEMS-MS when analyzing different viral samples.

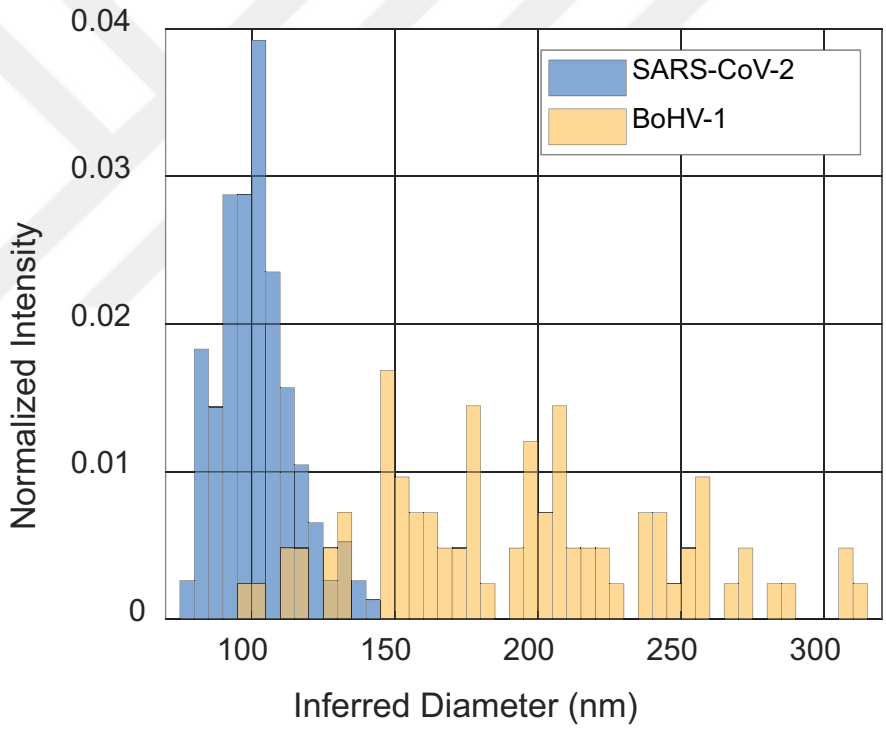

Figure 2.19: Inferred diameter histograms of SARS-CoV-2 and BoHV-1 viruses.

Chapter 3

Dissipative Mode Shapes in Atmospheric NEMS-MS

The utilization of NEMS-MS under atmospheric conditions has significantly advanced the progress of this technique towards commercialization. However, operating within a dissipative environment introduces specific challenges, one of which is Mode Shape Attenuation. This phenomenon refers to the deviation of the displacement profiles of the NEMS from the expected ideal mode shapes. Various factors, including the viscous damping of air and the actuation-readout scheme, contribute to the occurrence of mode shape attenuation. The purpose of this chapter is to address this issue comprehensively. To begin, the Introduction section provides an explanation of mode shape attenuation, its origins, and a brief overview of its impact on mass measurement. Subsequently, two mathematical models are proposed to estimate the displacement profiles when dissipation is present. Additionally, a dedicated section is devoted to a detailed analysis of the expected mass uncertainty resulting from mode shape attenuation. Finally, a series of experiments is presented to effectively illustrate the effect of mode shape attenuation.

3.1 Introduction

Nanoelectromechanical Systems-based Mass Spectrometry (NEMS-MS) is an emerging technique that performs mass measurement of particles weighing in the MDa to GDa range which is away from the working range of conventional mass spectrometry techniques. As demonstrated in Chapter 2, this technique can be operated effectively under atmospheric conditions offering sufficient resolutions. Recent advancements in Atmospheric Pressure NEMS-MS have addressed various limitations of the established NEMS-MS, including the elimination of bulky vacuum setups, enhanced throughput, and improved capture efficiency [4]. These developments have propelled the technique closer to practical real-world applications and commercial viability.

However, when NEMS devices are operated at atmospheric pressure, a reduction in the Quality factor (Q) is expected compared to vacuum conditions due to thermoelastic damping [60, 61, 62, 63]. [60] extensively discusses the fluid-induced influence on the vibrational properties of a cantilever beam. A comprehensive theoretical analysis is presented, focusing on the frequency response of the beam when submerged in a viscous fluid and subjected to an arbitrary driving force. Verbridge et al. investigated the impact of dissipative media on resonating Silicon Nitride (SiN) doubly-clamped beams and measured the Quality factor of SiN doubly-clamped beams resonating in air, water, and PBS (phosphate-buffered saline) [61]. Yasumura et al. [62] explored the loss mechanisms in SiN cantilever beams and established a relationship between the Quality factor and the geometry of SiN beams. Their findings indicated that for submicron-thick cantilevers, Q decreases with decreasing thickness, suggesting the presence of surface loss mechanisms. Additionally, it was observed that when operating at atmospheric pressure, below 1 mtorr, the Quality factor of SiN is primarily limited by pressure rather than temperature. The decrease in the Quality factor compromises the sensitivity of NEMS resonators, thereby limiting their mass resolution when utilized as mass sensors.

In resonant NEMS mass measurement, the determination of mass and position of particles landing on the NEMS beam relies on the foreknowledge of the normalized displacement profiles at resonance (referred to as *Mode shape*) of the NEMS device used. These mode shapes are formulated using the elasticity wave equation, which, when solved, provides undamped eigenfunctions with well-known standing wave mode shapes. All NEMS mass spectrometry studies in the literature, including the initial report on Atmospheric NEMS-MS [4], utilize the ideal mode shapes for reverse-calculating the mass and position of the landing particles. However, the actual displacement profiles of NEMS structures deviate from these ideal mode shape solutions due to various factors such as non-ideal nanofabrication, stress distribution on the device, and random accumulation of adsorbents on the surface. Furthermore, a recent investigation into the oscillatory dynamics of the NEMS devices used in this study revealed that the displacement profiles are attenuated when the NEMS operates in a dissipative environment [3]. This phenomena is referred to as "Mode Shape Attenuation" throughout this chapter.

Figure 3.1a-c, adapted from [3], illustrates the discrepancy between the measured displacement of the NEMS along the beam (represented by the dots) and the ideal mode shape of the NEMS (depicted by the shaded area). In the case of doubly-clamped beams utilized here, the ideal mode shapes are given by $\left|\sin\left(\frac{n\pi}{L}x\right)\right|$ where x is the position along the beam, L is beam length and $n = 1, 2, 3$ for the first, second and third mode respectively.

Viscous air damping leads to a loss of symmetry about the center of the beam in the displacement profile away from the driving electrode. For comparison, Figure 3.1d-f presents measurements of the NEMS displacement under low dissipation conditions (*i.e.*, in a vacuum). It is noteworthy how closely the measurements performed in vacuum align with the expected mode shapes. The actuation of the NEMS is achieved by thermo-elastically, specifically through the electrode positioned on the left side of the beam (at $x = 0$ in Figure 3.1). On the other hand, the electrode on the right (at $x = L$) is utilized for read-out purposes. This convention is consistently maintained throughout this chapter.

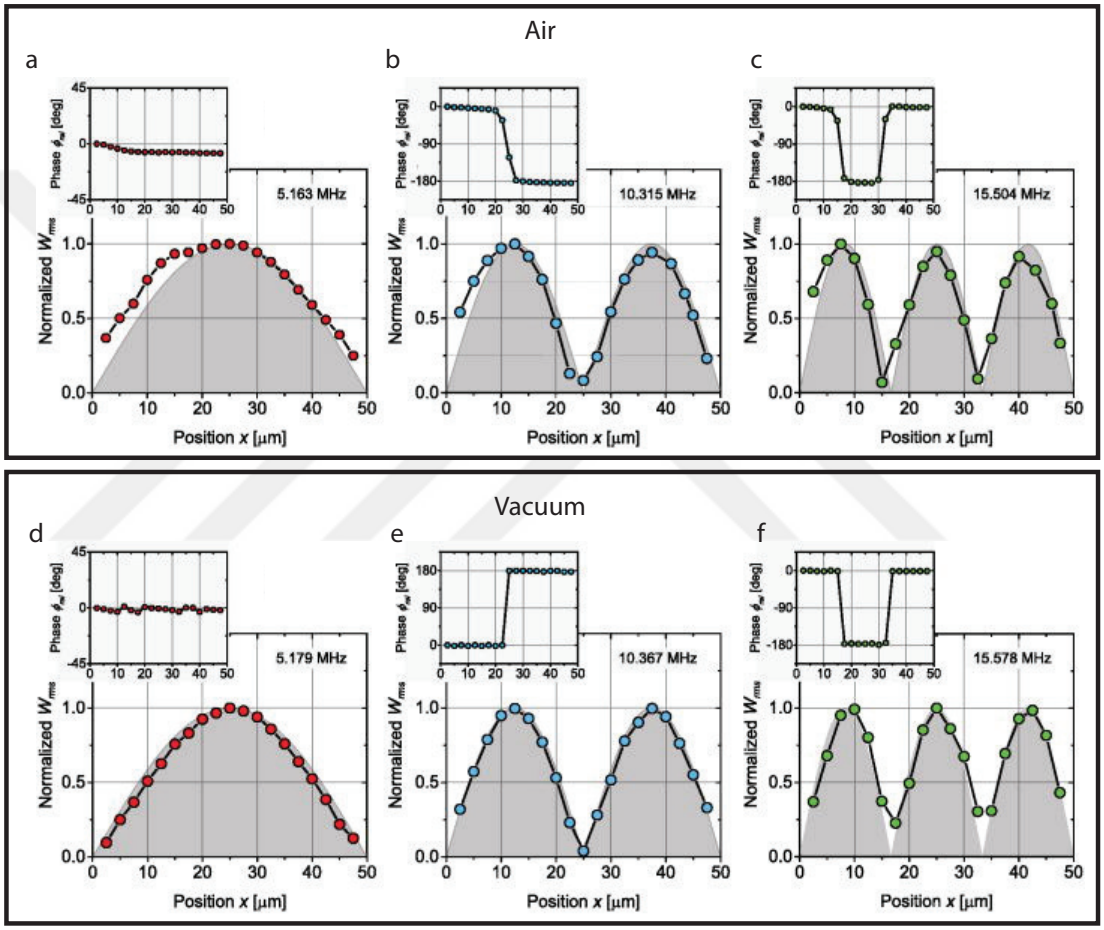

Figure 3.1: NEMS displacement measurements in air and vacuum. For NEMS operating in air, the quality factors for the first, second, and third mode shapes are 32, 54, and 73, respectively. Conversely, in a vacuum, the quality factors shift to 23600, 22800, and 20300 for the first, second, and third mode shapes, respectively. Figures adapted from [3, C. Ti et al.; Dynamics of NEMS resonators across dissipation limits. Appl. Phys. Lett. 11 July 2022; 121 (2): 023506. https://doi.org/10.1063/5.0100318] with permission from AIP Publishing, License Number: 5610710652347.

3.2 Mode Shape Attenuation and Atmospheric NEMS-MS

This section delves into the examination of the effect of the attenuation of the displacement profile on mass sensing. More specifically, how particles landing at different sides of the NEMS device can generate different responses. In this analysis, the displacement amplitude is normalized such that the maximum is unity whereas the position on the NEMS beam is normalized such that 0 corresponds to the anchor point where the "drive electrode" is situated and 1 corresponds to the "read-out electrode" side.

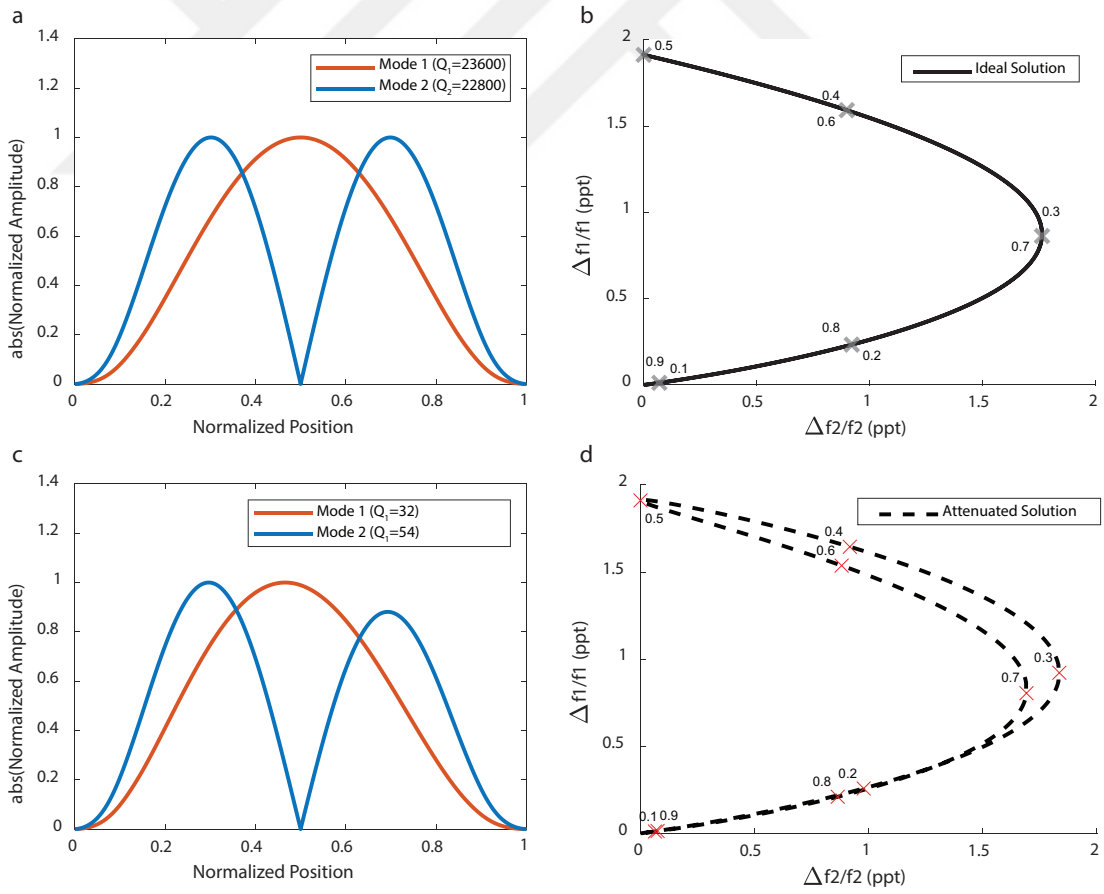

Figure 3.2: The effect of the mode shape attenuation on Two-mode theory.

Figure 3.2 demonstrates the impact of mode shape attenuation on the determination of mass and landing position of analytes, employing the quality factors

reported in [3]. In vacuum-operating NEMS, the first and second mode shapes have record quality factors of 23600 and 22800, respectively. The utilization of high quality factor mode shapes preserves symmetry (as depicted in Figure 3.2a). This symmetry leads to a solitary solution in the δf_1 *vs.* δf_2 plot for calculating analyte mass and landing position. Figure 3.2b illustrates the solution for frequency shifts resulting from a representative mass value of 1.5 particles per thousand (ppt) of the beam's total mass, utilizing the ideal displacement profile featured in panel (a). The cross markers correspond to the solutions for the same mass landing at 0.1, 0.2, ... , 0.9 along the beam. As the displacement profiles are symmetric about the center of the resonating beam, solving for half of the beam is adequate to ascertain both mass and landing position. Notably, a particle landing at position x yields identical frequency shifts to one landing at $1 - x$.

However, in situations where the NEMS operates in an air environment with compromised resonance quality factors, the displacement profiles experience attenuation, resulting in the breakdown of symmetry across the beam's displacement profile. This is illustrated in Figure 3.2c with first and second mode shape quality factors of 32 and 54, respectively as reported in [3]. Consequently, the singular solution observed in the frequency shifts plane (Figure 3.2b) bifurcates into two distinct solutions contingent on the side of the beam where the particle lands, as illustrated in Figure 3.2d. Within the δf_1 *vs.* δf_2 plot, the outer curve represents the particles landing closer to the driving electrode side of the NEMS beam whereas the inner curve represents the particles landing closer to the read-out side.

Hence, an enhanced displacement profile model is essential in atmospheric NEMS-MS to enhance the resulting mass spectra, accounting for resonance quality factors. It's important to highlight that the attenuation depicted in Figure 3.2c is derived from the quality factors noted in [3], providing a visual demonstration of how mode shape attenuation introduces an additional unknown in the two-mode theory. Section 3.5 is entirely dedicated to estimating the mass measurement uncertainty arising from this phenomenon.

3.3 Mathematical Modelling Based on Wave Propagation

Estimation of the displacement profile function is an important step for NEMS mass spectrometry. In this section, a mathematical model that accounts for the displacement profile attenuation is derived. The model assumes that the bending term is small and the beam behave as beam under tension.

The generalized n^{th} mode shape in an ideal setting (ϕ_n) can be approximated as follows:

$$\phi_n(x) = \sin\left(\frac{n\pi x}{L}\right) \tag{3.1}$$

Where x is the distance along the beam, n is the mode number and L is the beam length. In a lossless setting, this ideal standing wave can be viewed as emerging from a traveling wave perfectly reflecting back and forth at the clamping points. However, when the beam is driven in a lossy environment, viscous damping is expected to occur [3]. For this reason, the attenuated displacement profile or the damped mode shape (Φ) is modeled as follows:

$$\Phi_0(x) = \phi(x) \cdot e^{-\gamma x} \tag{3.2}$$

Where $\gamma > 0$ is the decay coefficient. Note that the damped displacement profile is denoted with a subscript (0) to indicate that it is the incident wave. When the wave reaches the opposite side (*i.e.*, the clamp with the read-out electrode), the mode shape will be attenuated by $e^{-\gamma L}$. Now, and depending on the boundary condition at the clamp, the first reflection (Φ_1) will be equal to:

$$\Phi_1(x) = \Gamma \cdot \phi(x) \cdot e^{-2\gamma L} \cdot e^{\gamma x} \tag{3.3}$$

Where Γ is the reflection coefficient and is set between 0 for perfectly matched system (*i.e.*, no loss) and -1 for highly mismatched system (*i.e.*, high loss). Note that the direction of the decay function is flipped in the odd reflection (*i.e.*, $e^{-\gamma(x-L)}$ instead of $e^{-\gamma x}$). Similarly, the subsequent reflections are calculated:

$$\Phi_2(x) = \Gamma^2 \cdot \phi(x) \cdot e^{-3\gamma L} \cdot e^{-\gamma x} \tag{3.4}$$

$$\Phi_3(x) = \Gamma^3 \cdot \phi(x) \cdot e^{-4\gamma L} \cdot e^{-\gamma x} \tag{3.5}$$

$$\Phi_4(x) = \Gamma^4 \cdot \phi(x) \cdot e^{-5\gamma L} \cdot e^{-\gamma x} \tag{3.6}$$

$$\vdots$$

Summing the even numbered reflections:

$$\begin{aligned} \Phi_{\text{even}}(x) &= \Phi_0(x) + \Phi_2(x) + \Phi_4(x) + \cdots \\ \Phi_{\text{even}}(x) &= \phi(x)e^{-\gamma x}\left(1 + \Gamma^2 e^{-3\gamma L} + \Gamma^4 e^{-5\gamma L} + \cdots\right) \end{aligned} \tag{3.7}$$

Using the sum of infinite geometric series, the sum of even mode shapes can be written as:

$$\Phi_{even}(x) = \phi(x)e^{-\gamma x}\left(1 + \frac{\Gamma^2 e^{-3\gamma L}}{1 - \Gamma^2 e^{-2\gamma L}}\right) \tag{3.8}$$

Similarly, the odd numbered reflections can be summed as follows:

$$\begin{aligned} \Phi_{odd}(x) &= \Phi_1(x) + \Phi_3(x) + \Phi_5(x) + \cdots \\ \Phi_{odd}(x) &= \phi(x)e^{\gamma x}\left(\Gamma e^{-2\gamma L} + \Gamma^3 e^{-4\gamma L} + \cdots\right) \\ \Phi_{odd}(x) &= \phi(x)e^{\gamma x}\left(\frac{\Gamma e^{-2\gamma L}}{1 - \Gamma^2 e^{-2\gamma L}}\right) \end{aligned} \tag{3.9}$$

Applying superposition, the final solution of the attenuated mode shape can be written as follows:

$$\begin{aligned} \Phi(x) &= \Phi_{\text{even}}(x) + \Phi_{odd}(x) \\ \Phi(x) &= \frac{\phi(x)}{1 - \Gamma^2 e^{-2\gamma L}}\left(Xe^{-\gamma x} + Ye^{\gamma x}\right) \end{aligned} \tag{3.10}$$

where:

$$\begin{aligned} X &= 1 - \Gamma^2 e^{-2\gamma L}\left(1 - e^{-\gamma L}\right) \\ Y &= \Gamma e^{-2\gamma L} \end{aligned} \tag{3.11}$$

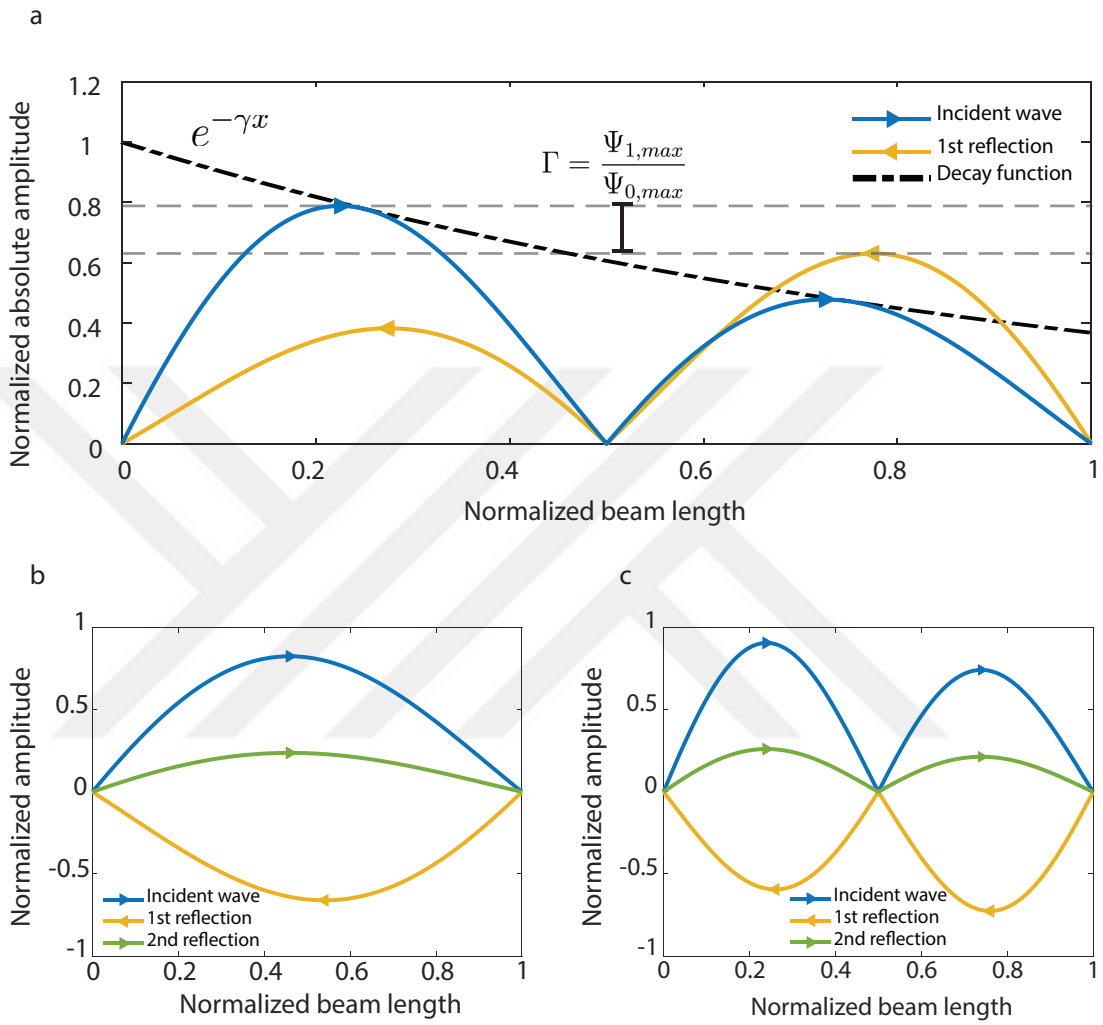

Figure 3.3: Mathematical model of mode shape attenuation based on wave propagation.

Figure 3.3 depicts the mathematical model based on wave propagation, proposed to describe the attenuation of mode shapes. In Figure 3.3a, the second mode shape with an attenuation function is shown to decay by $e^{(-\gamma x)}$, where $(\gamma > 0)$ represents the decay coefficient, and x is the normalized distance from the drive side.

The reflection coefficient (Γ) governs the proportion of the reflected wave in relation to the incident wave, and it is determined by the losses at the clamping point. Figure 3.3b and c demonstrate the progression of the waves in the first and second out-of-plane modes respectively based on this model. This model employs

two physically meaningful coefficients, namely the decay coefficient (γ) and the reflection coefficient (Γ).

The proposed mathematical model offers the advantage of requiring fewer free parameters in comparison to the time-dependent solution derived in [3], which is based on the string equation with uniform viscous damping. The time-dependent solution is expressed as follows:

$$w(x,t) = \Re\left\{Ae^{-k_I x}e^{i(k_R x-\omega t)} + Be^{k_I x}e^{-i(k_R x+\omega t)}\right\} \tag{3.12}$$

Here the parameters A and B represent the complex amplitudes of the right- and left-propagating waves, respectively. However, these parameters lack a direct physical correlation and are typically determined through fitting. Moreover, the values of $k_R = \mathfrak{R}\{k\}$ and $k_I = \mathfrak{I}\{k\}$ depend on other parameters that are not readily measurable experimentally, defined as:

$$k = k_R + ik_I = \frac{\omega}{c}\left(1 + i\frac{\gamma}{\mu\omega}\right)^{1/2} \tag{3.13}$$

where $c = \sqrt{\frac{\tau}{\mu}}$ represents the speed of flexural waves in the beam, necessitating the measurement of the tension in the beam (τ), while γ denotes the damping per unit length and μ is the mass per unit length of the NEMS beam.

On the other hand, the proposed mathematical model presents a streamlined approach, involving fewer parameters, to effectively model the dissipation in the displacement profiles caused by viscous damping.

3.4 Experimental Results *vs.* Proposed Model

To assess the performance of the developed mathematical model, experimental measurements conducted by Ti et al. [3] were used to fit the proposed model. The fitting process was carried out for both vacuum and air conditions.

In order to determine the ideal displacement profile (*i.e.*, the mode shape) applicable to the model, the 50 µm device utilized in the measurements was simulated in COMSOL Multiphysics.

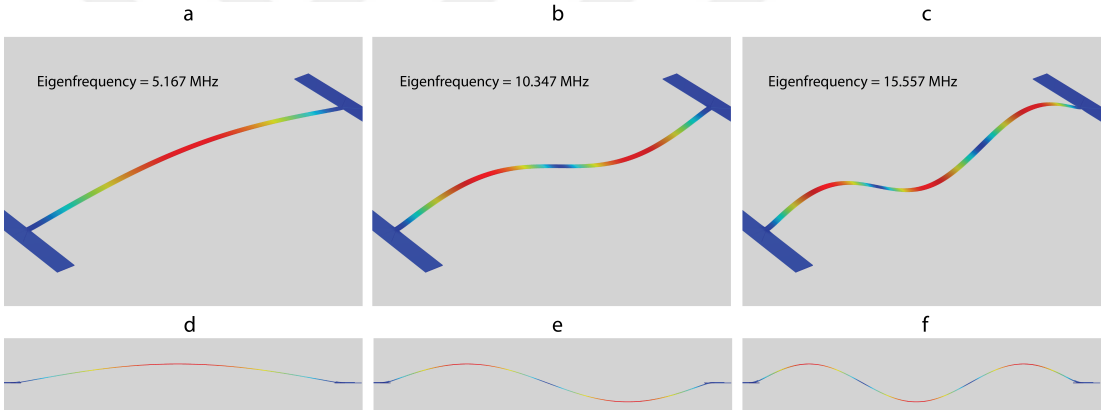

Figure 3.4: COMSOL simulated mode shapes of the device utilized in (Ti et al., 2022). Panels (a-c) display the first three mode shapes in isometric view and panels (d-f) depict the out-of-plane view of the corresponding modes.

The experimentally measured resonance frequencies for the first, second, and third out-of-plane modes were 5.179 MHz, 10.367 MHz, and 15.578 MHz, respectively [3]. In the COMSOL simulation, the residual stress in the Silicon Nitride (SiN) layer was adjusted until the experimentally obtained and simulated resonance frequencies matched within 0.15% (see Figure 3.4). The identified residual stress was found to be 813 MPa.

In each mode, the decay coefficient (γ), representing the parameter for viscous damping, was assumed to be inversely proportional to the reported Quality factor (Q), such that:

$$\gamma_n = \frac{1}{Q_n}$$

The Quality factors for the vacuum case were reported as 23600, 22800, and 20300 for the first, second, and third modes, respectively [3], leading to small decay coefficients in the order of 10^{-5}. For the air case, the reported Quality factors were 32, 54, and 73 for the first, second, and third modes [3], resulting in decay coefficients approximately three orders of magnitude higher than the vacuum case (10^{-2}).

As the reflection coefficient Γ is attributed to the loss at the boundary condition, rather than the viscous damping, it was determined to have a consistent value of -0.7 for both air and vacuum conditions. Table 3.1 summarizes the parameters used for all three modes in both air and vacuum

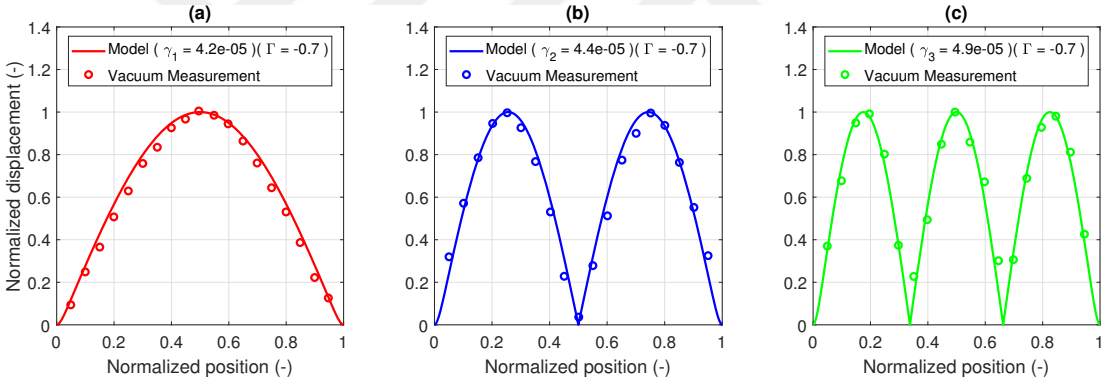

Figure 3.5: Comparison between the mathematical model and experimental results adapted from [3] concerning vacuum condition in the first three modes.

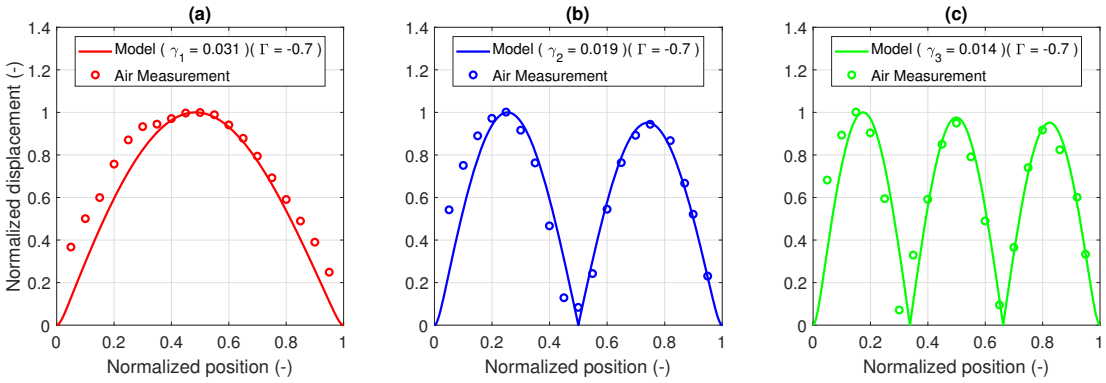

Figure 3.6: Comparison between the mathematical model and experimental results adapted from [3] concerning air condition in the first three modes.

The fitting for the vacuum case using the model parameters calculated is performed and presented in Figure 3.5, and it demonstrate excellent agreement with

the experimental result [3].

In the air case, the fitting result using the parameters as described above is shown in Figure 3.6. While the model effectively captures the decaying nature of the mode shape, it exhibits symmetry near the anchors which is not the case in the experimental results. To enhance the fit to the experimental results under air conditions, a normalization step was incorporated. An effective length (L_{eff}) in each mode was suggested to account for the asymmetry near the boundary.

The effective length (L_{eff}) was computed by dividing the length of the NEMS beam (*i.e.*, 50 µm) by the integration of the normalized ideal mode shape obtained from COMSOL, as follows:

$$L_{eff}^{(n)} = \frac{2L}{\int_{a=0}^{a=1} \phi_n(a)^2 da} \tag{3.14}$$

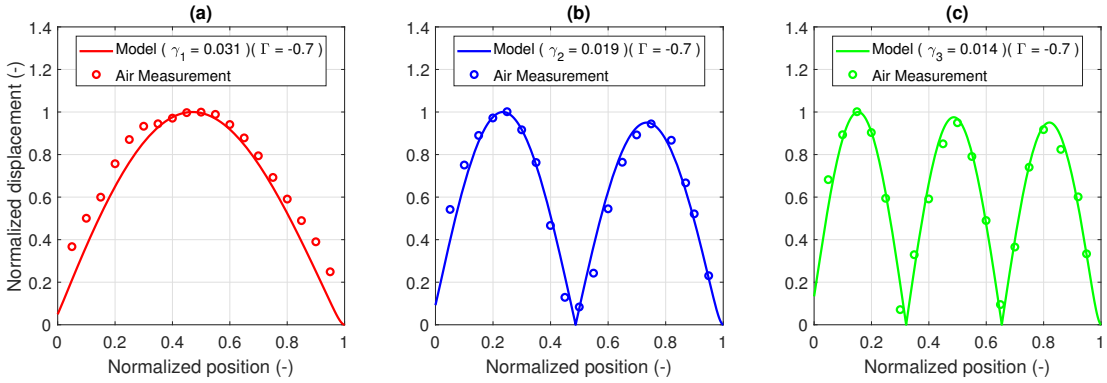

Figure 3.7: Comparison between the mathematical model and experimental results adapted from [3] concerning air condition in the first three modes with boundary condition modified.

Following this normalization step, the experimental and modeled results exhibited improved fitting in air (Figure 3.7). Notably, the additional length induced by the effective length measurement was added at the actuation electrode side (*i.e.*, at $x = 0$).

Table 3.1: Air and vacuum fitting parameters for the first 3 out-of-plane modes.

Environment	Parameter	Mode 1	Mode 2	Mode 3
Vacuum	Quality factor (Q) [3]	23600	22800	20300
	Decay coefficient (γ)	4.24×10^{-5}	4.39×10^{-5}	4.93×10^{-5}
	Reflection coefficient (Γ)	-0.7	-0.7	-0.7
	Effective length (L_{eff})	50 µm	50 µm	50 µm
Air	Quality factor (Q) [3]	32	54	73
	Decay coefficient (γ)	0.0312	0.0185	0.0137
	Reflection coefficient (Γ)	-0.7	-0.7	-0.7
	Effective length (L_{eff})	51.31 µm	51.30 µm	51.28 µm

3.5 Dissipation and Mass Uncertainty

To comprehend how uncertainty in mass measurement can arise from attenuation in the displacement profile, it is necessary to first grasp how the measurement of changes in the first two modes can determine the mass and landing position of the analyte. A detailed explanation of this concept can be found in Chapter 2 (section 2.1.2). For a complete derivation of the two-mode theory for solving the mass and landing position of the analytes, the reader is referred to [23].

The key takeaway is that if we assume the displacement profile to be symmetric (Figure 3.2a), meaning it matches the undamped mode shape, then the two-mode theory alone is adequate for resolving the mass and landing position of the analytes. In this scenario, the landing position will be determined relative to half the length of the beam. In other words, a particle with a specific mass value landing at a certain distance from either electrode will induce the same frequency shifts in both modes (Figure 3.2b). For instance, a particle landing at $x = 0.3$ normalized distance from the actuation electrode will ideally produce the same frequency shift in all modes as if it landed at $x = 0.7$ from the same electrode.

However, when attenuation is present, as is the case in dissipative environments such as air [3], the symmetry of the displacement profile about the center of the beam is lost. This introduces an additional variable to the two-mode theory, such that a particle landing at x or $1 - x$ will cause non-identical frequency shifts in all modes (Figure 3.2c-d).

In this section, the uncertainty in mass measurement due to attenuation in the displacement profile is estimated in a systematic way. First recall from chapter 2 that the frequency shifts in the first and second modes (δf_1 and δf_2 respectively) due to a particle with mass (Δm) landing on the doubly-clamped beam with total mass (M) is calculated as follows:

$$\delta f_1 = \frac{\Delta f_1}{f_1} = \frac{\Delta m}{M\alpha_1}\phi_1^2(x) \tag{3.15}$$

$$\delta f_2 = \frac{\Delta f_2}{f_2} = \frac{\Delta m}{M\alpha_2}\phi_2^2(x) \tag{3.16}$$

Where $\phi_1(x)$ and $\phi_2(x)$ are the mode shapes which were derived earlier for the air and vacuum conditions, δf_1, δf_2 are the change in frequency in the first and second modes respectively and α_1, α_2 are the integration of the squared of the mode shape as follows:

$$\alpha_n = \int_{a=0}^{a=1} \phi_n(a)^2 da \tag{3.17}$$

For simplicity, define $\theta_1(x)$ and $\theta_2(x)$ as the squared of the mode shapes normalized with the integral of the mode shape as follows:

$$\theta_1(x) = \phi_1^2(x)/\alpha_1 \tag{3.18}$$

$$\theta_2(x) = \phi_2^2(x)/\alpha_2 \tag{3.19}$$

Denoting $(\frac{\Delta m}{M})$ as δm, equations 3.15 and 3.16 can be re-written as follows:

$$\delta f_1 = \delta m \theta_1 \tag{3.20}$$

$$\delta f_2 = \delta m \theta_2 \tag{3.21}$$

Now we define a function $g(x)$ as follows:

$$g(x) = \frac{\delta f_2}{\delta f_1} \tag{3.22}$$

which when evaluated at a specific position (x_{val}) is denoted (η) as follows:

$$\eta = \frac{\delta f_2}{\delta f_1} \tag{3.23}$$

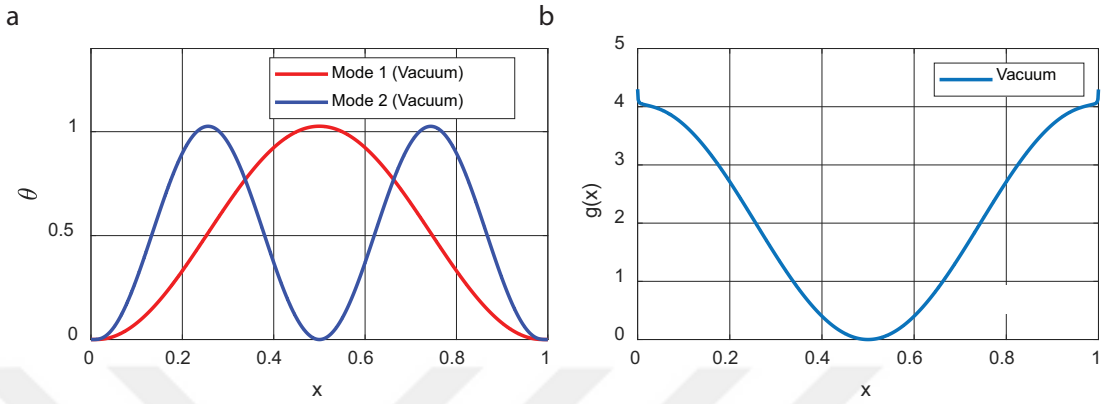

Figure 3.8: Function $g(x)$ for a NEMS operating at vacuum condition ($Q_1 = 23600$ and $Q_2 = 22800$).

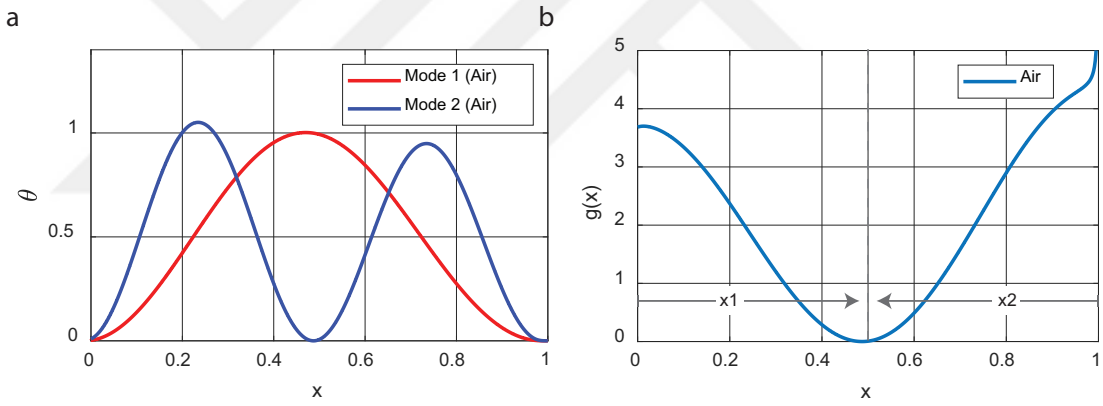

Figure 3.9: Function $g(x)$ for a NEMS operating at atmospheric condition ($Q_1 = 32$ and $Q_2 = 54$).

Now we define functions $g_1(x)$ and $g_2(x)$ in which the position is measured from the drive electrode ($x = 0$) and read-out electrode ($x = 1$) respectively (Figure 3.9b). When NEMS is operated in vacuum (*i.e.*, $\alpha_1 = \alpha_2 = 0$), the mode shapes preserve the symmetry about the center of the beam and therefore the function $g(x)$ is symmetric. This causes the solutions $g_1(x)$ and $g_2(x)$ to be identical (Figure 3.8). However when operated in a dissipative media, then $\alpha_1 \neq \alpha_2 \neq 0$ and the resulting functions $g_1(x)$ and $g_2(x)$ become non-identical (Figure 3.9).

Rearrange equation (3.20) as follows:

$$\delta m = \frac{\delta f_1}{\theta_1(x)} \tag{3.24}$$

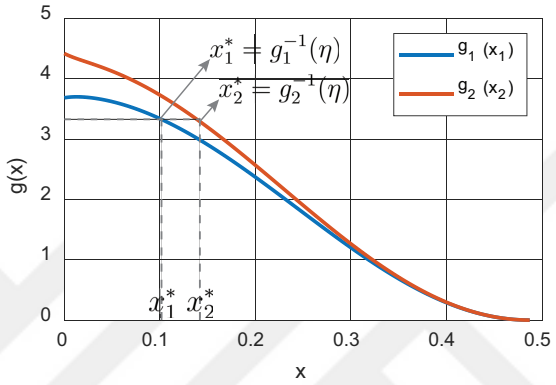

Figure 3.10: The emergence of two distinct solutions for the landing position due to dissipation. The two curves would overlap if there were no dissipation.

However and due to the emergence of two different solutions $g_1(x)$ and $g_2(x)$, there will be two possibilities for a single value of position (x_{val}) namely $x_1^* =_1^{-1} (\eta)$ and $x_2^* = g_2^{-1}(\eta)$ as demonstrated in Figure 3.10.

Now we substitute both possibilities in equation 3.24 and using equation 3.23:

$$\left(\frac{\Delta m}{M}\right)^*_1 = \frac{\Delta f_1}{f_1 \theta_1 \left(g_1^{-1}(\eta)\right)} \tag{3.25}$$

$$\left(\frac{\Delta m}{M}\right)^*_2 = \frac{\Delta f_1}{f_1 \theta_1 \left(g_2^{-1}(\eta)\right)} \tag{3.26}$$

Using the notation $\frac{\Delta m}{M} = \delta m$, equations 3.25 and 3.26 can be written as:

$$\delta m_1^* = \frac{\Delta f_1}{f_1 \theta_1 \left(g_1^{-1}(\eta)\right)} \tag{3.27}$$

$$\delta m_2^* = \frac{\Delta f_1}{f_1 \theta_1 \left(g_2^{-1}(\eta)\right)} \tag{3.28}$$

Now the uncertainty in mass measurement can be quantified as follows:

$$\frac{\delta m^{\text{uncert.}}}{\delta m^{\text{avg.}}} = \frac{|\delta m_1^* - \delta m_2^*|}{\left(\frac{\delta m_1^* + \delta m_2^*}{2}\right)} \tag{3.29}$$

Substituting 3.27 and 3.28 in 3.29 yields:

$$\frac{\delta m^{\text{uncert.}}}{\delta m^{\text{avg.}}} = \frac{2\left|\left(\frac{g_2^{-1}(\eta)}{g_1^{-1}(\eta)g_2^{-1}(\eta)} - \frac{g_1^{-1}(\eta)}{g_1^{-1}(\eta)g_2^{-1}(\eta)}\right)\right|}{\left(\frac{g_2^{-1}(\eta)}{g_1^{-1}(\eta)g_2^{-1}(\eta)} + \frac{g_1^{-1}(\eta)}{g_1^{-1}(\eta)g_2^{-1}(\eta)}\right)} = \frac{2\left|g_2^{-1}(\eta) - g_1^{-1}(\eta)\right|}{g_2^{-1}(\eta) + g_1^{-1}(\eta)} \tag{3.30}$$

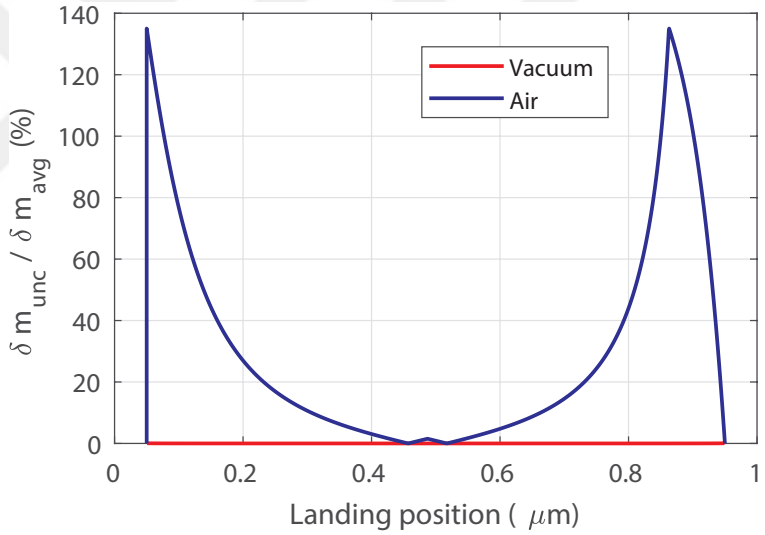

Figure 3.11: The uncertainty in mass measurement arising from the ambiguity in the landing side. In vacuum conditions, the quality factors were $Q_1 = 23600$ and $Q_2 = 22800$ for the first and second modes, respectively, while in an air environment, they were $Q_1 = 32$ and $Q_2 = 54$.

Figure 3.11 illustrates the calculated uncertainty in mass for all possible positions in both air and vacuum conditions. As expected, when operated in a vacuum, the uncertainty remains nearly 0% across the entire length of the beam. However, NEMS-MS is performed in air, the uncertainty takes on a bathtub-like shape, with higher uncertainty observed for particles landing closer to the anchor points.

Approximately 25% of the landing positions (*i.e.*, for $0 < x < 0.1$ and $0.85 < x < 1$) exhibit uncertainty levels surpassing 100%. In these landing positions,

the uncertainty in mass measurement is primarily influenced by the attenuation effect. Conversely, when particles land closer to the center of the beam, the uncertainty drastically decreases, and in this region, the uncertainty in mass is primarily limited by the mass resolution (arising from the frequency stability). This analysis underscores the significant impact of mode shape attenuation in air on mass measurement accuracy.

3.6 Mode Shape Attenuation Effect: Experimental Results

The objective of this analysis is to demonstrate that the experimental results obtained from NEMS-MS (Nanoelectromechanical Systems Mass Spectrometry) tend to deviate from ideal solutions when operated in air. For this purpose, a NEMS-MS experiment is conducted using 200 nm fluorescent Polystyrene nanoparticles (f-PSNP) in an air environment. The NEMS device is operated, and after capturing a single landing event, the NEMS is immediately halted. The landing position and side are estimated using a fluorescent microscope.

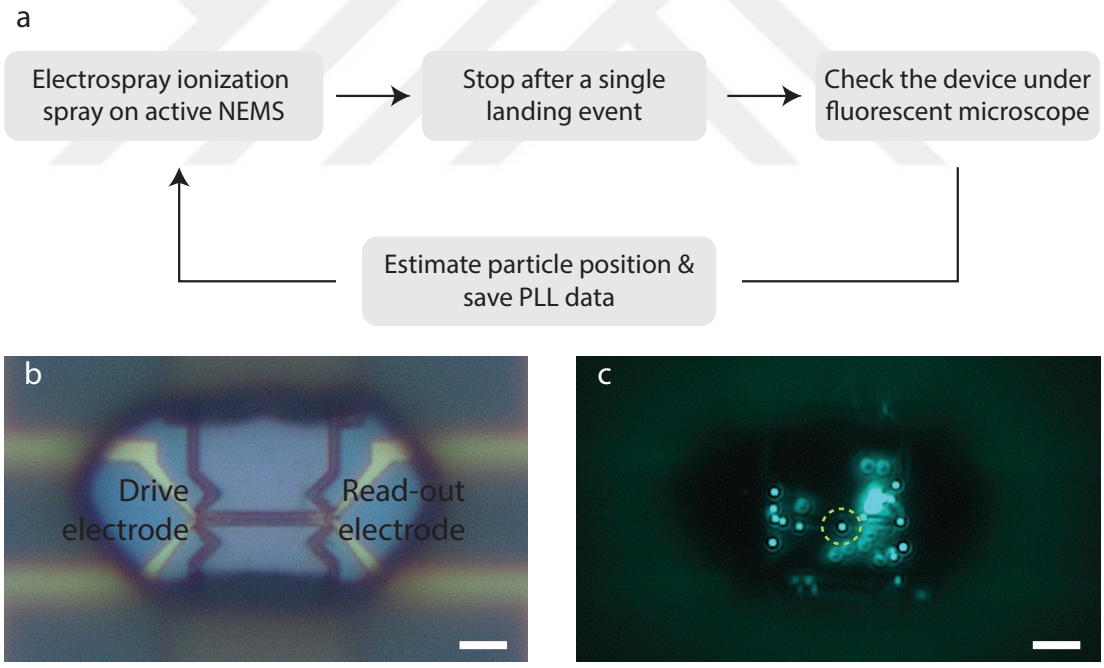

Figure 3.12: Experimental demonstration of mode shape attenuation effect. Workflow is depicted in panel (a). Panels (b) and (c) display bright field and fluorescent microscope images, respectively, captured after a single landing event. Scale bar: 5 µm.

The experimental flow is depicted in Figure 3.12a, while panels 3.12b and c display the bright field and fluorescent microscope images, respectively, after a single landing event. To obtain data, the experiment is repeated six times, measuring consecutive particles and recording their landing positions. The expected

frequency shift in the first and second modes is then estimated using both the ideal mode shapes and the attenuated mode shapes from the earlier modeling section (*i.e.*, Figures 3.5 and 3.7).

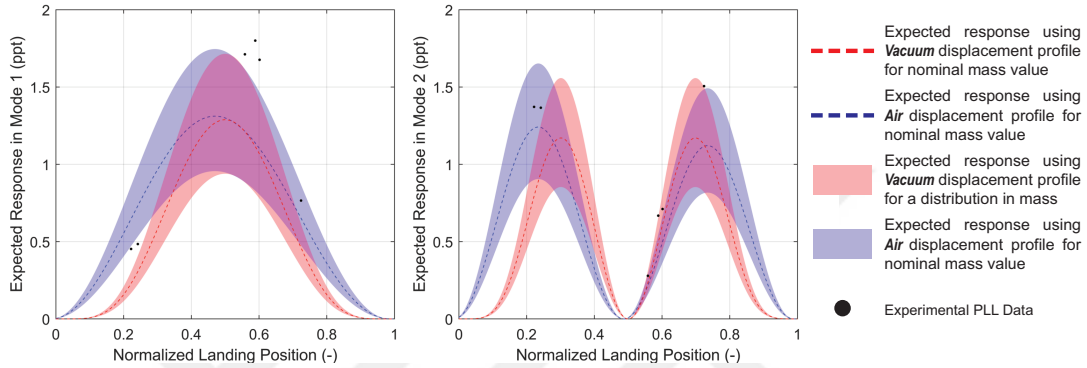

Figure 3.13: Illustration of experimental findings demonstrating the occurrence of mode shape attenuation.

Figure 3.13 showcases the results of the mode shape attenuation. The expected frequency shift solutions for the first and second modes are calculated using vacuum and air mode shapes, as shown in figures 3.5 and 3.7, respectively, for all possible landing positions ($x = [0, 1]$). The results are presented along with the measured Phase-Locked Loop (PLL) data.

It is essential to consider that nanoparticles have inherent size distribution. The 200 nm fluorescent PSNP used in the experiment exhibits a uniformity percentage below 10%, corresponding to a standard deviation ($\sigma = 20$ nm). At a confidence level of $Z = 1$, this size distribution is limited between 180 nm and 220 nm, resulting in minimum and maximum masses of 1.93 GDa and 3.53 GDa, respectively. The nominal diameter value (200 nm) yields a nominal mass value of 2.65 GDa.

Figure 3.13 presents the expected frequency shift solutions for each mode considering the mass distribution as a shaded area, while the nominal solutions are shown as dotted lines. The PLL measurements for the six detected particles are also included in the same figure and presented as dots.

Analyzing the results, it is observed that in the first mode, the three particles

landing closer to the electrodes (*i.e.*, $x \approx 0.2$ and $x \approx 0.7$) are better captured by the air mode shapes compared to the vacuum mode shapes. However, the other three particles landing closer to the center (*i.e.*, $x \approx 0.55$) are not captured by either mode shape, likely due to calibration issues related to the M_{eff} measurement. This discrepancy might be attributed to uncertainties in calculating the mode shape itself, as the mode shapes used here might not necessarily match the device utilized by Ti et al. One notable difference is that the devices utilized in this experiments has low stress SiN ($< 250MPa$) whereas the mode shapes were estimated for high stress devices (800 MPa) [3],

In the second mode, the two particles landing closer to the actuation electrodes (around $x \approx 0.2$) exhibit a better match with the air mode shape compared to the vacuum mode shape. On the other hand, the other four data points were situated at similar distances from both fittings. It is important to mention that the effective mass (M_{eff}) value was maintained constant in both analyses to ensure a fair and accurate comparison.

Overall, the experimental data exhibit a shift toward the left side (actuation electrode), indicating the presence of mode shape attenuation in NEMS mass measurement. This suggests the need for a compensation method or an improved mode shapes to enhance the accuracy of atmospheric NEMS-MS.

3.7 Potential Strategies to Address Mode Shape Attenuation

In this section, two distinct approaches to effectively account for the effect of mode shape attenuation in NEMS mass measurements are explored. These methods aim to improve the accuracy of the resulting mass spectra by accounting the effect of mode shape attenuation on the experimental data.

The first approach involves utilizing the information from the third mode of the NEMS system. The third mode, can serve as a valuable indicator of the side on which the particle landed. By analyzing the frequency shift in the third mode during the landing event, we can infer information about the particle's landing position and, subsequently, the side of the solution to be selected.

The second approach involves a statistical method that leverages error reduction to determine the side on which the particle landed. This method utilizes statistical analysis and error estimation to make an informed decision about the particle's landing position and the corresponding solution side.

3.7.1 Three Mode Experiments

In the experiments involving three modes, NEMS-MS is conducted as usual, but this time utilizing the first three out-of-plane flexural modes that operate simultaneously. When a particle lands, frequency shifts are measured in all three modes.

By employing the resolved landing position obtained from the first and second mode shapes, along with the frequency shift observed in the third mode, it becomes theoretically possible to infer whether the particle has landed closer to the drive electrode or the readout electrode (*i.e.*, x or $1 - x$). This valuable information is then used to select the appropriate side of the solution, considering the effects of mode shape attenuation, ultimately leading to enhanced accuracy

in mass measurement.

In a vacuum environment where all three modes exhibit symmetry, the frequency shift in the third mode does not provide any additional information about the correct side of landing. However, in the presence of attenuation, the breaking of inherent symmetry allows the third mode to indicate the correct landing position of the particle.

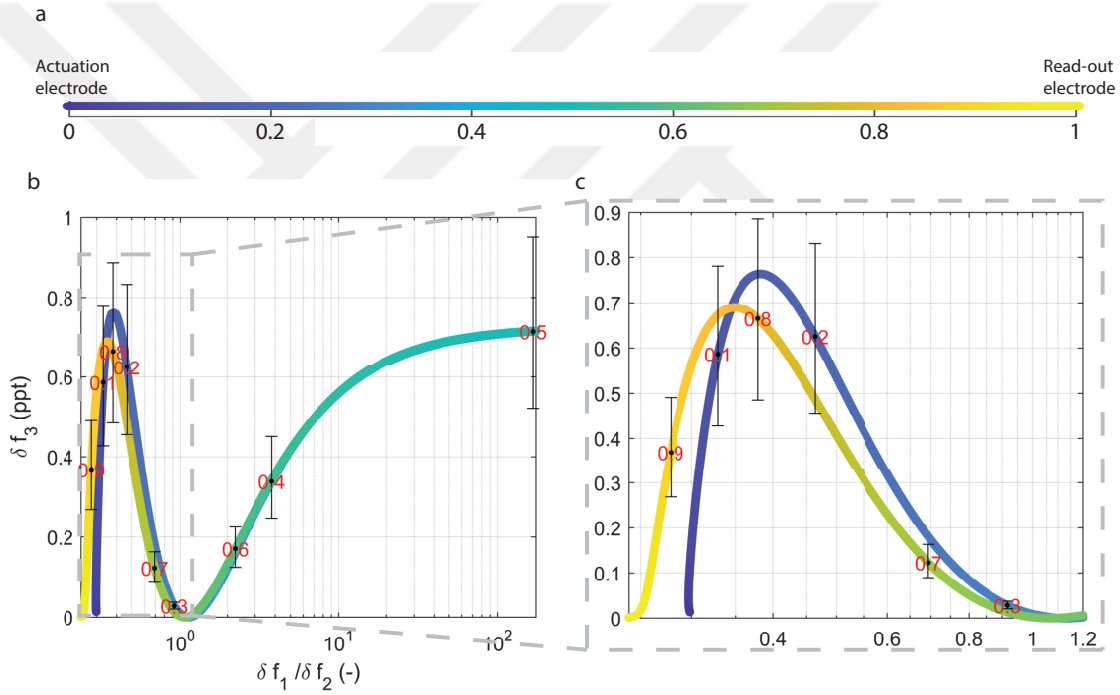

Figure 3.14: Relationship between the change in the third mode frequency (δf_3) and the ratio of changes in the first and second modes ($\delta f_1/\delta f_2$), which correspond to the landing position. Error bars in the plot represent the range of δf_3 values derived from the inherent size distribution of the 200 nm PSNP used in this analysis. Quality factors of NEMS operated in air were employed, specifically $Q_1 = 32$, $Q_2 = 54$, and $Q_3 = 73$.

Figure 3.14 demonstrates how the frequency shift in the third mode aids in identifying the landing side of particles. The relationship between the change in the frequency of the third mode and the landing position, quantified by the ratio of change in the first to the second mode, is presented in Figure 3.14b. The plot is color-coded based on the landing position along the beam, as shown in Figure 3.14a.

This relationship is particularly evident when particles land closer to the electrodes (*i.e.*, $x = 0.1 - 0.3$ or $x = 0.7 - 0.9$), as highlighted in the zoomed-in view in Figure 3.14c. Notably, the frequency shift solution in the third mode splits, suggesting that the third mode can effectively provide information about the landing side. However, as particles approach the center of the NEMS (*i.e.*, $x = 0.4 - 0.6$), the two solutions converge again, making it more challenging to distinguish the side of landing accurately. Fortunately, as we know from Figure 3.11, the error in estimating the mass is close to zero, so the knowledge of the side of the particle is not very critical for particles landing near the center.

The error bars in the plot are derived from the maximum and minimum values of δf_3, obtained from the inherent size distribution of the 200 nm PSNP used in this analysis. As seen in the zoomed-in view (Figure 3.14c), most error bars extend beyond the difference between the two curves, indicating that this analysis can only be effective for highly dispersed particles, where the impact of the size distribution is less than the difference between the two distinct solutions resulting from mode shape attenuation.

3.7.1.1 Monte Carlo Simulations

As previously discussed, the inherent size distribution of nanoparticles can have a significant effect that might exceed the detectability limits of the three-mode analysis. To investigate this, Monte Carlo simulations were conducted, involving the generation of a population of synthesized landing events, and the subsequent calculation of the expected frequency shifts in the first three modes. The mass of the particles was generated from a Gaussian distribution, with random landing positions scattered throughout the beam (*i.e.*, $x = 0$ to 1).

For 200 nm PSNP(, the masses of the 10^4 particles were generated to fit a Gaussian distribution (Figure 3.15a) with a mean of 200 nm and a standard deviation of 20 nm [64]. The histogram of the landing positions is depicted in Figure 3.15b. These Monte Carlo simulations were conducted to gain insights into the potential impact of size distribution on the analysis.

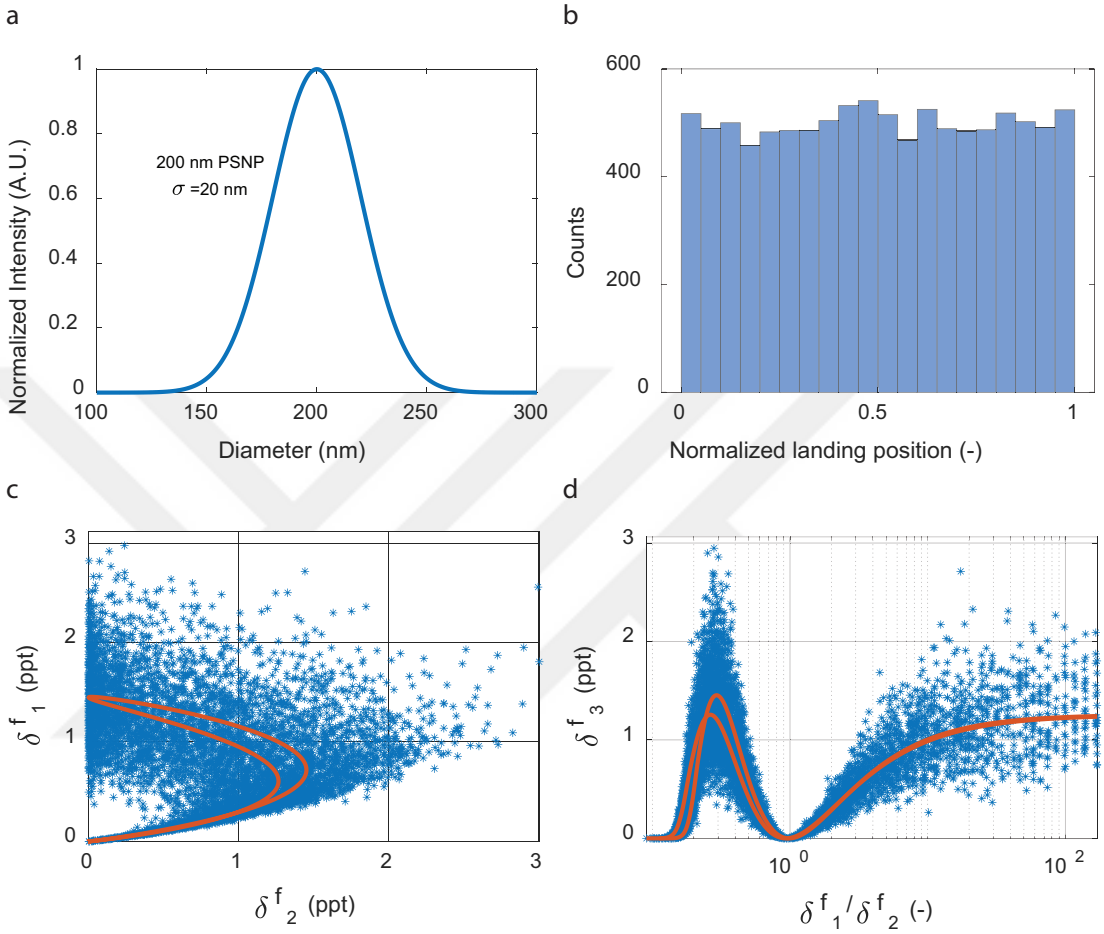

Figure 3.15: Monte Carlo simulation for 200 nm PSNP. Quality factors of NEMS operated in air were employed, specifically $Q_1 = 32$, $Q_2 = 54$, and $Q_3 = 73$.

Figure 3.15c displays the scatter plot of δf_1 *vs.* δf_2 results for the generated landing events, along with the nominal solution obtained using the mass of 200 nm PSNP (*i.e.*, 2.65 GDa) represented by the solid line. Similarly, Figure 3.15d depicts the plot of δf_3 *vs.* $\delta f_1/\delta f_2$. The wide distribution observed in the generated landing events indicates that the inherent size distribution of particles extends beyond the limit of the three-mode analysis. In other words, at this high level of size distribution, and with the available three-mode information, it becomes experimentally challenging to ascertain the side of the beam where the particle landed, leading to difficulty in selecting the correct solution for the attenuated mode shape.

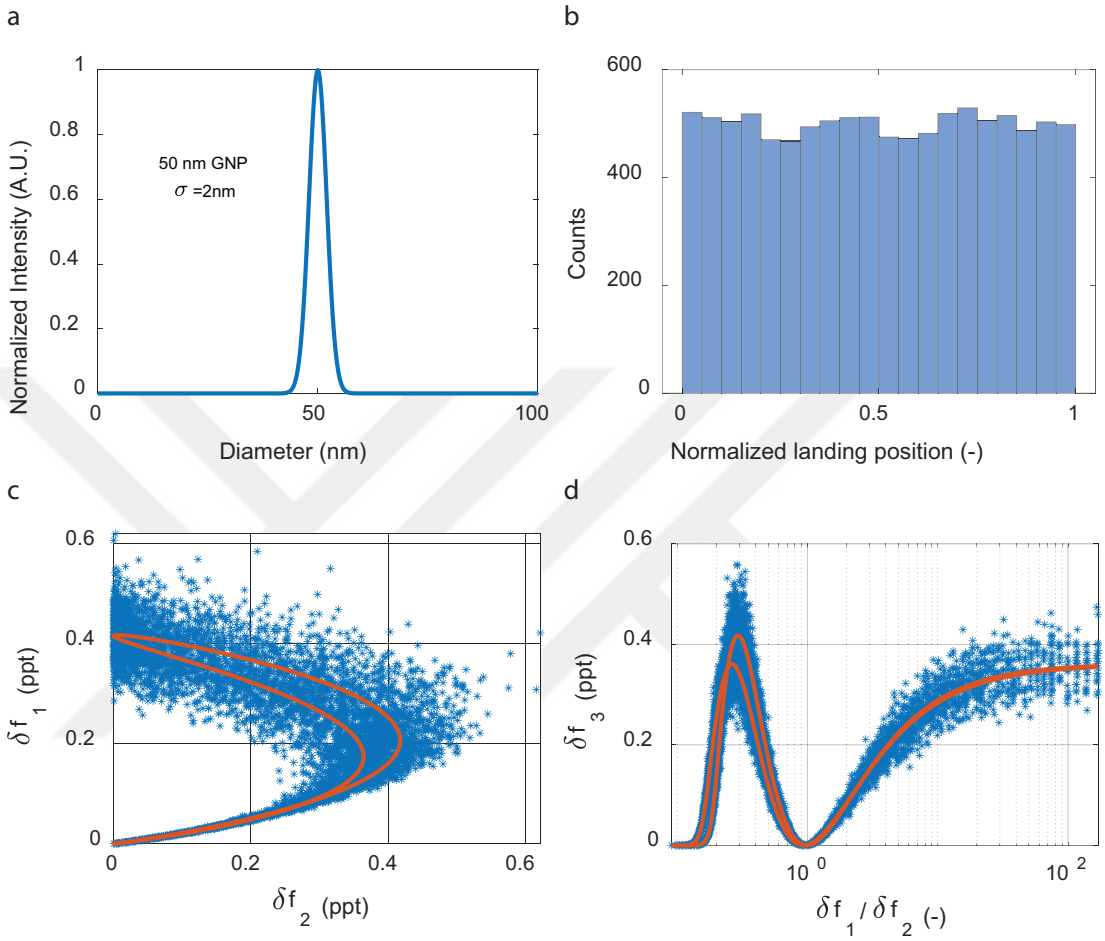

Figure 3.16: Monte Carlo simulation for 50 nm GNP. Quality factors of NEMS operated in air were employed, specifically $Q_1 = 32$, $Q_2 = 54$, and $Q_3 = 73$.

Following a similar approach, Monte Carlo simulations were performed for high-accuracy 50 nm gold nanoparticles (Nanopartz, A11-50), and the outcomes are illustrated in Figure 3.16. The simulated sample consisted of 10^4 data points, with a mass mean of 50 nm and a standard deviation of 2 nm [65], as shown in Figure 3.16a. Once more, the landing positions were randomly distributed throughout the beam, as depicted in Figure 3.16b. The findings presented in Figures 3.16c and d indicate that the three-mode analysis can be beneficial for lower dispersity nanoparticles.

3.7.2 Statistical Approach

In this section, the mode shape attenuation is taken into account and the landing side is determined through statistical methods. The underlying assumption here is that deviations from the nominal mass value are primarily attributed to mode shape attenuation, rather than variations in the particle's mass. The analysis revolves around employing the mode shape attenuation model developed previously in section 3.4 (Figure 3.7) to reevaluate data that was formerly collected and documented in [4].

Regarding the data concerning 40 nm gold nanoparticles (GNP) measured through atmospheric NEMS-MS, and outlined in [4], two potential solutions were extracted. One solution assumes the particle landed on the side closer to the drive electrode (*i.e.*, $x < 0.5$), while the other assumes it landed on the opposite side of the beam closer to the read-out electrode (*i.e.*, $x > 0.5$). The chosen solution is the one that aligns more closely with the nominal mass value of the 40 nm GNP (*i.e.*, 391 MDa). Upon reevaluating all 225 phase-locked loop (PLL) events in accordance with this criterion, 97 PLL events were attributed to the half of the beam closer to the drive electrode. In contrast, 128 PLL events were found to be closer to the assumed solution of the other half of the beam (*i.e.*, read-out electrode). The close alignment in the number of particles presumed to land on each side implies that this statistical method holds promise as a zeroth-order approximation for improving the mass spectrum.

Figure 3.17 visually presents the results from [4], alongside with the results obtained after implementing the aforementioned statistical approach. The results are depicted as histograms, alongside the plotting of the corresponding non-parametric probability density functions (PDFs) for each histogram. It is noteworthy that the outcomes achieved through the statistical approach showcase a peak that aligns more closely with the nominal mass value. Moreover, they exhibit heightened intensity when compared to the results obtained through the use of ideal mode shapes. Once more, it is essential to emphasize that this analysis

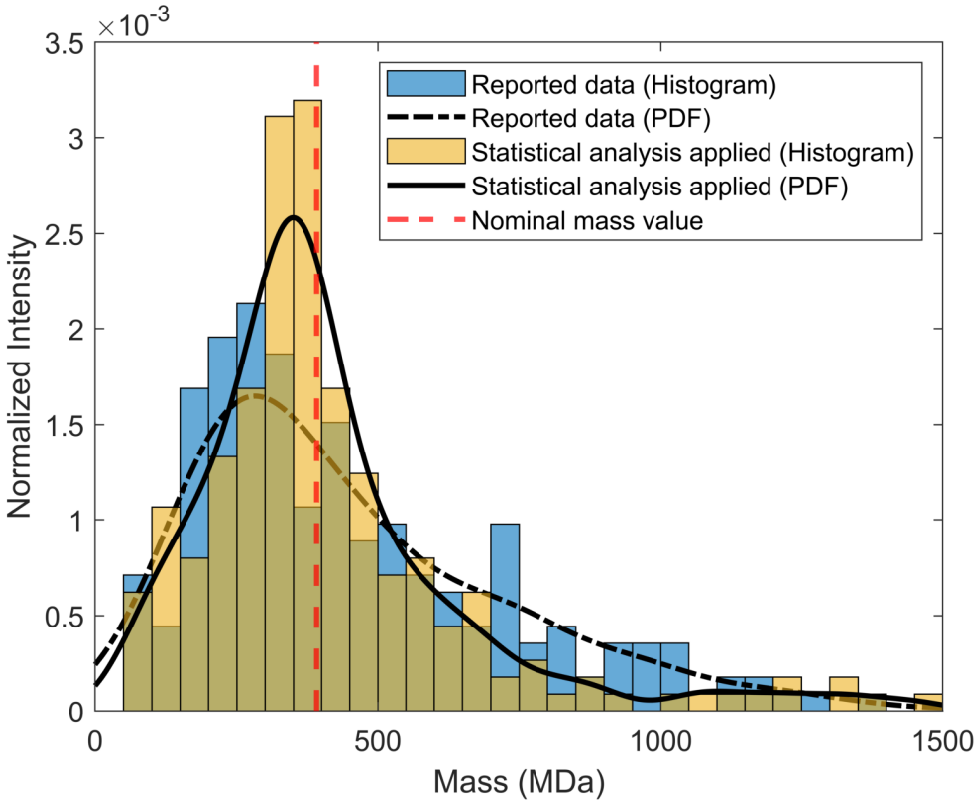

Figure 3.17: Histograms depicting mass measurements of 40 nm GNP particles, as reported by [4], and after applying the statistical approach outlined along with respective non-parametric probability density functions (PDF). The vertical line represents the nominal mass value for a 40 nm GNP particle.

is grounded on the assumption that fluctuations in frequency shifts primarily result from mode shape attenuation. This viewpoint deliberately overlooks factors such as the inherent mass distribution of the particle or variables intrinsic to the real experiment. This encompasses factors like, but not limited to, nonidealities in NEMS fabrication or variations in ESI conditions.

Chapter 4

Microwave-Based Characterization of Nanoparticle Electric Properties

This chapter is dedicated to the development of a microwave-based sensor designed specifically for determining another class of essential physical parameters – specifically, the electrical properties of nanoparticles. Accurate identification of these properties, including the nanoparticle's dielectric constant, holds utmost significance for comprehending their characteristics, optimizing functionality, and exploring potential applications in conjunction with other sensors like NEMS-MS. Functioning within the electromagnetic spectrum, the proposed sensor is designed to operate effectively under atmospheric conditions. Its primary objective is to facilitate swift determination of the dielectric constant (or an associated parameter correlated with it), thereby yielding valuable insights into the composition of the target analyte. By leveraging nanoscale microwave technology, this research endeavors to enrich the domain of nanoparticle sensing and characterization, thereby contributing to the advancement of NEMS sensing capabilities.

4.1 Microwave sensor working principle

Microwave sensors can be simplified as an RLC circuit with the sensing region aligned with the capacitor (Figure 4.1a). The RLC circuit resonates at natural frequency (f_0) that depends on the inductive and capacitance of the circuit as follows:

$$f_0 = \frac{1}{2\pi\sqrt{LC}} \tag{4.1}$$

In microwave sensing experiments, the aim is to measure the alteration in the capacitance ΔC induced by a particle landing in the constructed sensing area which subsequently leads to a frequency shift (Δf) that is detected by circuitry (Figure 4.1b). This is similar to the approach used in NEMS- based Mass Spectrometry described in Chapter 2 in the mechanical domain, where we utilized the measurement of resonance frequency change to determine the mass of the landing analyte. This detection of the change in frequency in the electromagnetic domain can be achieved directly through a Phase-locked loop (PLL), or indirectly by monitoring the phase change. The measured change in frequency in the electromagnetic domain (Δf) is related to the capacitance change by the following relationship:

$$\frac{\Delta f}{f_0} = -\frac{1\Delta C}{2C_0} \tag{4.2}$$

Where f_0 is the resonance frequency of the sensor before the analyte landing event and C_0 is the total sensor's capacitance prior to the landing event. Accurately estimating the total capacitance is crucial for establishing a relationship between the change in capacitance and the dielectric constant of the landing analytes. For simplification, let's assume the capacitor is a parallel plate capacitor with the total capacitance (C_0) of:

$$C_0 = \frac{\epsilon A}{d} \tag{4.3}$$

This shows that the capacitance primarily depends on the dielectric constant of the sensors' materials, the resonator's volume (*i.e.*, the volume of the sensing

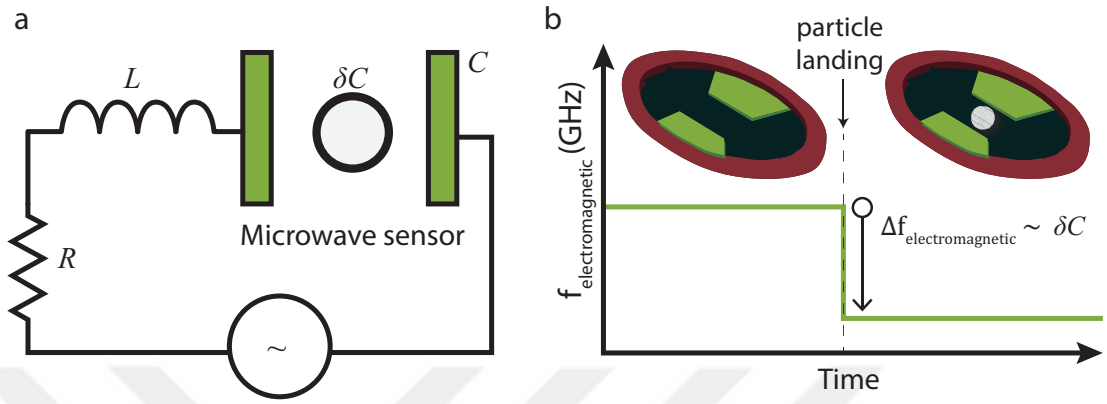

Figure 4.1: Microwave Sensor at the Nano Scale for Nanoparticle Electrical Characterization.

region), and the distance between the capacitor's conductors. However, determining the capacitance can become more intricate due to additional parasitic capacitance effects introduced by wire bonds and the PCB. Nevertheless, assuming the total capacitance is approximated, the change in capacitance resulting from the landing event can be estimated using the following equation:

$$\Delta C_0 = -2\frac{\Delta f C_0}{f_0} \tag{4.4}$$

Which can be related to the sensor and analyte parameters as in the following equation [66]:

$$\Delta C = V_{\text{particle}} \times 3K_{CM} \times \epsilon_m \times \frac{|E_{rms}(r_{\text{particle}})|^2}{U_{rms}^2} \tag{4.5}$$

Where $V_{particle}$ is the particle's volume, K_{CM} is Clausius-Mossotti factor, ϵ_m is the permittivity of the medium, E_{rms} is the root mean square of the electrical field at the particle location and U_{rms} is the rms value of the voltage difference between the conductors averaged over the entire sensor structure. The Clausius-Mossotti factor is found by the relationship below:

$$K_{CM} = \frac{\epsilon_p - \epsilon_m}{\epsilon_p + 2\epsilon_m} \tag{4.6}$$

Where ϵ_p is the dielectric constant of the particle. Based on the above, it can be inferred that if the microwave resonator is designed such that the landing particles are desorbed inside a nano-scale capacitor with known capacitance, the induced frequency shifts can be related to the change in the capacitance induced by these particles. Consequently, this change in capacitance can be correlated with the volume and dielectric constant of the particles, which are significant characteristics for nanoparticles analysis.

Microwave sensing has proven effective in various applications, including the sensing of biological cells [67, 68, 69, 70, 71, 72, 73, 66] and microparticles [74, 75] in fluidic environments. However, the specific application of microwave sensing for nanoparticles in air, as described in this context, has not been previously realized. While the technique has been successfully employed for larger particles and biological cells, its adaptation to the detection and characterization of nanoparticles in air presents a novel and unexplored area of research. The tiny size of nanoparticles necessitates the development of specialized sensing regions to accurately detect and analyze their presence. By utilizing microwave sensing for nanoparticles detection, this research aims to bridge the existing gap in knowledge and contribute to the advancement of the field.

4.2 Microwave Sensor Design

The microwave sensor comprises two primary components:

1. The microwave resonator such as a split-ring resonator (SRR), coplanar waveguide (CPW), or any other configuration which resonates at a specific frequency in the electromagnetic domain.

2. The nano-scaled gap which is connected to the microwave resonator and whose capacitance is affected by the particles that land inside it.

The two components can be either fabricated as a unified structure or separately and then interconnected using wirebonds. Figure 4.2 presents two embodiments of the proposed microwave NEMS device. In the first design, a split-ring resonator (SRR) is employed in which the sensing region extends from the inner ring to form a nano-scaled sensing region (Figure 4.2a). In the second architecture, the nano-sized gap is linked to an off-chip coplanar waveguide (CPW) microwave resonator via wirebonds (Figure 4.2b). In both variations, the sensing region is a nano-scaled gap between two electrodes where the electric field is confined (Figure 4.2c).

When a particle lands in the small sensing region, the particle replaces the gap

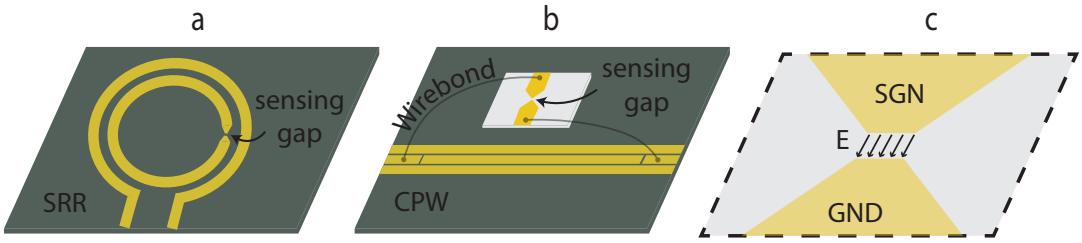

Figure 4.2: Microwave resonator proposed. (a) Split-ring resonator (SRR) with a nano-scale sensing region in the inner ring or (b) Coplanar waveguide (CPW) fabricated off the chip containing the sensing gap and interconnected by wirebonds. Panel (c) illustrates the nano-scale sensing gap that is situated between two electrodes (signal and ground).

medium and therefore alters the dielectric constant inside the nano-scaled capacitor. These changes modify the resonance frequency of the microwave resonator. The changes in the resonance frequency can be tracked by a custom electronic circuit based on Phase-locked loop (PLL). The measurement circuit comprises several components. A signal generator is used to drive the resonator, providing the necessary excitation. Secondly, a detection circuitry is employed to determine the phase of the resonator at the applied frequency while a proportional Integral (PI) controller is utilized to update the resonance frequency of the signal generator's low-pass filter (LPF). This detection and measurement scheme was similar to the circuitry constructed in [74].

4.3 Proof of Concept Demonstration

To demonstrate the feasibility of the concept, a microwave resonator coupled with a nano-scale sensing region was fabricated and tested (Figure 4.3). The sensing region, as shown in Figure 4.3b, is composed of two conductive (gold) pads measuring 150 µm x 150 µm that converge into a narrow 5 µm wide region, separated by a distance of 500 nm. These gold electrodes are 100 nm thick. These pads serve the purpose of wire bonding the device to a microwave resonator, which is directly printed onto the printed circuit board (PCB).

The microwave resonator is a Coplanar waveguide (CPW) is constructed with three conductive trace legs deposited on a substrate made of glass-reinforced epoxy resin laminate (FR4: TG150), measuring 1.6 mm in thickness. Each of these conductive traces possesses a width of 3 mm and is made from 1 oz Copper (equivalent to a thickness of 35 µm), with a gold immersion surface finish to enhance adhesion during wire bonding. The ground traces, located on the sides, extend for 12 mm, while the central signal trace extends for 16 mm and maintains a 1 mm spacing from each of the ground traces. The CPW mask, along with its dimensions, is illustrated in Figures A.6 and A.7 in the Appendix.

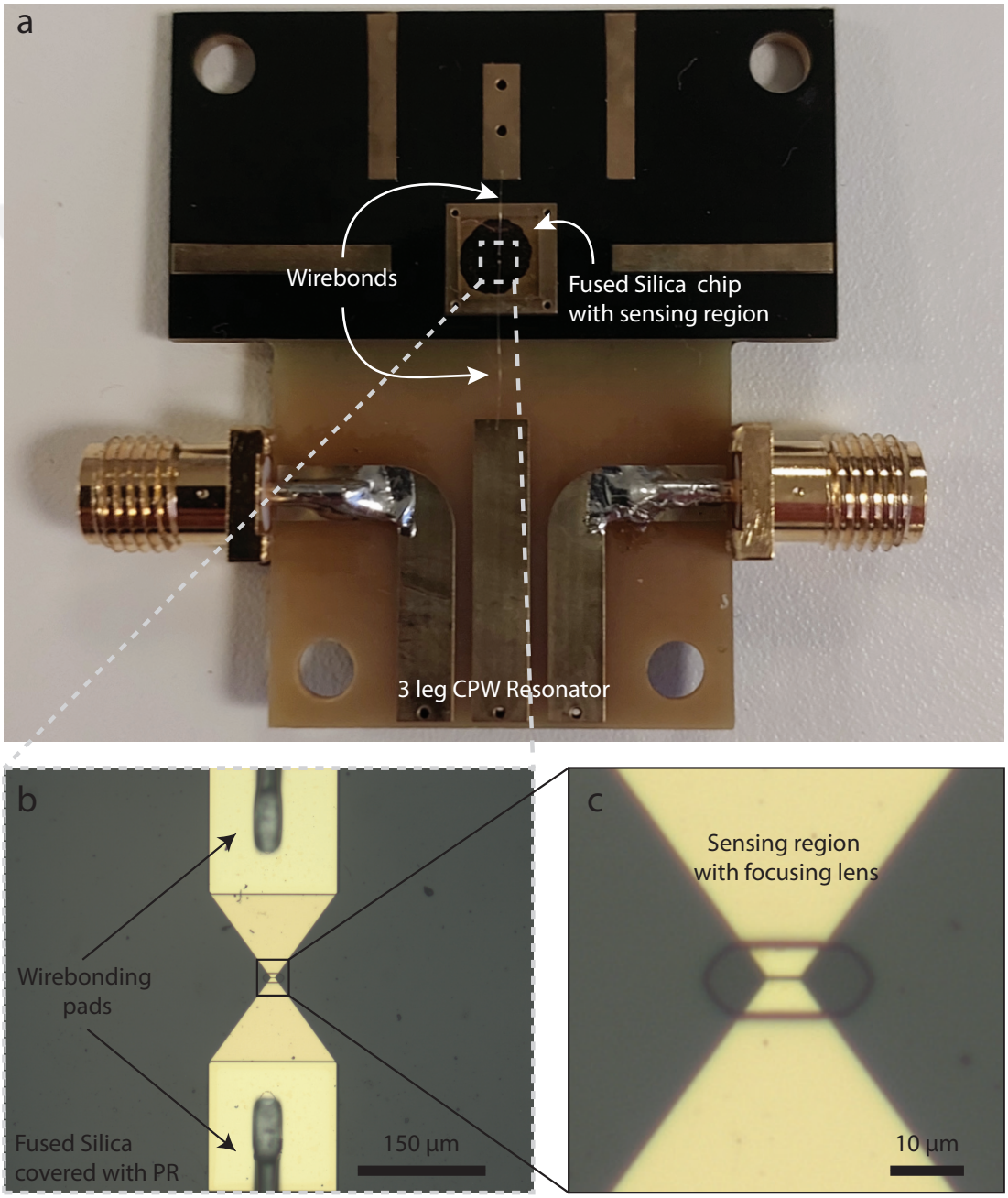

Figure 4.3: Nano-scale sensing region with self-focusing ion lens.

4.4 Nanoscale Sensing Region Fabrication

Initially, a 4 × 4 mm fused silica chip (University Wafer) is diced and cleaned. Fused Silica is used due to its insulating nature. Subsequently, a 2 µm thick photoresist (AZ 5214) layer was coated onto the fused silica chip. Photolithography is performed using a chromium mask containing the desired pattern. Following development, the pattern is transferred into the photoresist layer, as depicted in Figure 4.4b.

Next, a 100 nm gold layer is thermally evaporated onto the chip, and a lift-off process is carried out to create the nano-scaled gap, as shown in Figure 4.4d. To integrate a polymeric focusing lens, a thick layer of photoresist (AZ 4533) is applied onto the fused silica chip with the nano-scale gap. Another photolithography step is employed to create an opening that aligns with the nano-gap, enabling the focusing of incoming particles. The dimensions of the focusing lens are similar to those used for the NEMS mass sensors described in Chapter 2. Additionally, the bonding pads are exposed during the photolithography step to facilitate wire bonding, as depicted in Figure 4.4f.

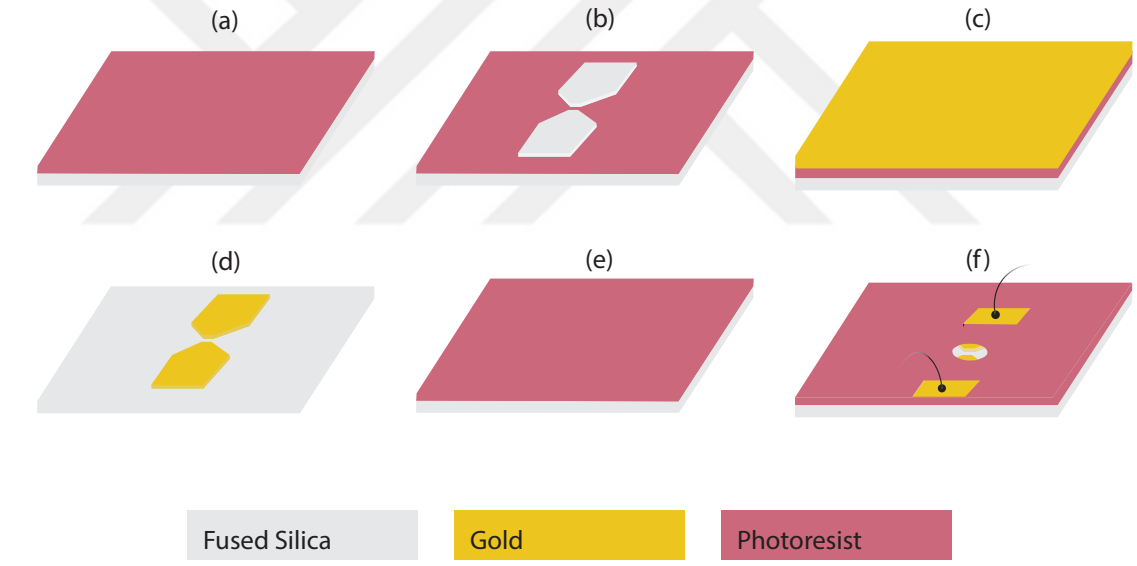

Figure 4.4: Microwave nano-scale sensing region fabrication.

4.5 Proof of Concept Experiment

The in-house built electrospray ionization (ESI) setup was used to ionize and transport 100 nm fluorescent polystyrene nanoparticles (PSNP) to the sensing region. In this experiment, 40µL of two-fold diluted polystyrene nanoparticles solution (Fluoro-Max G100, ThermoFisher) was mixed with 900µL of 80mM Ammonium Acetate (NH4Ac) and 100µL methanol. The final concentration of the nanoparticles in the solution was 7.1×10^9 particle/mL. Prior to spraying the nano-scale sensing chip, we sprayed an empty chip which features a focusing lens on the center of the chip (Figure 4.5a & b). This is done before each experiment to confirm the ESI and focusing window are working as intended and to confirm that there is no cross-contamination. Next, the PCB containing the CPW microwave resonator and the nano gap is loaded into the ESI system and was sprayed for one hour. During this time, the change in phase and amplitude was continuously measured by the PLL system (Figure 4.6a) which tracks the voltage amplitude and phase change with time.

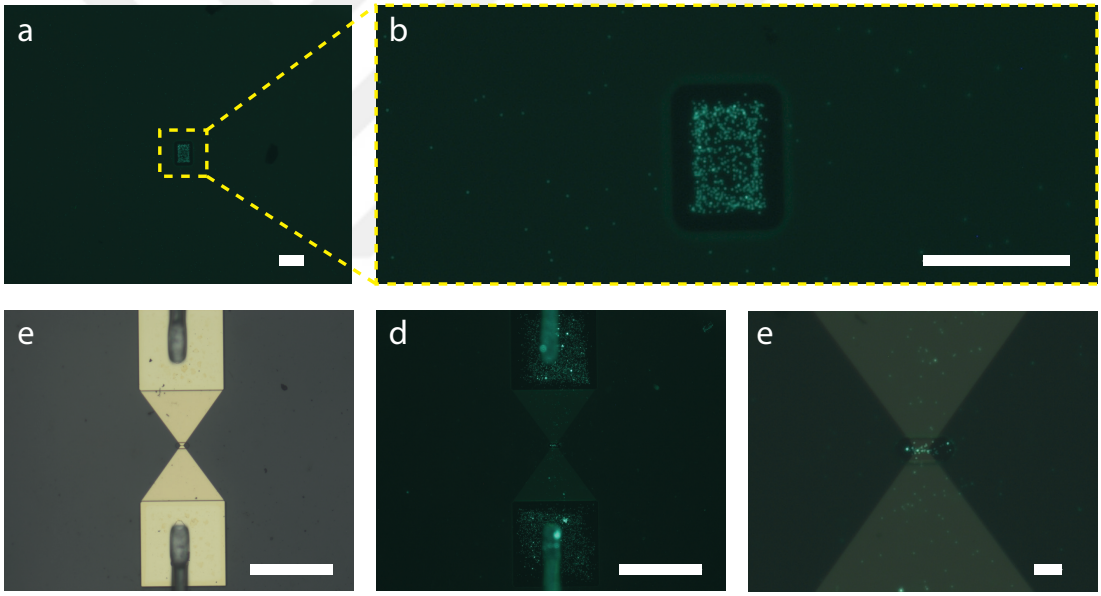

Figure 4.5: Microwave sensing experiment with 100nm fluorescent polystyrene nanoparticles.

4.6 Results

Two types of events were observed namely spike-like and step-like (Figure 4.6b). We attribute the spike like events to water droplets with no nanoparticles that replaces air in the nano-gap and evaporates very fast leaving no net change in phase nor in amplitude. The step-like events are the events that are expected from nanoparticle absorption in the sensing region and these events were recorded and reported in the results (Figure 4.6c-f). As a positive control, an experiment was conducted in which we sprayed the ESI solution without any nanoparticles inside. This was done to confirm that the frequency shifts are due to the particles coming to the sensing region. The solution was made by mixing 900 µL of 80mM Ammonium Acetate (NH4Ac) with 100 µL methanol. For both the control experiment and experiment with 100 nm PSNP, the step-like changes in phase and amplitude were recorded and reported (Figure 4.6c and d).

For each event, the phase and amplitude data were converted from polar coordinates to cartesian coordinates by the following conversion [75]:

$$\Delta Y = \Delta R \sin\left(\theta + \theta_{\text{intrinsic}}\right) + R \cos\left(\theta + \theta_{\text{intrinsic}}\right) \Delta\theta \tag{4.7}$$

Where R and θ are initial amplitude and phase at an event and ΔR and $\Delta\theta$ are the change of amplitude and phase in the event. $\theta_{\text{intrinsic}}$ is the intrinsic phase that is set to a specific value between zero and 2π. Since the measurement observed in the lock-in amplifier is oscillating (Figure 4.6a) and we are trying to measure it with a lock-in amplifier which calculates the difference between the signal it provides and reads and not the phase at resonance. In theory, when the device is driven at resonance, the resonator phase must be zero. However, in practice, this phase is unknown and that is why it is referred to as the intrinsic phase [75]. ΔY is calculated based on the equation above for $\theta_{\text{intrinsic}}$ swept between 0 and 2π, next the value of $\theta_{\text{intrinsic}}$ is chosen to maximize the contrast in ΔY measurements for all the observed events.

Figure 4.7 shows the ΔY histograms for the events from both the control and PSNP runs calculated at intrinsic phase values of 1.07π and 1.4π respectively. It

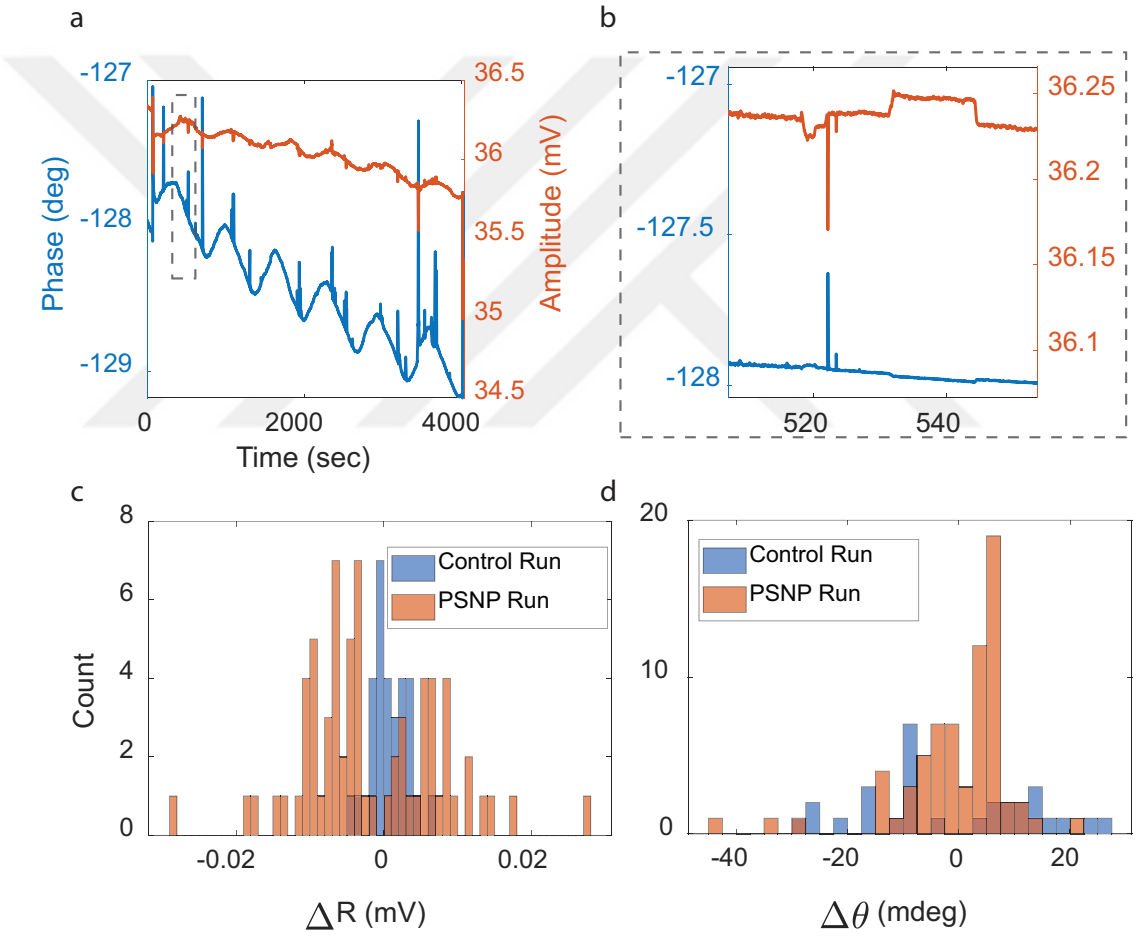

Figure 4.6: PLL Data and results from the 100 nm polystyrene nanoparticles spray and control solution spray.

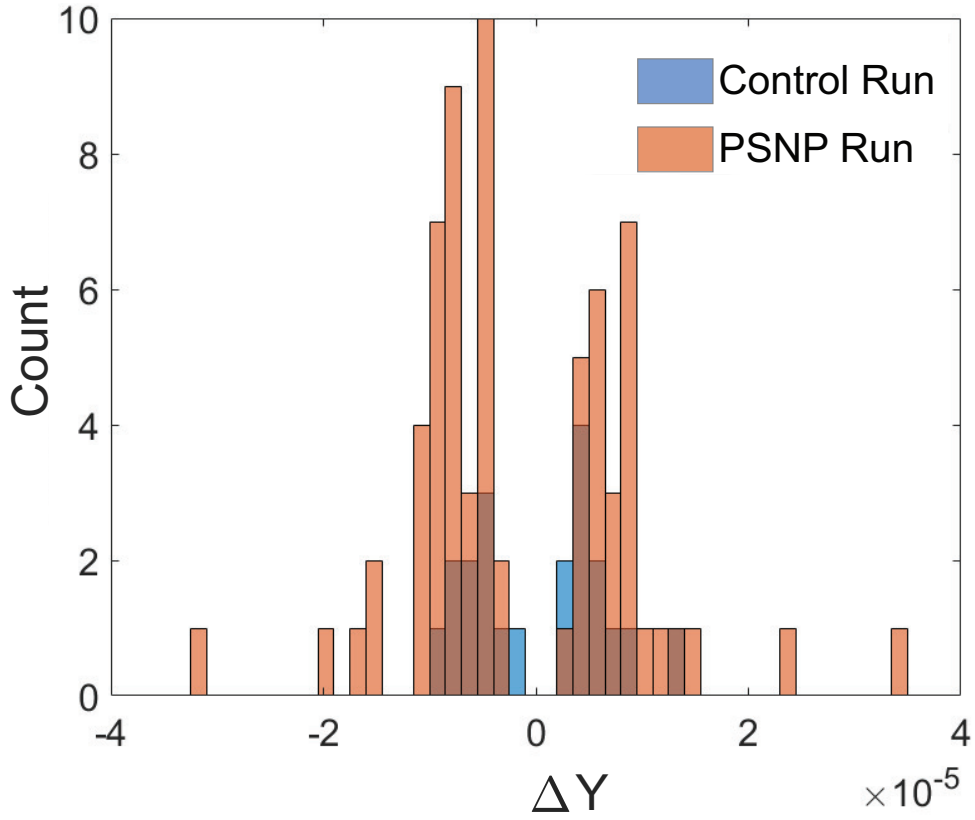

Figure 4.7: ΔY histogram for control and 100 nm PSNP experiments with intrinsic phase of 1.07π and 1.4π, respectively.

is evident that there is a peak emerging for the 100 nm PSNP run. The shifts in the control run are attributed to the salt crystals due to the ESI operation.

4.7 Discussion and Future Work

To gain a more comprehensive understanding of the nanoparticles sensing with the proposed microwave device, it is imperative to conduct further investigations. In this section, I put forward a series of experiments that aim to explore the underlying mechanisms and help understand the results obtained (Figure 4.6 and Figure 4.7) . By conducting these proposed experiments, we can elucidate the factors influencing the response of the microwave device to different particle volumes and determine whether the observed similarities in response are consistent across various particle types.

To further enhance the precision of these investigations, it is suggested to employ a narrower ion lens. By implementing this modification, the particles can be effectively directed to land inside the designated sensor region, which in this case is a 5 µm x 500 nm area. This strategic arrangement ensures that the sensing primarily takes place in the electric field within the gap, rather than being affected by the fringing field in other areas (Figure 4.5e). This refinement enables more controlled measurements, thus providing more accurate insights into the effect of particles landing in the sensing region.

One avenue for future research is to explore the influence of particle size on the microwave device's sensitivity and response. This can be accomplished by systematically varying the particle sizes within a specific range and measuring their corresponding effects on the phase and amplitude. By doing so, we can quantitatively assess any size-dependent trends and evaluate how the measurements are affected by particle volume. Additionally, investigating the impact of different particle properties, such as composition and surface characteristics, would provide valuable insights. By introducing particles with varying compositions or surface modifications, we can assess how these factors influence the device's response and whether they contribute to the observed similarities in the results. This analysis can help us understand the specific interactions between the particles and the device, leading to a deeper understanding of the sensing mechanisms involved.

Furthermore, exploring the temporal dynamics of particle-device interaction can provide crucial information. By monitoring the response of the device over time, we can observe any transient or time-dependent effects that may occur during the sensing process. This investigation would enable us to discern whether the observed responses are instantaneous or if they evolve over time, potentially indicating additional underlying phenomena. It is also crucial to conduct a comprehensive investigation into the intrinsic phase presented in [75]. This aspect holds significant importance in accurately determining the change in capacitance (ΔC), which, in turn, enables the correlation of microwave measurements with physical measurements of the dielectric constant.

Furthermore, beyond the proposed experimental paths, there is a need for further optimization in relation to the CPW device and its connection scheme to the nanosized sensing gap. This include optimizing the geometry of the microwave resonator and transitioning to an improved PCB substrate material like Rogers 4350b, known for its reduced signal loss compared to the currently used FR4 material.

Moreover, the fused silica chips utilized in the fabrication of the nanoscale sensing gap could be upgraded to materials such as Alumina, or alternatives with lower dielectric loss tangent. It's also noteworthy to suggest that for the upcoming iterations of these devices, the removal of the conductive paste used to adhere the fused silica chip to the PCB, in favor of an insulating gluing compound, would be advisable.

Chapter 5

Conclusion

5.1 Summary

This dissertation presents a comprehensive investigation of Nanoelectromechanical systems based mass spectrometry (NEMS-MS), a promising approach for weighing particles that are too large for conventional Mass Spectrometry (MS) techniques. A novel and advanced approach is proposed, allowing the entire sensing process to occur under atmospheric conditions, a previously unexplored area in NEMS-MS. Challenges associated with conducting experiments in an atmospheric environment, such as dissipation due to viscous damping, are addressed. Moreover, the dissertation proposes another class of sensors operating at electromagnetic domain. The proposed microwave sensor device aims at gather electrical properties of the nanoparticles sprayed.

In Chapter 1, a thorough review of mass spectrometry techniques is provided, along with a comparison of competitive NEMS-MS approaches. The history of NEMS-MS and recent advancements are presented chronologically. The main motivation behind this work is to propose a system capable of measuring particles that are too large for conventional mass spectrometry, effectively closing the technology gap.

Chapter 2 focuses on the utilization of the proposed atmospheric NEMS-MS system to detect and measure the mass of two types of viruses: SARS-CoV-2 and BoHV-1. The working principle of NEMS-MS and its governing equations are explained. The device fabrication and components of the in-house electrospray ionization system are illustrated. The virus preparation procedure for ionization and measurement is detailed, and the results are presented.

Chapter 3 delves into the investigation of how the operation of NEMS-MS entirely under atmospheric conditions can affect the resulting mass spectra. Particularly, the deviation of the displacement profiles from the undamped eigenfunctions solution due to air damping is analyzed and discussed.

Chapter 4 of this dissertation introduces another class of sensors, microwave-based sensors that are intended to leverage the sensing and characterization of nanoparticles by inferring vital information related to its electrical properties.

5.2 Outlook and Future Work

In this section, we present a road map for future research lines aimed at enhancing and advancing atmospheric NEMS-MS into a universal characterization tool. These potential research directions are envisioned to broaden the scope and capabilities of NEMS-MS, making it applicable in a wide range of scientific and industrial contexts.

1. Optimized Atmospheric NEMS-MS Setup:

To further enhance the proposed atmospheric NEMS-MS system, rigorous exploration and refinement are recommended. One crucial aspect to address is minimizing the impact of air damping on the Quality factor and displacement profiles. One promising approach is operating the NEMS-MS under different gases, such as Helium, which can yield up to four times enhancement in the

Quality factor compared to air at atmospheric pressure [76]. Moreover, employing atmospheric NEMS-MS in conjunction with microwave sensors while using gases other than air, which possess distinct dielectric constants, has the potential to yield improved capacitance measurements [77].

To achieve this, the system can be placed inside an enclosed environment, such as a glovebox or dry box. This controlled setup can significantly improve the performance of the NEMS-MS system by mitigating the effects of air damping. Furthermore, operating the NEMS-MS within a glovebox offers better control over experiment parameters like humidity and temperature, known to impact NEMS-MS in both the mechanical and electromagnetic domains.

2. Novel NEMS Devices:

Continuing the optimization of NEMS devices is crucial to enhance their performance under atmospheric conditions and reduce susceptibility to deviations in displacement profiles. The development of the single-mode NEMS-MS [78], which I recently co-developed, is a significant step in this direction.

Another promising research avenue involves optimizing 3D focusing lenses to precisely direct incoming analytes towards specific locations on the NEMS devices. This optimization aims to achieve superior focusing of analytes, leading to a clearer and more predictable response from the NEMS devices. By accurately focusing the incoming analytes, particularly directing them to the center of the NEMS device where the uncertainty in mass measurement is lowest, we can greatly enhance the system's sensitivity and accuracy. This enhancement in focusing capabilities will contribute to the overall sensitivity and accuracy of the NEMS-MS system as well as enhancing the capture efficiency of the technique, making it an even more powerful and effective tool for universal characterization.

By focusing on novel designs and nanofabrication techniques, we can establish NEMS devices with better capabilities at atmospheric pressure, enabling them to produce more reliable PLL results and therefore better mass analysis.

3. Explore real-world applications:

An important direction for future research is to explore the practical applications of NEMS-MS in real-world scenarios, spanning various fields such as environmental monitoring, medical diagnostics, and pharmaceutical analysis. Leveraging NEMS-MS under atmospheric conditions to detect, measure, and characterize nanoplastics holds immense potential for understanding their abundance in everyday products and assessing their medical risks. This novel application of NEMS-MS can shed light on the presence and impact of nanoplastics, contributing to our understanding of environmental health and safety.

Furthermore, by showcasing the capability of NEMS-MS in addressing critical issues like nanoplastics, it will raise awareness and promote the technology's adoption in diverse industries and scientific communities.

4. Integration of NEMS-MS with Microwave Sensing:

Continuing the investigation of integrating NEMS-MS with microwave sensing is a promising avenue for future research. This integration aims to capitalize on the complementary strengths of both technologies to enhance the overall characterization capabilities.

By combining NEMS-MS for mass measurement, with microwave sensing, which provides valuable electrical properties, the integrated system can offer a more comprehensive and detailed characterization of nanoparticles and molecules. This allows for simultaneous measurement of mass and material properties, providing valuable insights into complex samples. Further research can focus on optimizing the integration process and exploring different sensing configurations.

Bibliography

[1] S. Banerjee and S. Mazumdar, "Electrospray Ionization Mass Spectrometry: A Technique to Access the Information beyond the Molecular Weight of the Analyte," *International Journal of Analytical Chemistry*, vol. 2012, p. 282574, Mar. 2012. Publisher: Hindawi Publishing Corporation.

[2] S. Dominguez-Medina, S. Fostner, M. Defoort, M. Sansa, A.-K. Stark, M. A. Halim, E. Vernhes, M. Gely, G. Jourdan, T. Alava, P. Boulanger, C. Masselon, and S. Hentz, "Neutral mass spectrometry of virus capsids above 100 megadaltons with nanomechanical resonators," *Science*, vol. 362, no. 6417, pp. 918–922, 2018.

[3] C. Ti, J. G. McDaniel, A. Liem, H. Gress, M. Ma, S. Kyoung, O. Svitelskiy, C. Yanik, I. I. Kaya, M. S. Hanay, M. González, and K. L. Ekinci, "Dynamics of NEMS resonators across dissipation limits," *Applied Physics Letters*, vol. 121, p. 023506, 07 2022.

[4] R. T. Erdogan, M. Alkhaled, B. E. Kaynak, H. Alhmoud, H. S. Pisheh, M. Kelleci, I. Karakurt, C. Yanik, Z. B. Şen, B. Sari, A. M. Yagci, A. Özkul, and M. S. Hanay, "Atmospheric pressure mass spectrometry of single viruses and nanoparticles by nanoelectromechanical systems," *ACS Nano*, vol. 16, no. 3, pp. 3821–3833, 2022. PMID: 35785967.

[5] A. M. Haag, *Mass Analyzers and Mass Spectrometers*, pp. 157–169. Cham: Springer International Publishing, 2016.

[6] I. Falconer, "J j thomson and the discovery of the electron," *Physics Education*, vol. 32, p. 226, jul 1997.

[7] J. Griffiths, "A Brief History of Mass Spectrometry," *Analytical Chemistry*, vol. 80, pp. 5678–5683, Aug. 2008. Publisher: American Chemical Society.

[8] Anonymous, "Proceedings of the american physical society," *Phys. Rev.*, vol. 69, pp. 674–674, Jun 1946.

[9] M. Dole, L. L. Mack, R. L. Hines, R. C. Mobley, L. D. Ferguson, and M. B. Alice, "Molecular beams of macroions," *The Journal of Chemical Physics*, vol. 49, pp. 2240–2249, Sept. 1968.

[10] M. Karas, U. Bahr, and F. Hillenkamp, "Uv laser matrix desorption/ionization mass spectrometry of proteins in the 100 000 dalton range," *International Journal of Mass Spectrometry and Ion Processes*, vol. 92, no. C, p. 231 – 242, 1989.

[11] M. A. Grayson, *Measuring mass: from positive rays to proteins*. Chemical Heritage Foundation, 2002.

[12] M. F. Jarrold, "Applications of charge detection mass spectrometry in molecular biology and biotechnology," *Chemical Reviews*, vol. 122, no. 8, pp. 7415–7441, 2022. PMID: 34637283.

[13] M. Mann, C. K. Meng, and J. B. Fenn, "Interpreting mass spectra of multiply charged ions," *Analytical Chemistry*, vol. 61, no. 15, pp. 1702–1708, 1989.

[14] T. P. Burg, M. Godin, S. M. Knudsen, W. Shen, G. Carlson, J. S. Foster, K. Babcock, and S. R. Manalis, "Weighing of biomolecules, single cells and single nanoparticles in fluid," *Nature*, vol. 446, pp. 1066–1069, Apr. 2007.

[15] O. Malvar, J. J. Ruz, P. M. Kosaka, C. M. Domínguez, E. Gil-Santos, M. Calleja, and J. Tamayo, "Mass and stiffness spectrometry of nanoparticles and whole intact bacteria by multimode nanomechanical resonators," *Nature Communications*, vol. 7, p. 13452, Nov. 2016.

[16] A. Sanz-Jimenez, J. J. Ruz, E. Gil-Santos, O. Malvar, S. Garcia-Lopez, P. M. Kosaka, A. Cano, M. Calleja, and J. Tamayo, "Square membrane resonators supporting degenerate modes of vibration for high-throughput

mass spectrometry of single bacterial cells," *ACS Sensors*, vol. 0, no. 0, p. null, 0. PMID: 37122237.

[17] C. Comby-Zerbino, X. Dagany, F. Chirot, P. Dugourd, and R. Antoine, "The emergence of mass spectrometry for characterizing nanomaterials. atomically precise nanoclusters and beyond," *Mater. Adv.*, vol. 2, pp. 4896–4913, 2021.

[18] M. M. Atalla, E. Tannenbaum, and E. J. Scheibner, "Stabilization of silicon surfaces by thermally grown oxides," *The Bell System Technical Journal*, vol. 38, no. 3, pp. 749–783, 1959.

[19] M. Roukes and K. Ekinci, "An apparatus and method for ultrasensitive nanoelectromechanical mass detection," Nov. 2002.

[20] K. L. Ekinci, X. M. H. Huang, and M. L. Roukes, "Ultrasensitive nanoelectromechanical mass detection," *Applied Physics Letters*, vol. 84, pp. 4469–4471, 05 2004.

[21] Y. T. Yang, C. Callegari, X. L. Feng, K. L. Ekinci, and M. L. Roukes, "Zeptogram-scale nanomechanical mass sensing," *Nano Letters*, vol. 6, no. 4, pp. 583–586, 2006. PMID: 16608248.

[22] A. K. Naik, M. S. Hanay, W. K. Hiebert, X. L. Feng, and M. L. Roukes, "Towards single-molecule nanomechanical mass spectrometry," *Nature Nanotechnology*, vol. 4, no. 7, pp. 445–450, 2009.

[23] M. S. Hanay, S. Kelber, A. K. Naik, D. Chi, S. Hentz, E. C. Bullard, E. Colinet, L. Duraffourg, and M. L. Roukes, "Single-protein nanomechanical mass spectrometry in real time," *Nature Nanotechnology*, vol. 7, no. 9, pp. 602–608, 2012.

[24] J. Chaste, A. Eichler, J. Moser, G. Ceballos, R. Rurali, and A. Bachtold, "A nanomechanical mass sensor with yoctogram resolution," *Nature Nanotechnology*, vol. 7, pp. 301–304, May 2012.

[25] B.-D. Chan, K. Icoz, W. Huang, C.-L. Chang, and C. A. Savran, "On-demand weighing of single dry biological particles over a 5-order-of-magnitude dynamic range," *Lab Chip*, vol. 14, pp. 4188–4196, 2014.

[26] E. Sage, A. Brenac, T. Alava, R. Morel, C. Dupré, M. S. Hanay, M. L. Roukes, L. Duraffourg, C. Masselon, and S. Hentz, "Neutral particle mass spectrometry with nanomechanical systems," *Nature Communications*, vol. 6, p. 6482, Mar. 2015.

[27] O. Malvar, J. J. Ruz, P. M. Kosaka, C. M. Domínguez, E. Gil-Santos, M. Calleja, and J. Tamayo, "Mass and stiffness spectrometry of nanoparticles and whole intact bacteria by multimode nanomechanical resonators," *Nature Communications*, vol. 7, p. 13452, Dec. 2016.

[28] M. S. Hanay, R. T. Erdogan, M. Alkhaled, and H. S. Pisheh, "Device for obtaining the mass of single nanoparticles, viruses and proteins in suspension or in solution with high-collection efficiency," Oct. 2021.

[29] M. Yuksel, E. Orhan, C. Yanik, A. B. Ari, A. Demir, and M. S. Hanay, "Nonlinear nanomechanical mass spectrometry at the single-nanoparticle level," *Nano Letters*, vol. 19, no. 6, pp. 3583–3589, 2019. PMID: 31117750.

[30] V. U. Weiss, R. Pogan, S. Zoratto, K. M. Bond, P. Boulanger, M. F. Jarrold, N. Lyktey, D. Pahl, N. Puffler, M. Schelhaas, E. Selivanovitch, C. Uetrecht, and G. Allmaier, "Virus-like particle size and molecular weight/mass determination applying gas-phase electrophoresis (native nes gemma)," *Analytical and bioanalytical chemistry*, vol. 411, p. 5951—5962, September 2019.

[31] V. U. Weiss, J. Z. Bereszczazk, M. Havlik, P. Kallinger, I. Gösler, M. Kumar, D. Blaas, M. Marchetti-Deschmann, A. J. R. Heck, W. W. Szymanski, and G. Allmaier, "Analysis of a common cold virus and its subviral particles by gas-phase electrophoretic mobility molecular analysis and native mass spectrometry," *Analytical Chemistry*, vol. 87, no. 17, pp. 8709–8717, 2015. PMID: 26221912.

[32] G. Young, N. Hundt, D. Cole, A. Fineberg, J. Andrecka, A. Tyler, A. Olerinyova, A. Ansari, E. G. Marklund, M. P. Collier, S. A. Chandler, O. Tkachenko, J. Allen, M. Crispin, N. Billington, Y. Takagi, J. R. Sellers, C. Eichmann, P. Selenko, L. Frey, R. Riek, M. R. Galpin, W. B. Struwe, J. L. P. Benesch, and P. Kukura, "Quantitative mass imaging of single biological macromolecules," *Science*, vol. 360, no. 6387, pp. 423–427, 2018.

[33] A. Sonn-Segev, K. Belacic, T. Bodrug, G. Young, R. T. VanderLinden, B. A. Schulman, J. Schimpf, T. Friedrich, P. V. Dip, T. U. Schwartz, B. Bauer, J.-M. Peters, W. B. Struwe, J. L. P. Benesch, N. G. Brown, D. Haselbach, and P. Kukura, "Quantifying the heterogeneity of macromolecular machines by mass photometry," *Nature Communications*, vol. 11, p. 1772, Apr. 2020.

[34] D. Z. Keifer, E. E. Pierson, and M. F. Jarrold, "Charge detection mass spectrometry: weighing heavier things," *Analyst*, vol. 142, pp. 1654–1671, 2017.

[35] S. D. Fuerstenau, W. H. Benner, J. J. Thomas, C. Brugidou, B. Bothner, and G. Siuzdak, "Mass spectrometry of an intact virus," *Angewandte Chemie International Edition*, vol. 40, no. 3, pp. 541–544, 2001.

[36] E. E. Pierson, D. Z. Keifer, L. Selzer, L. S. Lee, N. C. Contino, J. C.-Y. Wang, A. Zlotnick, and M. F. Jarrold, "Detection of late intermediates in virus capsid assembly by charge detection mass spectrometry," *Journal of the American Chemical Society*, vol. 136, no. 9, pp. 3536–3541, 2014. PMID: 24548133.

[37] T. Doussineau, C. Mathevon, L. Altamura, C. Vendrely, P. Dugourd, V. Forge, and R. Antoine, "Mass determination of entire amyloid fibrils by using mass spectrometry," *Angewandte Chemie International Edition*, vol. 55, no. 7, pp. 2340–2344, 2016.

[38] T. P. Wörner, J. Snijder, A. Bennett, M. Agbandje-McKenna, A. A. Makarov, and A. J. R. Heck, "Resolving heterogeneous macromolecular assemblies by Orbitrap-based single-particle charge detection mass spectrometry," *Nature Methods*, vol. 17, pp. 395–398, Apr. 2020.

[39] Z. Baird, P. Wei, and R. G. Cooks, "Ion creation, ion focusing, ion/molecule reactions, ion separation, and ion detection in the open air in a small plastic device," *Analyst*, vol. 140, pp. 696–700, 2015.

[40] Z. Baird, W.-P. Peng, and R. G. Cooks, "Ion transport and focal properties of an ellipsoidal electrode operated at atmospheric pressure," *International*

Journal of Mass Spectrometry, vol. 330-332, pp. 277–284, 2012. SI: Armentrout Honor Issue.

[41] H. Kim, J. Kim, H. Yang, J. Suh, T. Kim, B. Han, S. Kim, D. S. Kim, P. V. Pikhitsa, and M. Choi, "Parallel patterning of nanoparticles via electrodynamic focusing of charged aerosols," *Nature Nanotechnology*, vol. 1, pp. 117–121, Nov. 2006.

[42] Y. Zhu and P. R. Chiarot, "Directed assembly of nanomaterials using electrospray deposition and substrate-level patterning," *Powder Technology*, vol. 364, pp. 845–850, 2020.

[43] J. Tang and A. Gomez, "Controlled mesoporous film formation from the deposition of electrosprayed nanoparticles," *Aerosol Science and Technology*, vol. 51, no. 6, pp. 755–765, 2017.

[44] I. Bargatin, I. Kozinsky, and M. L. Roukes, "Efficient electrothermal actuation of multiple modes of high-frequency nanoelectromechanical resonators," *Applied Physics Letters*, vol. 90, 02 2007. 093116.

[45] T. Kouh, M. S. Hanay, and K. L. Ekinci, "Nanomechanical motion transducers for miniaturized mechanical systems," *Micromachines*, vol. 8, no. 4, 2017.

[46] Z. Francis, S. Incerti, S. A. Zein, N. Lampe, C. A. Guzman, and M. Durante, "Monte Carlo Simulation of SARS-CoV-2 Radiation-Induced Inactivation for Vaccine Development," *Radiation Research*, vol. 195, no. 3, pp. 221 – 229, 2021.

[47] L. A. Caldas, F. A. Carneiro, L. M. Higa, F. L. Monteiro, G. P. da Silva, L. J. da Costa, E. L. Durigon, A. Tanuri, and W. de Souza, "Ultrastructural analysis of SARS-CoV-2 interactions with the host cell via high resolution scanning electron microscopy," *Scientific Reports*, vol. 10, p. 16099, Sept. 2020.

[48] J. Zhao, H. Zhou, W. Huang, J. Zhou, M. Qiu, Z. Deng, L. Chen, Y. Weng, L. Cai, Y. Gu, Q. Zheng, Q. Chen, X. Hou, L. Wang, L. Shen, and Z. Yang,

"Cell morphological analysis of sars-cov-2 infection by transmission electron microscopy," *Journal of Thoracic Disease*, vol. 12, no. 8, 2020.

[49] N. Zhu, D. Zhang, W. Wang, X. Li, B. Yang, J. Song, X. Zhao, B. Huang, W. Shi, R. Lu, P. Niu, F. Zhan, X. Ma, D. Wang, W. Xu, G. Wu, G. F. Gao, and W. Tan, "A novel coronavirus from patients with pneumonia in china, 2019," *New England Journal of Medicine*, vol. 382, no. 8, pp. 727–733, 2020. PMID: 31978945.

[50] M. Laue, A. Kauter, T. Hoffmann, L. Möller, J. Michel, and A. Nitsche, "Morphometry of SARS-CoV and SARS-CoV-2 particles in ultrathin plastic sections of infected Vero cell cultures," *Scientific Reports*, vol. 11, p. 3515, Feb. 2021.

[51] R. Xu, M. Shi, J. Li, P. Song, and N. Li, "Construction of sars-cov-2 virus-like particles by mammalian expression system," *Frontiers in Bioengineering and Biotechnology*, vol. 8, 2020.

[52] B. Kiss, Z. Kis, B. Pályi, and M. S. Z. Kellermayer, "Topography, Spike Dynamics, and Nanomechanics of Individual Native SARS-CoV-2 Virions," *Nano Letters*, vol. 21, pp. 2675–2680, Mar. 2021. Publisher: American Chemical Society.

[53] S. Lyonnais, M. Hénaut, A. Neyret, P. Merida, C. Cazevieille, N. Gros, C. Chable-Bessia, and D. Muriaux, "Atomic force microscopy analysis of native infectious and inactivated SARS-CoV-2 virions," *Scientific Reports*, vol. 11, p. 11885, June 2021.

[54] S. Klein, M. Cortese, S. L. Winter, M. Wachsmuth-Melm, C. J. Neufeldt, B. Cerikan, M. L. Stanifer, S. Boulant, R. Bartenschlager, and P. Chlanda, "SARS-CoV-2 structure and replication characterized by in situ cryo-electron tomography," *Nature Communications*, vol. 11, p. 5885, Nov. 2020.

[55] Z. Ke, J. Oton, K. Qu, M. Cortese, V. Zila, L. McKeane, T. Nakane, J. Zivanov, C. J. Neufeldt, B. Cerikan, J. M. Lu, J. Peukes, X. Xiong, H.-G.

Kräusslich, S. H. W. Scheres, R. Bartenschlager, and J. A. G. Briggs, "Structures and distributions of SARS-CoV-2 spike proteins on intact virions," *Nature*, vol. 588, pp. 498–502, Dec. 2020.

[56] H. Yao, Y. Song, Y. Chen, N. Wu, J. Xu, C. Sun, J. Zhang, T. Weng, Z. Zhang, Z. Wu, L. Cheng, D. Shi, X. Lu, J. Lei, M. Crispin, Y. Shi, L. Li, and S. Li, "Molecular architecture of the sars-cov-2 virus," *Cell*, vol. 183, no. 3, pp. 730–738.e13, 2020.

[57] B. Turoňová, M. Sikora, C. Schürmann, W. J. H. Hagen, S. Welsch, F. E. C. Blanc, S. von Bülow, M. Gecht, K. Bagola, C. Hörner, G. van Zandbergen, J. Landry, N. T. D. de Azevedo, S. Mosalaganti, A. Schwarz, R. Covino, M. D. Mühlebach, G. Hummer, J. K. Locker, and M. Beck, "In situ structural analysis of sars-cov-2 spike reveals flexibility mediated by three hinges," *Science*, vol. 370, no. 6513, pp. 203–208, 2020.

[58] H. Ludwig, "Bovine Herpesviruses," in *The Herpesviruses: Volume 2* (B. Roizman, ed.), pp. 135–214, Boston, MA: Springer US, 1983.

[59] K. Barber, H. Daugherty, S. Ander, V. Jefferson, L. Shack, T. Pechan, B. Nanduri, and F. Meyer, "Protein Composition of the Bovine Herpesvirus 1.1 Virion," *Veterinary Sciences*, vol. 4, p. 11, Feb. 2017.

[60] J. E. Sader, "Frequency response of cantilever beams immersed in viscous fluids with applications to the atomic force microscope," *Journal of Applied Physics*, vol. 84, pp. 64–76, 07 1998.

[61] S. S. Verbridge, L. M. Bellan, J. M. Parpia, and H. G. Craighead, "Optically driven resonance of nanoscale flexural oscillators in liquid," *Nano Letters*, vol. 6, no. 9, pp. 2109–2114, 2006. PMID: 16968035.

[62] K. Yasumura, T. Stowe, E. Chow, T. Pfafman, T. Kenny, B. Stipe, and D. Rugar, "Quality factors in micron- and submicron-thick cantilevers," *Journal of Microelectromechanical Systems*, vol. 9, no. 1, pp. 117–125, 2000.

[63] R. Lifshitz and M. L. Roukes, "Thermoelastic damping in micro- and nanomechanical systems," *Phys. Rev. B*, vol. 61, pp. 5600–5609, Feb 2000.

[64] T. F. S. Inc., "Fluoro-Max Dyed Green Aqueous Fluorescent Particles (Catalog number: G200) Specifications," tech. rep.

[65] N. INC., "Accurate Spherical Gold Nanoparticles (A11-50) Certificate of Analysis," tech. rep.

[66] M. Nikolic-Jaric, S. F. Romanuik, G. A. Ferrier, G. E. Bridges, M. Butler, K. Sunley, D. J. Thomson, and M. R. Freeman, "Microwave frequency sensor for detection of biological cells in microfluidic channels," *Biomicrofluidics*, vol. 3, p. 034103, Sept. 2009.

[67] T. Chen, F. Artis, D. Dubuc, J.-J. Fournie, M. Poupot, and K. Grenier, "Microwave biosensor dedicated to the dielectric spectroscopy of a single alive biological cell in its culture medium," in *2013 IEEE MTT-S International Microwave Symposium Digest (MTT)*, (Seattle, WA, USA), pp. 1–4, IEEE, June 2013.

[68] X. Ma, X. Du, H. Li, X. Cheng, and J. C. M. Hwang, "Ultra-Wideband Impedance Spectroscopy of a Live Biological Cell," *IEEE Transactions on Microwave Theory and Techniques*, vol. 66, pp. 3690–3696, Aug. 2018.

[69] C. Watts, S. M. Hanham, J. P. K. Armstrong, M. M. Ahmad, M. M. Stevens, and N. Klein, "Microwave Dielectric Sensing of Free-Flowing, Single, Living Cells in Aqueous Suspension," *IEEE Journal of Electromagnetics, RF and Microwaves in Medicine and Biology*, vol. 4, pp. 97–108, June 2020.

[70] J.-C. Chien, A. Ameri, E.-C. Yeh, A. N. Killilea, M. Anwar, and A. M. Niknejad, "A high-throughput flow cytometry-on-a-CMOS platform for single-cell dielectric spectroscopy at microwave frequencies," *Lab on a Chip*, vol. 18, no. 14, pp. 2065–2076, 2018.

[71] C. Dalmay, M. Cheray, A. Pothier, F. Lalloué, M. Jauberteau, and P. Blondy, "Ultra sensitive biosensor based on impedance spectroscopy at microwave frequencies for cell scale analysis," *Sensors and Actuators A: Physical*, vol. 162, pp. 189–197, Aug. 2010.

[72] Y. Yang, H. Zhang, J. Zhu, G. Wang, T.-R. Tzeng, X. Xuan, K. Huang, and P. Wang, "Distinguishing the viability of a single yeast cell with an ultra-sensitive radio frequency sensor," *Lab on a Chip*, vol. 10, no. 5, p. 553, 2010.

[73] G. A. Ferrier, S. F. Romanuik, D. J. Thomson, G. E. Bridges, and M. R. Freeman, "A microwave interferometric system for simultaneous actuation and detection of single biological cells," *Lab on a Chip*, vol. 9, no. 23, p. 3406, 2009.

[74] A. Secme, U. Tefek, B. Sari, H. S. Pisheh, H. D. Uslu, A. Caliskan, B. Kucukoglu, R. T. Erdogan, H. Alhmoud, O. Sahin, and M. S. Hanay, "High-Resolution Dielectric Characterization of Single Cells and Microparticles Using Integrated Microfluidic Microwave Sensors," *IEEE Sensors Journal*, vol. 23, pp. 6517–6529, Apr. 2023.

[75] U. Tefek, B. Sari, H. Z. Alhmoud, and M. S. Hanay, "Permittivity-based microparticle classification by the integration of impedance cytometry and microwave resonators," *Advanced Materials*, vol. n/a, no. n/a, p. 2304072.

[76] B. A. Boom, A. Bertolini, E. Hennes, and J. F. J. van den Brand, "Gas damping in capacitive mems transducers in the free molecular flow regime," *Sensors*, vol. 21, no. 7, 2021.

[77] S. J. Kim, R. Dean, R. L. Jackson, and G. T. Flowers, "An investigation of the damping effects of various gas environments on a vibratory mems device," *Tribology International*, vol. 44, no. 2, pp. 125–133, 2011.

[78] B. E. Kaynak, M. Alkhaled, E. Kartal, C. Yanik, and M. S. Hanay, "Atmospheric pressure mass spectrometry by single-mode nanoelectromechanical systems," 2023.

Appendix A

Fabrication Recipes and Masks

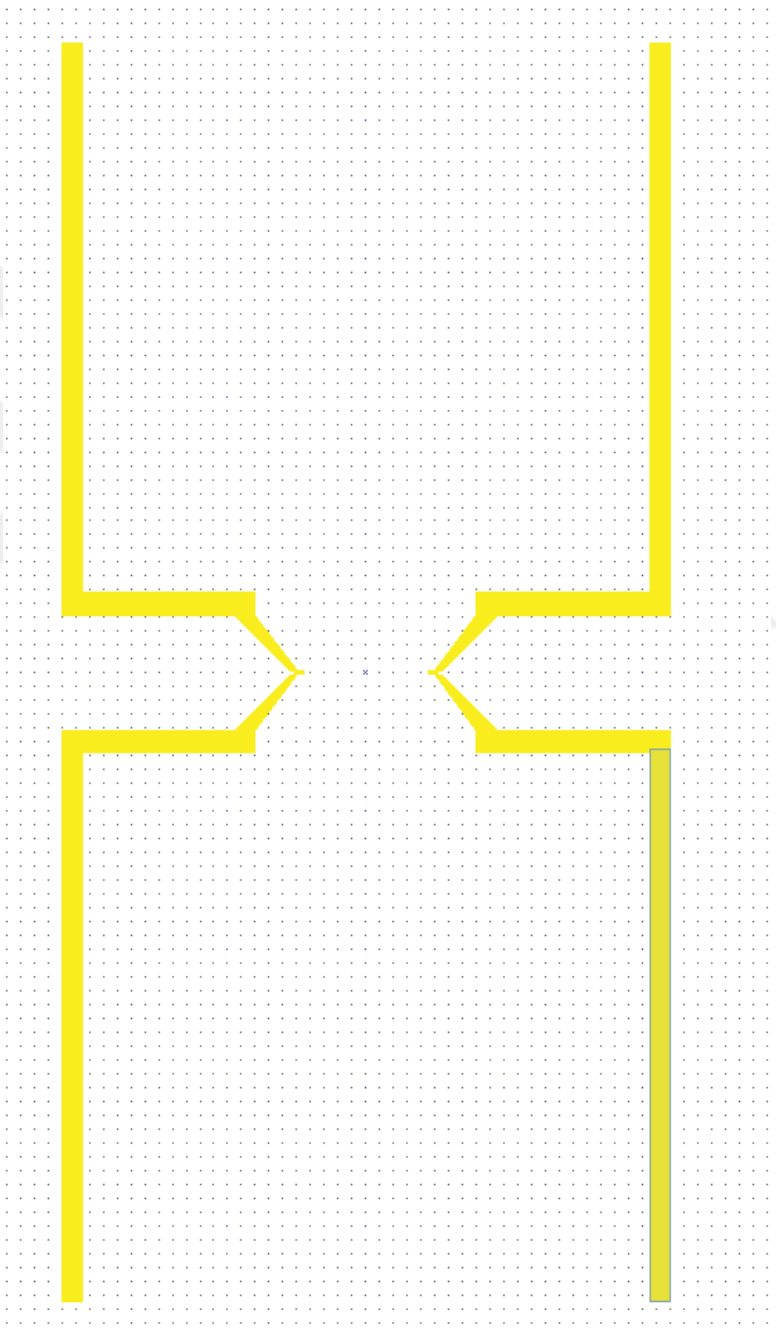

Figure A.1: 1^{st} EBL mask used for patterning the electrodes (Full size). Distance between each two subsequent dots is 1 μm

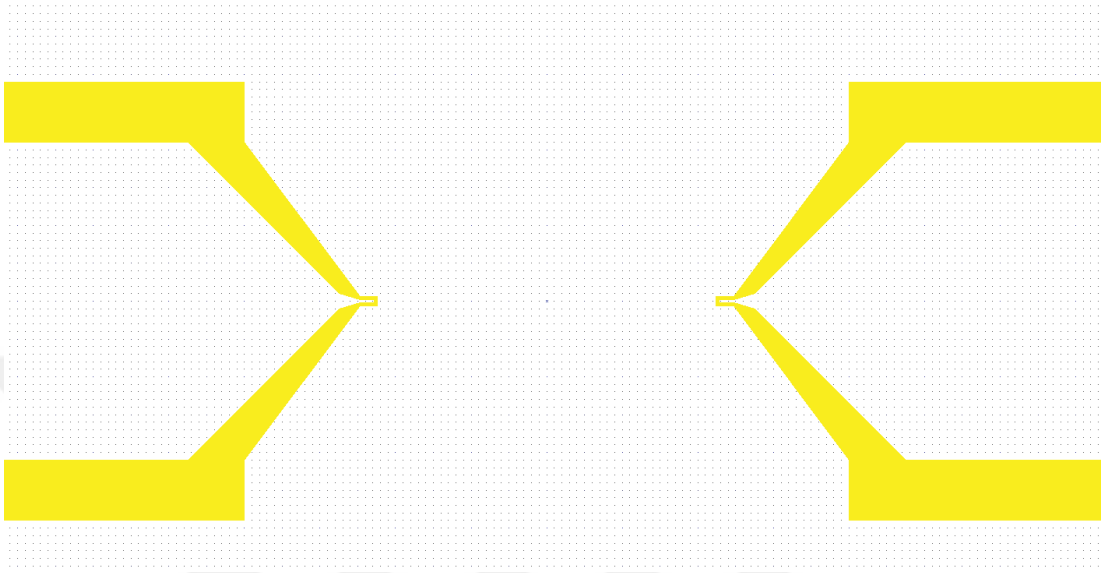

Figure A.2: Close-up view to the 1^{st} EBL mask used for patterning the electrodes. Distance between each two subsequent dots is 200 nm

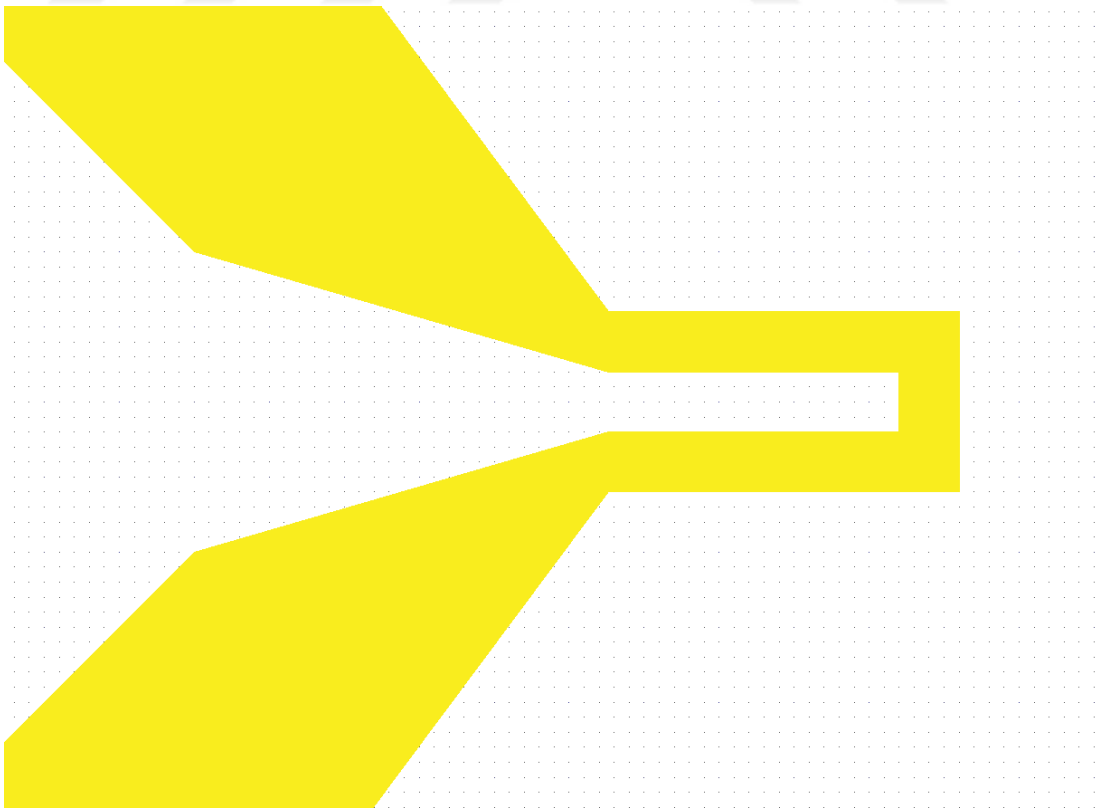

Figure A.3: Zoom-in to a single electrode in the 1^{st} EBL mask. Distance between each two subsequent dots is 20 nm

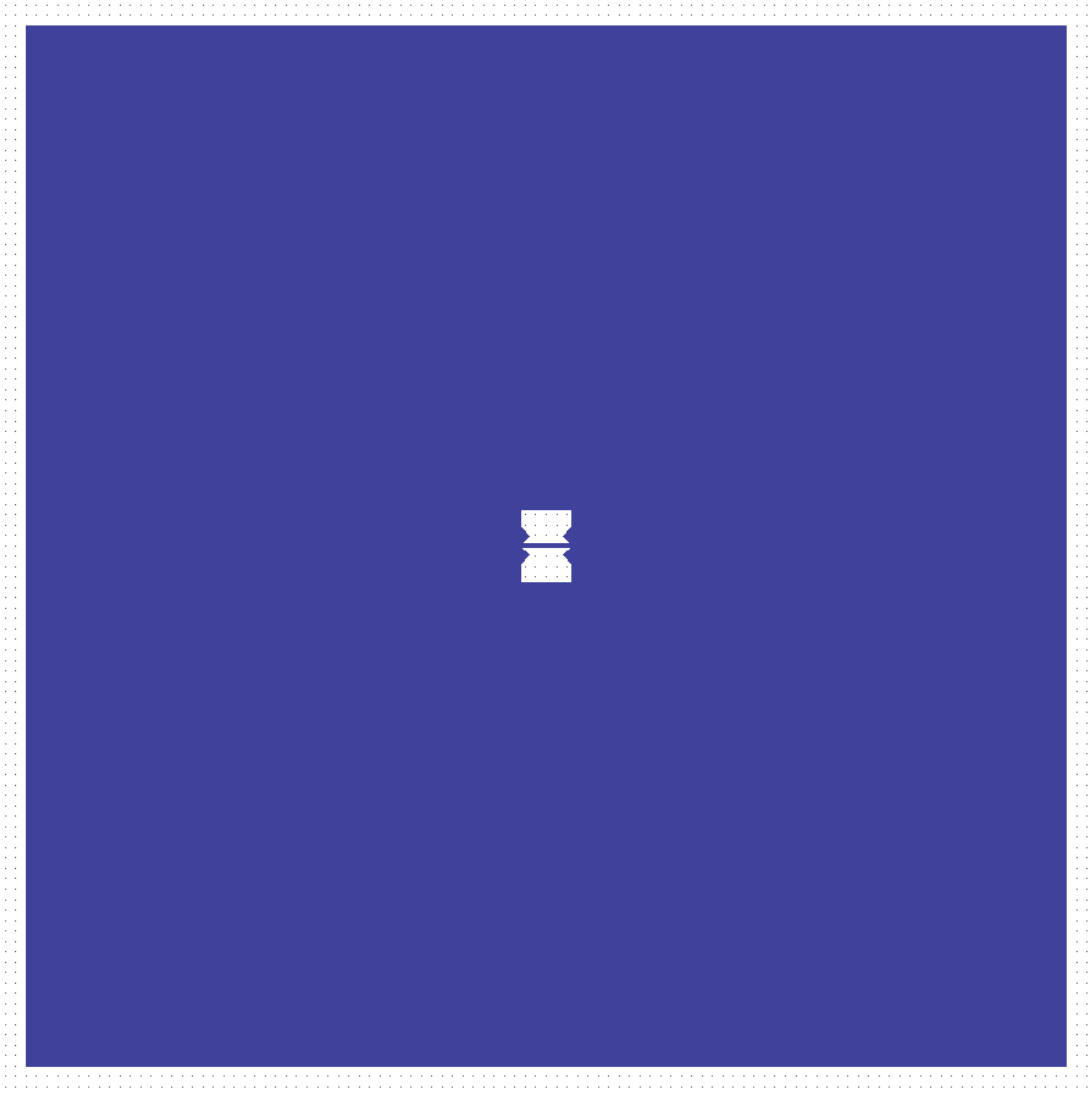

Figure A.4: 2^{nd} EBL mask used for patterning the beam and clamping region (Full size). Distance between each two subsequent dots is 2 μm

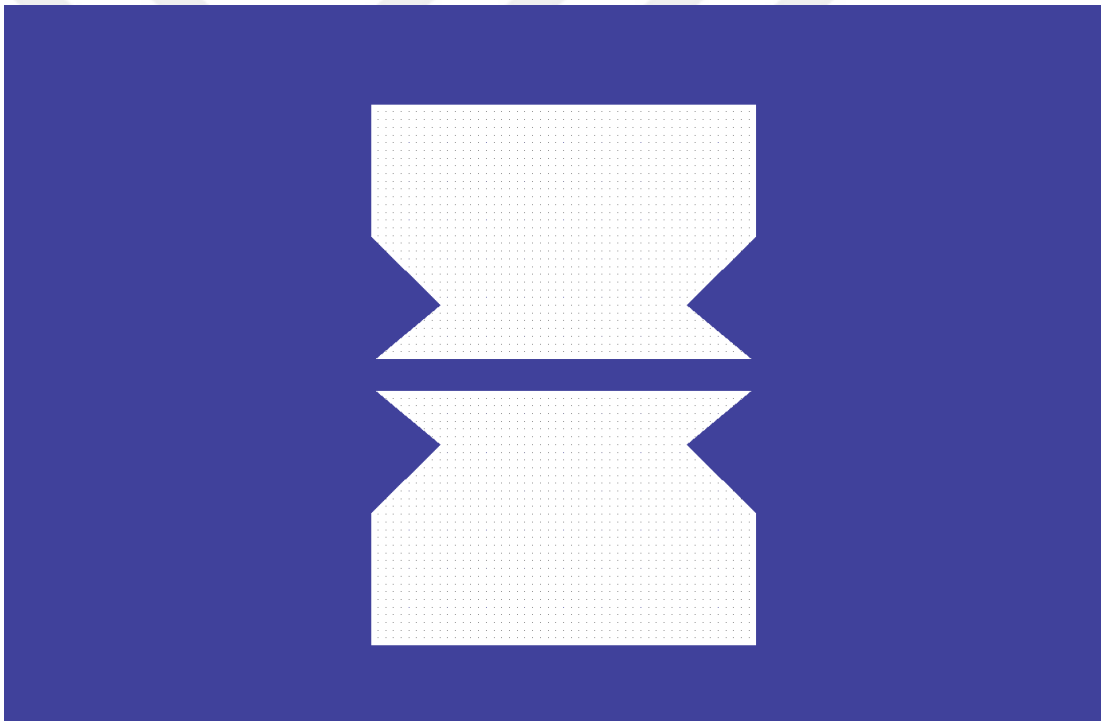

Figure A.5: Close-up view to the 2^{nd} EBL mask used for patterning the beam and clamping region. Distance between each two subsequent dots is 200 nm

Figure A.6: Layout of the 3 leg CPW resonator. Distance between each two subsequent dots is 500 nm

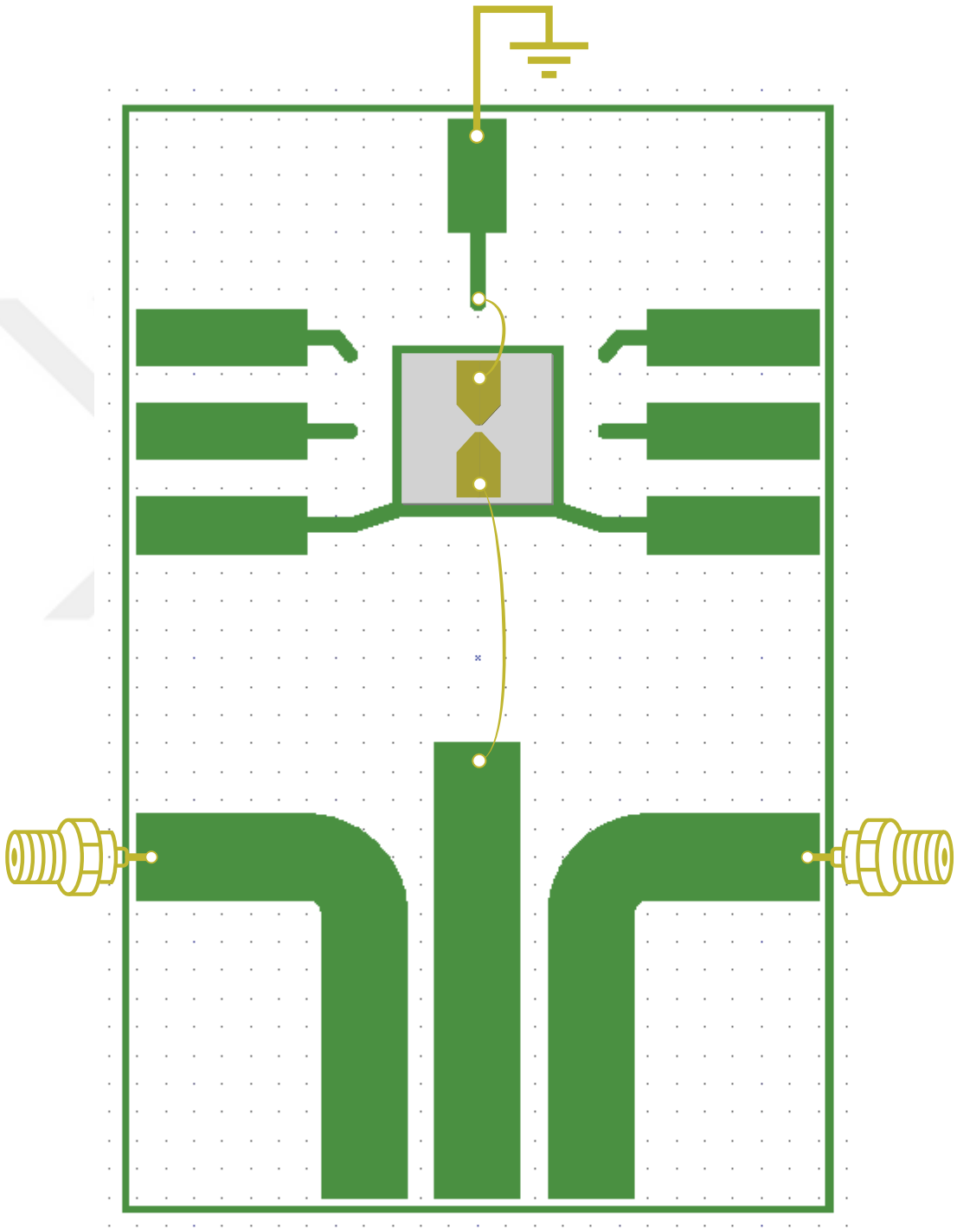

Figure A.7: Layout of the PCB utilized in the proof-of-concept microwave experiment illustrating the microwave CPW resonator, the fused silica chip with the nanoscale sensing region along with the SMA connectors and wirebonds. Distance between each two subsequent dots is 1 µm